SURFACE CHEMISTRY AT THE NANOMETER SCALE

Thesis by

Peigen Cao

In Partial Fulfillment of the Requirements

for the Degree of

Doctor of Philosophy

California Institute of Technology

Pasadena, California

2011

(Defended April 29, 2011)

Acknowledgements

There are many people to whom I would like to express my gratitude. First and foremost I would like to thank my advisor, Professor Jim Heath. I'm so grateful for his constant support and guidance during my graduate studies. His intensive enthusiasm to the pursuit of science has always been inspiring me and motivating me to think creatively about the experiments. I would also like to thank Jim for providing access to the resources that are imperative for much of my research work. I'm very grateful to have the opportunity to have worked with him.

I would also like to thank my committee members, Professor Aron Kuppermann, Professor Nate Lewis, and Professor Dan Weitekamp, who are all inspiring scientists and have guided me through my Ph.D. study.

In the Heath group, a lot of the current and past members have helped me tremendously during the past years. Dr. Hongbin Yu, a former postdoc in the group, taught me most of the basic experimental techniques when I first joined the lab, and I've learned a lot from him while working with him on the low-temperature atomic force microscopy project. Dr. Ke Xu, a former graduate student of the Heath group, has been a terrific friend and a constant source of inspiration and ideas. He collaborated with me on most of my research projects and was enormously generous with his time. I'm deeply impressed by his instincts about the experiments and have learned a lot from him. I would particularly thank Dr. Rosemary Rohde and Dr. Heather Agnew, who taught me the basic glove-box skills and infrared spectrometer techniques, and have also been always willing

to discuss the silicon functionalization project. Joey Varghese collaborated with me closely on the graphene-templated imaging project. I learnt a lot from him, and enjoyed his friendship. Thanks to Dr. Bonnie Sheriff, Dr. William Dichtel and Clara Ji-Hyun Cho on the microcontact printing project. Special thanks to Drs. Yi Luo, Guanglu Ge, Ryan Bailey, Kris Beverly, Ezekiel Johnston-Halperin, Pin Wang, Woon-Seok Yeo, Dunwei Wang, Mike McAlpine, Rong Fan, Lidong Qin, Habib Ahmad, Akram Boukai, John Nagarah, Erica Delonno, Johnny Green, Yuri Bunimovich, Jang Wook Choi, Young-Shik Shin, Gabriel Kwong, Udi Vermish, Ophir Vermesh, Slobodan Mitrovic and Steven Millward for useful discussions and assistance with experiments. I thank Dr. Qihui Shi, Dr. Ann Cheung and Dr. Jun Wang, Jen-Kan Yu, Douglas Tham, Ruo-Gu Huang, Chao Ma, Wei Wei, Kiwook Huang, Alex Sutherland, Ahrundhati Nag, Kaycie Butler, Jessica Pfeilsticker and other labmates for helpful discussions. I also thank Kevin Kan, Diane Robinson and Amy Crown for keeping the lab running at high efficiency.

Beyond the Heath group, I would also like to thank many other people who helped me and added tremendous depth to my education and experience at Caltech. I’m so grateful to Dr. Lauren Webb, a former graduate student in the Lewis group, who introduced me to the silicon functionalization project. I also learned a lot in collaboration with Dr. Santiago Solares from Goddard group on the functionalization project. Discussing with him was always a pleasure for me. I thank Professor George Rossman for helpful discussions and assistance in using the micro-Raman spectrometer. I would also like to thank Professor Franz J. Giessibl (Universitaet Augsburg) for great help in the low-temperature AFM project and generously providing their q-plus setup and valuable

suggestions. I thank Dr. Cameron Hughes and Dr. Andrew Beyer from Yeh group for helpful discussions on the AFM project.

I'd like to thank Dr. Matt Traub for help in using XPS; Dr. Chi Ma for his help with the SEM system; Dr. Guy DeRose and Bophan Chhim for training and assistance of using the facilities in the KNI; Dr. Kate Plass for making samples for STM measurements; Dr. Bruce Brunschwig and the Caltech Molecular Materials Research Center (MMRC) for assistance in using the equipment therein.

Thanks also go to Dian Buchness, Laura Howe and Agnes Tong for help with the departmental paperwork, especially during my candidacy exam and graduation. Thanks to Jim Endrizzi, Athena Trentin, Laura Kim and Daniel Yoder in ISP for their help with my visa paperwork. Thanks to Rick Gerhart and Mike Roy for their help with my glassware and machine work.

I'd also like to thank all my friends who enriched my life here at Caltech; they are Drs. Ling Shi, Changlin Pang, Chengzhong Zhang, Yong Hao, Tao Liu, Yu Liu, Fan Yang, Bolin Lin, Xin Guo, Shu Miao, Xiao Lu, Chih-Kai Ko, Xiaojie Gao, Wei Ji Ma, Siyang Zheng, I-Ren Li, Min-Shir Lin, Hsin-Ying Chiu, Valerie Norton, Hao Jiang, Jigang Wu, Zhipu Jin, John Matson, Yan Xia, Seokmin Jeon, Changshi Lao, Mo Li, Bo Li, Kechun Zhang, George Ouyang, Peera Jaru-Ampornpan, Jinyu Chen, Tingwei Mu, etc.

Finally, I'd like to express my deep gratitude to my parents and my wife for their endless love, support and encouragement. None of this would have been possible without them.

Abstract

This thesis describes research towards understanding surface chemical and physical processes, as well as their effects on the underlying substrate properties, at the nanometer and atomic scales. We demonstrate a method to tune the density of etch pits on Si(111) during the chlorination process so as to change the surface reactivity. Subsequent grafting of an azide group to replace chlorine demonstrates an example of non-oxidative passivation of silicon surfaces with new functionalities. Depending upon the solvent used in the azidation process, it is shown to yield different azidation kinetic rates, different final azide coverages, and different surface-area distributions. Scanning tunneling spectroscopy studies show that both chlorination and azidation processes significantly modify the surface electronic structures, with the former leading to a non-zero density of states at the Fermi level.

Our studies on a new class of corrugation, i.e., wrinkles, in exfoliated graphene on SiO_2 show that a “three-for-six” triangular pattern of atoms is exclusively and consistently observed on wrinkles, suggesting the local curvature of the wrinkle is a perturbation that breaks the six-fold symmetry of the graphene lattice. Lower electrical conductance is also found on the top of wrinkles compared to other regions of graphene. The wrinkles are characterized by the presence of midgap states, which is in agreement with recent theoretical predictions. A general method is also reported for reliably fabricating ultrahigh-density graphene nanoribbon (GNR) arrays. We have clearly observed how the properties of GNRs evolve as a function of number of graphene layers.

The band gap (and so the on-off ratio) decreases as the number of layers increases. These results suggest that, in addition to single layer graphene, properties of GNRs of different thicknesses can also be harnessed for engineering GNRs as different building blocks towards FET applications.

A novel imaging technique, graphene-templated scanning probe microscopy, has been developed and applied for the study on the condensation process of water and small organic molecules on mica. We found that these molecular adlayers grow epitaxially on the mica substrate in a layer-by-layer fashion. In particular, submonolayers of water form atomically flat, faceted islands of height 0.37±0.02 nm, in agreement with the height of a monolayer of ice. The second adlayers also appear ice-like, and thicker layers appear liquid-like. This general mechanism, however, is not universal. Exclusively three-dimensional droplets of water are observed on chemically modified (hydrophobic) mica surfaces, suggesting a 3D growth mechanism.

This thesis also includes my work on the design of a quartz-tuning-fork-based force sensor and related electronics for applications on low-temperature atomic force microscopy. Results show that the force-sensor-global-feedback circuit detector system induced lowest noise floor. The high detection sensitivity of this system demonstrates its ability to be used in frequency-modulated AFM at cryogenic temperatures. Surface topographic imaging of H-terminated Si(111) has been achieved at low temperatures.

Table of Contents

List of Figures

List of Tables

Chapter 1

Thesis Overview

Surface atoms/molecules of a material act as an interface to its surrounding environment; their properties are often complicated by external adsorbates/species on the surface and are often poorly understood because of a lack of accurate description of surface adsorbates/species. Surface modification often dramatically changes the surface chemical and physical properties (e.g., reactivity and surface electronic structure). As the size of objects enters into the nanometer scale, surface properties gradually dominate owing to the increasing surface-area-to-volume ratio. It is therefore important not only to thoroughly understand the surface structure but also to engineer the surface in a controllable way. In this thesis, the modifying surface chemical and physical processes will be carried out in a controllable way and characterized at the nanometer and atomic scales through both conventional and novel scanning probe microscopy methods. Other spectroscopic characterization techniques, such as infrared and X-ray photoelectron spectroscopy, are also employed in our studies. Four major research areas are discussed in this thesis and are outlined here.

Functionalization of silicon

Traditional semiconductor silicon devices are often covered by a high-quality, thick silicon dioxide layer, which acts as both a dielectric and a protection layer. This strategy prevents the devices from the external ambient environment and inhibits deleterious chemical reactions. However, surface states induced by the oxide layer increase the electron-hole recombination rate, and this problem worsens as the devices shrink in lateral size to nanometer scale. Replacement of oxides with a chemical (molecular) passivation layer has increasingly drawn a large amount of research interest. It is expected that with a well-defined chemical passivation layer, it is possible to understand and control the introduction of electronic states on Si surfaces.[1, 2]

In Chapter 2 and 3, a novel two-step chlorination/azidation functionalization protocol is developed and systematically investigated through various surface characterization techniques in order to understand the chemistry occurring on surfaces. Our scanning tunneling microscopy (STM) studies on chlorinated Si(111) surfaces show an unreconstructed 1×1 structure.[3] Tuning of surface etch pit density is demonstrated experimentally, which may enable the tailoring of the surface chemical reactivity toward subsequent alkylation and other functionalization processes. Tunneling spectroscopy reveals a non-zero density of states near zero applied bias, in contrast to analogous measurements on H/Si(111), methyl/Si(111), and ethyl/Si(111) surfaces. Subsequent grafting of azide group to replace chlorine demonstrates an example of non-oxidative passivation of silicon surfaces with new functionalities. For example, the Cu(I)-catalyzed Huisgen 1,3-dipolar cycloaddition (“click” chemistry) may be employed to introduce bio-functionalities onto the surface. By varying the solvent used in the azidation process, different azidation kinetic rates, final azide coverages, and surface-area distributions have been achieved.[4]

Graphene wrinkles and nanoribbons

Graphene refers to a monolayer of carbon atoms tightly packed into a two-dimensional (2D) honeycomb lattice. The linear dispersion spectrum of graphene causes its charge carriers to behave like massless Dirac fermions, leading to various novel electrical properties that are of fundamental interest. Small ripples (<1 nm) existing in both SiO_2-supported and free-standing graphene have been observed via transmission electron microscopy and STM. Attempts to correlate local electrical properties with these corrugations, however, have achieved only limited success.

Chapter 4 describes the STM study of a new class of corrugations in monolayer graphene sheets that have been largely neglected in previous studies, i.e., wrinkles ~10 nm in width and ~3 nm in height. We found such corrugations to be ubiquitous in graphene, and have distinctly different properties in comparison to other regions of graphene that only contain small ripples. In particular, a “three-for-six” triangular pattern of atoms is exclusively and consistently observed on wrinkles, suggesting the local curvature of the wrinkle is a perturbation that breaks the six-fold symmetry of the graphene lattice. Through scanning tunneling spectroscopy (STS), we further demonstrate that the wrinkles have lower electrical conductance when compared to other regions of graphene, and are characterized by the presence of midgap states, which is in agreement with recent theoretical predictions. Our results suggest that, in addition to the previously investigated, low-amplitude ripples, these larger wrinkles likely also play an important role in determining the electrical properties of graphene sheets.[5]

While graphene has drawn tremendous attention for studies of its fundamental structural and electronic properties in recent years, the absence of an energy gap in graphene poses a challenge for conventional semiconductor field-effect transistor (FET) device operations. Previous studies have shown that an energy gap can be opened up by patterning graphene into ribbons of nanometers in width. This is explained in terms of a quantum size effect, where the originally 2D carriers are confined into a 1D system. Most of these studies have been focused on *individual* graphene nanoribbons (GNRs). The measurement results often vary from sample to sample due to the disorders introduced along the GNR edges during the lithography process. The origin of the energy gap is therefore complicated in this situation.

Chapter 4 also describes our fabrication of ultrahigh-density parallel GNR arrays. Measurements on these GNRs show consistent results, as variations previously observed on individual GNR devices are averaged out across multiple GNRs in our studies. We found that the electron transport in all of our GNR devices exhibits thermally activated behavior (regardless of number of layers): conductance decreases with decreasing temperature. This contrasts with the behavior of “bulk” graphene films, the conductance of which generally increases as temperature decreases. More importantly, we have also for the first time clearly observed how the properties of GNRs evolve as a function of number of graphene layers. The band gap (and so the on-off ratio) diminishes as the number of layers increases. These results suggest that, in addition to single layer graphene, properties of GNRs of different thicknesses can also be harnessed for engineering the GNRs as different building blocks for FET applications.

Graphene-templated imaging

As mentioned above, surface chemical and physical properties are often closely correlated to the surface microscopic structures. Direct imaging of the microscopic structures of adsorbed water and other weakly-bound small molecules on solid surfaces at ambient conditions has been a long-time dream for surface scientists. Due to the dynamic nature of these weakly bound adsorbates, the structures of these surface species are often strongly perturbed during imaging by scanning probe microscopy because of tip-sample interactions.

Chapter 5 describes our discovery of a novel imaging technique through graphene templating. We report on the use of monolayer graphene sheets as ultrathin coatings for enabling atomic force microscopy (AFM) studies of the first water (and small organic molecules) adlayers on mica. Sputtered carbon is commonly used to coat biological systems, such as cells, for electron microscopy imaging. The carbon enables the imaging experiments by providing a protective (and conductive) coating. The graphene coating used here plays a somewhat similar role; we find graphene can tightly seal what are otherwise elusive adlayers, and stably "fix" the water adlayer structures, thus permitting the detection of the structure of the first water adlayers under ambient conditions.[6]

We found that under ambient conditions, water adlayers grow epitaxially on the mica substrate in a layer-by-layer fashion. Submonolayers form atomically flat, faceted islands of height 0.37±0.02 nm, in agreement with the height of a monolayer of ice. The second adlayers, observed at higher relative humidity, also appear ice-like, and thicker layers appear liquid-like. Our results also indicate nanometer-scale surface defects serve as nucleation centers for the formation of both the first and second adlayers.[6]

For studies of tetrahydrofuran (THF) and cyclohexane on mica, we found that the first two adlayers of both molecules adsorb in a layer-by-layer fashion, and atomically flat two-dimensional islands are observed for both the first and the second adlayers. THF adlayers form initially as rounded islands, but over a time period of weeks evolve into faceted islands, suggesting that the adlayers possess both liquid and solid properties at room temperature. Cyclohexane adlayers form crystal-like faceted islands, and are immobile under the graphene template. Precise adlayer height measurements further permitted the identification of the crystal structures of the adlayers. The heights of the second adlayers of THF and cyclohexane are measured to be 0.44±0.02 and 0.50±0.02 nm, respectively, in good agreement with the layer thicknesses in the monoclinic crystal structure of THF and the Phase I "plastic crystal" structure of cyclohexane. The first adlayers appear slightly thinner for both molecules, indicative of interactions of the molecules with the mica substrate.[7]

Quartz-tuning-fork-based low temperature atomic force microscopy

In Chapter 6, we describe the design of a quartz-tuning-fork-based force sensor and related electronics for applications in low-temperature atomic force microscopy. Noise performance of three types of pre-amplifier electronics has been compared. Results show that the force-sensor-global-feedback circuit detector system induces the lowest noise floor. The high detection sensitivity of this system demonstrates its ability to be used in frequency-modulated AFM at cryogenic temperatures. The quality factor of the tuning-fork-tip ensemble has also been examined. We found that a high Q of ~9000 in vacuum at ~77K is obtained for a q-Plus type of tuning-fork-tip system. This facilitates accurate detection of frequency in AFM. Surface topographic imaging from H-terminated Si(111) has been achieved, which verifies our design of quartz tuning fork-based force sensor and pre-amplifier.

References

1. Yu, H.B. et al. Scanning tunneling microscopy of ethylated Si(111) surfaces prepared by a chlorination/alkylation process. *J Phys Chem B* **110**, 23898-23903 (2006).
2. Dichtel, W. et al. Surface chemistries for molecular electronics. *Abstr Pap Am Chem S* **236**, 48-ORGN (2008).
3. Cao, P.G., Yu, H.B. & Heath, J.R. Scanning tunneling microscopy and spectroscopy of wet-chemically prepared chlorinated Si(111) surfaces. *J Phys Chem B* **110**, 23615-23618 (2006).
4. Cao, P.G., Xu, K. & Heath, J.R. Azidation of silicon(111) surfaces. *J Am Chem Soc* **130**, 14910-14911 (2008).
5. Xu, K., Cao, P.G. & Heath, J.R. Scanning tunneling microscopy characterization of the electrical properties of wrinkles in exfoliated graphene monolayers. *Nano Lett.* **9**, 4446-4451 (2009).
6. Xu, K., Cao, P.G. & Heath, J.R. Graphene visualizes the first water adlayers on mica at ambient conditions. *Science* **329**, 1188-1191 (2010).
7. Cao, P.G., Xu, K., Varghese, J.O. & Heath, J.R. Atomic force microscopy characterization of room-temperature adlayers of small organic molecules through graphene templating. *J Am Chem Soc* **133**, 2334-2337 (2011).

Chapter 2

Chlorine-Terminated Silicon(111) Surfaces

The contents presented in this chapter are based on Cao, P.G., Yu, H.B. and Heath, J.R. "Scanning tunneling microscopy and spectroscopy of wet-chemically prepared chlorinated Si(111) surfaces," *J Phys Chem B*, 110, 23615-23618 (2006). (Ref.[1])

2.1 Introduction

Functionalization of Silicon(111) surfaces with covalently bonded organic reagents has received an increasing interest as a method for tailoring the chemical and electrical properties of Si surfaces.[2-6] In particular, alkyl passivated Si(111) surfaces prepared through a two-step chlorination/alkylation route[4-6] have shown low charge-carrier surface recombination velocities, oxidation resistance in air and during anodic current flow in electrochemical cells, and a number of other interesting chemical and electronic properties. The chlorinated Si(111) surface (Cl/Si(111)) is a key intermediate in this chemistry. Chemical component analysis of Cl/Si(111) surfaces has been performed using X-ray photoelectron spectroscopy,[6, 7] infrared,[8] and high-resolution electron energy loss spectroscopy,[9] indicating formation of the Cl-Si bond. The expected 1×1 structure of the chlorination layer was confirmed in a recent scanning tunneling microscopy study of Cl/Si(111) surface prepared by the gas phase reaction of H/Si(111) with molecular chlorine.[9] Cl-Si bond-induced stacking faults were previously observed by Itchkawitz et al.[10] That report was based upon the observation that inequivalent crystallographic directions (<$\bar{1}\bar{1}2$> and <$11\bar{2}$>) were found to exhibit the same bilayer step edge structure. In addition, significant enhancement of surface conductance for Cl/Si(111) was reported by Lopinski et al.[11] A p-type inversion layer was used to interpret this effect in terms of the formation of a 2D hole gas.

The morphology of a chlorinated Si(111) surface is apparently dependent upon the nature of the chemistry utilized for that chlorination, and that is the hypothesis that we test in this chapter. For example, when a H/Si(111) surface that is characterized by a low density of step edges is halogenated via the reaction with gas phase molecular chlorine, the resultant Cl/Si(111) surface remains extremely flat.[9] However, when a similarly flat H/Si(111) is chlorinated via the reaction with PCl_5 in chlorobenzene solution and subsequently alkylated, the resultant alkyl/Si(111) is characterized by a high density of etch pits, with a corresponding large fraction of alkylated Si atoms residing at the edge of those pits.[12, 13] Those atoms are more chemically accessible than the alkylated Si atoms that reside on terraces, and so can play a role in subsequent chemical processes on the surface.[14] They can also play important roles in driving the formation of a stacking fault.[12]

The etch pits presumably originate during the chlorination procedure. In this chapter, we present detailed results on the scanning tunneling microscopy (STM) and tunneling spectroscopy (STS) investigations of wet-chemically prepared Cl/Si(111) surfaces. We show that this wet-chemical chlorination of H/Si(111) does, in fact, introduce a large density of etch pits of one or more atomic steps in depth. Nevertheless, Cl atoms still passivate 100% of the atop Si atom sites on the unreconstructed Si(111) surface. The etch pits result in fragmented <$11\bar{2}$> steps and do not lead to stacking faults on the chlorinated surface. Unlike the case for H/Si(111), methyl/Si(111) or ethyl/Si(111),[15] tunneling spectroscopy revealed the absence of a band gap: current-voltage traces exhibited a non-zero slope at zero applied bias, implying a non-zero density-of-states (DOS) at the Fermi level.

2.2 Wet-chemical preparation of Cl-terminated Si(111) surfaces

The substrates utilized were (111)-oriented, Sb-doped, n-type Si wafers with a low miscut angle of ±0.5° and a resistivity of 0.005-0.02 ohm·cm. Anhydrous inhibitor-free tetrahydrofuran (THF, ≥99.9%, water content <0.002%) was purchased from Sigma-Aldrich. Phosphorus pentachloride (PCl5, 99.998%) was purchased from Alfa Aesar. These reagents were used as supplied and stored in a glovebox purged with nitrogen.

Silicon wafers were cut into samples of 0.5×1cm pieces. A standard RCA cleaning process was then carried out. Briefly, the substrate was immersed in a basic peroxide solution which is composed of 1:1:4 by volume of 28% $NH_3{\bullet}H_2O(aq)$/30% H_2O_2/H_2O at 80°C for at least 10 min and then rinsed thoroughly in running Milli-Q water. H-terminated Si(111) surface was then formed after immersing the cleaned sample in 40% NH_4F for about 15 min. This step produces large, atomically flat terraces.[16] Chlorination was performed in a nitrogen-purged glovebox. A few grains of benzoyl peroxide were added to a saturated solution of PCl_5 in chlorobenzene and the solution was then heated to 90-100°C for 50 min. For lower temperature experiments, reaction time was adjusted so that a complete chlorination of the Si surface was reached. This was monitored by the surface conductivity test, since the conductivity was observed to increase significantly in comparison with H/Si. After the reaction, the sample was removed from the solution and rinsed thoroughly with tetrahydrofuran. The samples were then dried under streaming N_2(g), mounted onto a sample stage, and quickly introduced into an Omicron low-temperature STM system.

The STM microscope is contained in an ultrahigh vacuum chamber with an operating pressure of $<6\times10^{-11}$ Torr. Both topographic and spectroscopic data were acquired at 77 K by use of a mechanically cut or etched Pt-Ir tip. In a typical topographic imaging measurement, the tip is brought 5-15 Å away from the sample surface. In our measurements, a tip/vacuum/sample junction resistance of 5-20 GΩ was maintained by setting up the sample voltage and tunneling current. Surface electronic properties are examined by measuring the tunneling spectroscopy simultaneously with topographic image acquisition. Briefly, at each topographic raster scanning point the feedback was temporarily switched off, and the tip-sample distance was then fixed. The tip-sample tunneling current I_t was then recorded while scanning the tip-sample voltages, which results in a total number of ~2500 current-voltage $I_t(V)$ traces in an STM image. The derivative dI_t/dV is then numerically calculated from the averaged $I_t(V)$ spectroscopic data.

2.3 STM results

Figure 2.1(a)-(c) shows constant-current STM images of the Cl/Si(111) surfaces prepared at three temperatures. The etch hillocks of a single bilayer step are clearly seen, and are pointing to the $<\bar{1}\bar{1}2>$ orientation. In comparison with the H/Si(111),[16] an obvious increase in etch pit density was observed for Cl/Si(111) prepared at all three temperatures. These etch pits are of one or more bilayer steps in depth. Previous results from methylated and ethylated Si(111) surfaces displayed a similar etch pit morphology,[6] although again with atomically flat terraces. The conclusion is that the increased etch pit density is most certainly caused by the wet-chemical chlorination procedure. Since the step sites are expected to be more chemically accessible than the terrace sites, the chlorination chemistry essentially transforms these relatively inert terrace sites to more reactive step sites that can be exploited in subsequent chemical reactions. It may thus be possible to tailor the surface chemical activity by changing the terrace-to-step site ratio via control over the chlorination chemistry. The etching chemistry could, in fact, be modified by changing the reaction temperature (Figure 2.1). The coverage of etch pit and edge atom were quantified and plotted versus temperature in Figure 2.1(d). An increase in reaction temperature led to an increase in both etch pit coverage and terrace-to-step ratio. A dependence of etch pit density upon the reaction conditions was also observed for Cl/Si(111) prepared via reactions of H/Si(111) with Cl_2(g). Under UV irradiation and at room temperature, Lopinski and coworkers[11] prepared Cl/Si(111) surfaces with a considerable number of etch pits by reaction with molecular chlorine, whereas the reaction without UV irradiation resulted in a completely flat surface with few etch pits.[9] The surface morphology is apparently dependent upon the relative etch rates of the terraces, step edges, kinks and other surface structures. The large number of etch pits in the Cl/Si(111) surface observed on surfaces prepared at higher temperatures is likely ascribable to the increased ratio of the terrace etch rate to the kink etch rate.

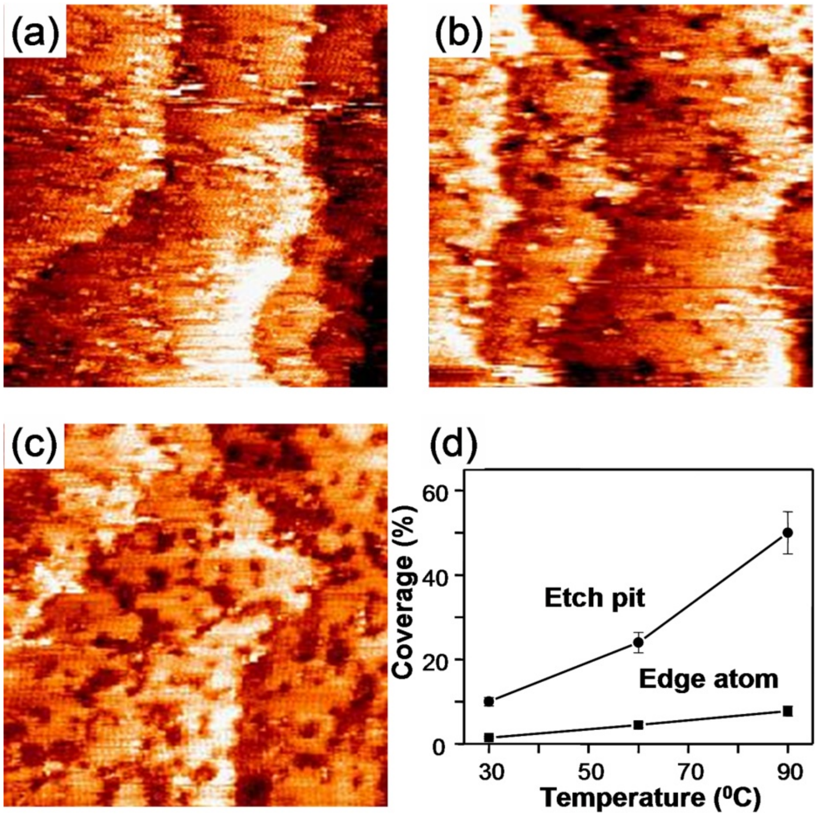

Figure 2.1. Large-field view of STM topographic images. (a)-(c) Constant-current STM images of the Cl/Si(111) surfaces prepared at different temperatures - (a) 30°C, 5 hr, (b) 60°C, 3hr, (c) 90°C, 50 min - acquired at a sample voltage of -1.0 V. Scan area is 100 nm × 100 nm for all three images. (d) Plot of etch pit and edge atom coverage against reaction temperature.

In spite of the increased number of etch pits in the chlorinated surface, a full coverage of Cl-Si on the Si(111) atop sites could be achieved through the solution phase chemical approach. This nearly 100% coverage is suggested by the constant-height atomic-resolution image as shown in Figure 2.2, and by experiments in which methyl and acetyl Grignard reagents have been shown to fully alkylate such a chlorinated surface.[6, 14] Constant-current mode images, at this resolution, were of slightly poorer quality but still revealed the full coverage and hexagonal structure of the Cl-Si on the surface. While it would have been interesting to obtain an image of a step edge at a similarly high resolution to that presented in Figure 2.2, such an image would require constant-current-mode imaging. Statistical analysis of the nearest-neighbor-atom distances revealed a peak value of 3.90±0.12 Å, which is in agreement with the distance between silicon atop sites on the unreconstructed Si(111) surface.[17] This suggests an unreconstructed 1×1 structure and hence a full passivation of the Si atop sites by Cl, consistent with reported results from the gas phase chlorination of H-terminated Si(111).[9] Similar images were obtained from other terrace sites. Atomically flat surfaces with a minimal amount of contamination can be identified from the image, indicating that the wet-chemically prepared Cl/Si(111) can survive at least moderate post-processing conditions that include a several minute air exposure prior to introduction into the UHV STM chamber.

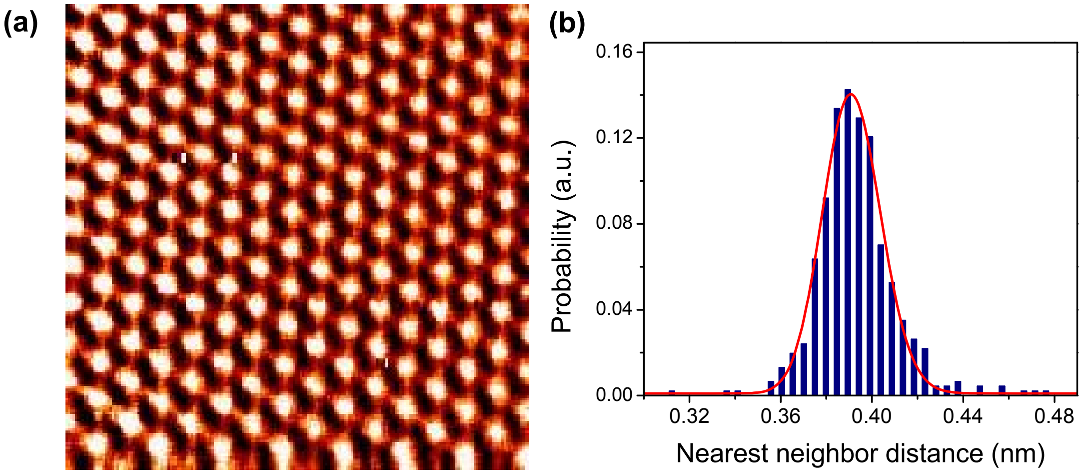

Figure 2.2. Close-up STM images with atomic resolution. (a) Constant height STM image of surface prepared at 90°C showing uniform Cl atom coverage of the atop sites of the unreconstructed surface. Scan area = 5×5 nm, V_b = -0.8 V, I_t = 0.27 nA. (b) Histogram of the distribution of distance between nearest neighbor atoms. A lognormal fit is indicated by a red line, which peaks at 0.39 nm. The full-width at half maximum gives an error of about ±0.012 nm.

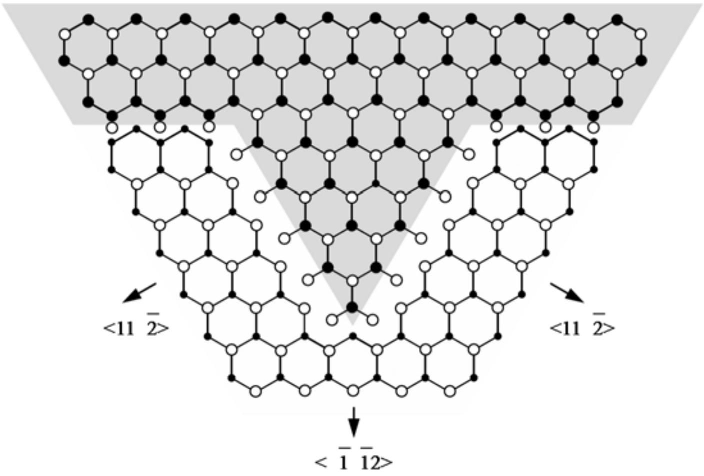

(a) Top view

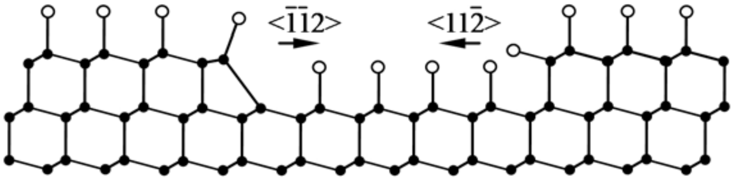

(b) Side view

Figure 2.3. Schematics of the structure of steps on Cl-terminated Si(111) surfaces. The <11$\bar{2}$> and <$\bar{1}\bar{1}$2> steps are indicated by arrows.

Another interesting set of observations are the fragmented <11$\bar{2}$> steps with the outward normal along the <11$\bar{2}$> orientation. Figure 2.3a is an illustration of the etch hillock observed in STM images. For H/Si(111) surfaces, it has been shown that a <11$\bar{2}$> step is terminated by the lower Si atoms of the bilayer, forming a horizontal monohydride termination structure.[16] By contrast, <$\bar{1}\bar{1}$2> steps are terminated by the upper Si atoms, resulting in a vertical dihydride structure.[16] Upon chlorination, a rebonded step geometry was formed at the <$\bar{1}\bar{1}$2> steps, where the step terminating Si atoms are bonded to the bottom terrace silicon atoms (see Figure 2.3b).[10] The full chlorination of the <11$\bar{2}$> step terminating Si atoms has been shown to be energetically unfavorable. This might be attributed to the significant electrostatic repulsion between the negatively charged chlorine atoms along the upper and lower terraces of the <11$\bar{2}$> steps.[10] Periodic DFT calculations indicated that the Si-Cl bond on <$\bar{1}\bar{1}$2> is 0.58 eV stronger than on <11$\bar{2}$>. For CH_3/Si(111) the difference is even greater (0.67 eV).[12]

A stacking fault basically switches a <11$\bar{2}$> step to a <$\bar{1}\bar{1}$2> step. Calculations indicated that a full stacking fault on the terraces is energetically possible for etched CH_3/Si(111) and Cl/Si(111) surfaces. Partly faulted regions were observed by Itchckawitz et al.[10] on the Cl/Si(111), and were inferred for CH_3/Si(111) by us through a combination of experiment[6] and theory.[12] For our Cl/Si(111) surfaces prepared at 90°C, the terrace-to-step site ratio (estimated to be ~13 from the STM images) indicates that stacking faults would be energetically possible.[12] However, no stacking faults were observed for any of our preparations. Careful inspection of the etch hillock edges (Figure 2.1c) revealed that the <11$\bar{2}$> step edges were actually segmented, or further etched. An etched <11$\bar{2}$> step edge site creates two kink sites, each of which possesses the <$\bar{1}\bar{1}$2> step edge structure. This further etching therefore partially removes the <11$\bar{2}$> step edge atoms and essentially changes the <11$\bar{2}$> step structure to the <$\bar{1}\bar{1}$2> step structure, thus stabilizing the surface.

2.4 STS results

We also investigated the tunneling spectroscopy of wet-chemically prepared Cl/Si(111). Current-voltage $I_t(V)$ traces, averaged over the area shown in Figure 2.2a are represented in Figure 2.4a, together with a similarly averaged trace collected from H/Si(111). The derivative dI_t/dV, which is roughly proportional to the local density of states, is shown in Figure 2.4b. The set points for bias voltage and current were experimentally varied to optimize image quality. For the data shown in Figure 2.4a, the parameters were -0.8 V and 0.27 nA for Cl/Si(111) and -1.7 V and 0.12 nA for H/Si(111).

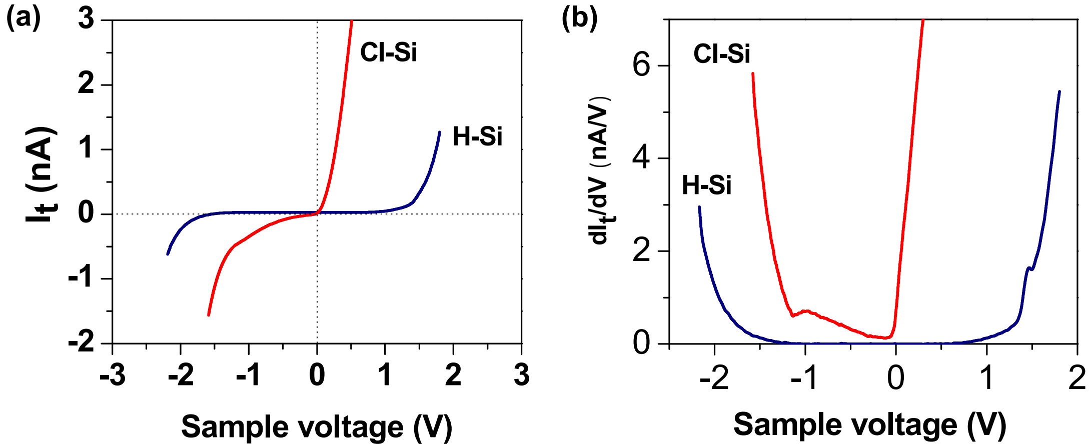

Figure 2.4. Scanning tunneling spectroscopy of Cl/Si(111). (a) Representative low temperature (77K) I-V spectra for H- and Cl-terminated Si(111) surfaces. (b) Corresponding dI_t/dV tunneling spectrum for the above two surfaces.

Fully passivated H/Si(111) exhibits a large conductance gap, and this was observed in a bias voltage range down to -1.7 V, where a limiting value of 1.6 V was obtained. Similarly large conductance gaps have been recently reported for methyl/Si(111) (100% passivation) and ethyl/Si(111) (80% ethyl-; 20% H-passivation).[15] This has been attributed to the absence of surface states for these chemically functionalized surfaces. The apparent larger value of the measured band gap compared to the standard bulk silicon gap (1.12 eV at 300 K) can be attributed to the tip-induced band bending (TIBB, see Figure 2.5a).[18] Since only part of the sample-tip voltage is applied across the vacuum gap, the onset of current is postponed till larger voltage values are reached. Interestingly, at small negative sample voltages just below the sample Fermi level, the expected tunneling current component (I_D) from the conduction-band electrons was not observed, while this is commonly observed at cleaved n-type GaAs surfaces.[19] The absence of this current component suggests a rather small tunneling transmission coefficient of conduction-band electrons from the sample to the tip. A possibility may be that the very sharp tip may not accommodate those states with non-zero momentum parallel to the semiconductor sample surface.[20]

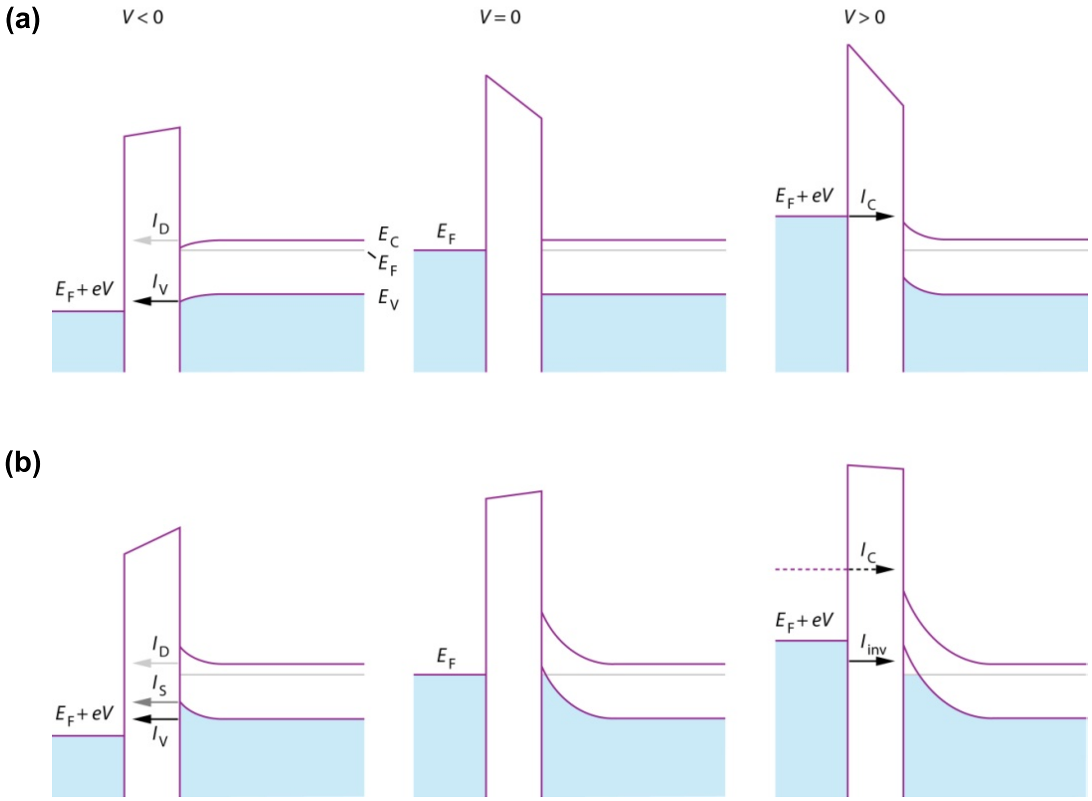

Figure 2.5. Schematic illustration of energy bands, showing the conduction-band minimum E_C and valence-band maximum E_V. The Fermi level of the sample is denoted by E_F and that of the tip E_F+eV, where V is the sample voltage. (a) Tip-induced band bending (TIBB). The arrows indicate the tunneling direction of electrons. (b) Adatom-induced band bending. The residue TIBB is also indicated at non-zero sample-tip voltages.

The current-voltage characteristics of Cl/Si(111) exhibited no evidence of a band gap (see Figure 2.4a), with the I-V curve possessing a finite slope at zero bias voltage. Varying the bias voltage in a range of -1.5 ~ -0.3 V showed consistent results. This indicates a non-zero DOS at the Fermi level. From the dI_t/dV versus voltage plot (Figure 2.4b), three different conductance regions are noticed. At positive values of sample voltage, a conductance response attributable to tunneling out of filled levels of the tip and into the empty levels of Si is observed. At negative-valued sample voltages below about -1.1 V the current is dominated by the tunneling of the valence band electrons from the silicon into the tip. The third region is that which is bracketed by negative-valued sample biases between 0 and -1.1 V.

Since the UHV STM images show atomically flat surfaces with minimal surface contamination, the finite conductance observed at zero bias could then be explained in terms of the intrinsic Cl/Si(111) surface properties. Unlike the H/Si(111) where the Fermi level is unpinned, the strong electronegativity of chlorine is expected to induce a large upward band bending (Figure 2.5b), where the Fermi level approaches the top of the valence band edge.[21] Strong surface band bending induced by adsorbates such as metal and semiconductor atoms, oxygen and halogens have been observed at even sub-monolayer coverages.[22] These adsorbates have also been shown to induce intrinsic surface states, pinning the Fermi level (E_F) at a position dependent upon the difference between the electronegativity of the adsorbate and the substrate atoms.[22] E_F pinning close to the edge of the valence band has been previously observed on Cl/GaAs(110) surfaces.[21] Recently, four-point measurements on Cl/Si(111) by Lopinski et al.[11] showed a high surface conductance, which is about 3 times of the bulk value. A p-type inversion layer was invoked to explain this effect. According to this model, at small positive voltages above the Fermi level, tunneling of electrons into the inversion layer may dominate the current till the onset of the conduction-band current (Figure 2.5b). At small negative sample bias, tunneling of both conduction-band electrons and surface valence-band edge electrons may both contribute to the current. The probability of thermionic emission of silicon conduction-band electrons followed by tunneling through the vacuum barrier is expected to be rather low.[23] At increasing values of negative sample bias, the surface barrier decreases and hence the tunneling current increased. A theoretical model of this surface would likely provide clarification of this picture. Surface recombination velocity measurements[24] have revealed a low velocity for a freshly prepared Cl/Si sample, followed by a sharp increase in recombination rate upon oxidation. Interestingly, although the observation of finite conductance between 0 and -1.1 V may obscure the observation of the valence band edge, the present data do exhibit a gap voltage difference that is very close to the bulk band gap value.

2.5 Conclusion

In this chapter, we have reported on the scanning tunneling microscopy and spectroscopic studies of Cl-terminated Si(111) surfaces. Cryo-STM images of wet-chemically prepared Cl/Si(111) surfaces showed an unreconstructed 1×1 structure and hence full replacement of hydrogen by chlorine atoms. An increased etch pit density relative to gas phase prepared Cl/Si(111) was observed, and could be controlled experimentally. Such control may enable the tailoring of the surface chemical reactivity toward subsequent alkylation and other functionalization processes. Tunneling spectroscopy revealed a non-zero DOS near zero applied bias, in contrast to analogous measurements on H/Si(111), methyl/Si(111), and ethyl/Si(111) surfaces. This may indicate that the electronegative Cl atoms are inducing surface states which are contributing to current observed within the usual forbidden region.

2.6 References

1. Cao, P.G., Yu, H.B. & Heath, J.R. Scanning tunneling microscopy and spectroscopy of wet-chemically prepared chlorinated Si(111) surfaces. *J Phys Chem B* **110**, 23615-23618 (2006).
2. Buriak, J.M. Organometallic chemistry on silicon and germanium surfaces. *Chem Rev* **102**, 1271-1308 (2002).
3. Weldon, M.K., Queeney, K.T., Eng, J., Raghavachari, K. & Chabal, Y.J. The surface science of semiconductor processing: gate oxides in the ever-shrinking transistor. *Surf Sci* **500**, 859-878 (2002).
4. Bansal, A. et al. Alkylation of Si surfaces using a two-step halogenation Grignard route. *J Am Chem Soc* **118**, 7225-7226 (1996).
5. Royea, W.J., Juang, A. & Lewis, N.S. Preparation of air-stable, low recombination velocity Si(111) surfaces through alkyl termination. *Appl Phys Lett* **77**, 1988-1990 (2000).
6. Yu, H.B. et al. Low-temperature STM images of methyl-terminated Si(111) surfaces. *J Phys Chem B* **109**, 671-674 (2005).
7. Rivillon, S. et al. Chlorination of hydrogen-terminated silicon(111) surfaces. *J Vac Sci Technol A* **23**, 1100-1106 (2005).
8. Rivillon, S., Amy, F., Chabal, Y.J. & Frank, M.M. Gas phase chlorination of hydrogen-passivated silicon surfaces. *Appl Phys Lett* **85**, 2583-2585 (2004).
9. Eves, B.J. & Lopinski, G.P. Formation and reactivity of high quality halogen terminated Si(111) surfaces. *Surf Sci* **579**, L89-L96 (2005).
10. Itchkawitz, B.S., McEllistrem, M.T. & Boland, J.J. Equivalent step structures along inequivalent crystallographic directions on halogen-terminated Si(111)-(1x1) surfaces. *Phys Rev Lett* **78**, 98-101 (1997).
11. Lopinski, G.P. et al. Enhanced conductance of chlorine-terminated Si(111) surfaces: Formation of a two-dimensional hold gas via chemical modification. *Phys Rev B* **71**, 125308 (2005).

12. Solares, S.D. et al. Chlorination-methylation of the hydrogen-terminated silicon(111) surface can induce a stacking fault in the presence of etch pits. *J Am Chem Soc* **128**, 3850-3851 (2006).
13. Yu, H.B. et al. Scanning tunneling microscopy of ethylated Si(111) surfaces prepared by a chlorination/alkylation process. *J Phys Chem B* **110**, 23898-23903 (2006).
14. Rohde, R.D., Agnew, H.D., Yeo, W.S., Bailey, R.C. & Heath, J.R. A non-oxidative approach toward chemically and electrochemically functionalizing Si(111). *J Am Chem Soc* **128**, 9518-9525 (2006).
15. Yu, H.B., Webb, L.J., Heath, J.R. & Lewis, N.S. Scanning tunneling spectroscopy of methyl- and ethyl-terminated Si(111) surfaces. *Appl Phys Lett* **88**, 252111 (2006).
16. Hines, M.A. In search of perfection: Understanding the highly defect-selective chemistry of anisotropic etching. *Annu Rev Phys Chem* **54**, 29-56 (2003).
17. Waltenburg, H.N. & Yates, J.T. Surface-chemistry of silicon. *Chem Rev* **95**, 1589-1673 (1995).
18. Mcellistrem, M., Haase, G., Chen, D. & Hamers, R.J. Electrostatic sample-tip interactions in the scanning tunneling microscope. *Phys Rev Lett* **70**, 2471-2474 (1993).
19. Stroscio, J.A., Feenstra, R.M. & Fein, A.P. Local state density and long-range screening of adsorbed oxygen-atoms on the GaAs(110) surface. *Phys Rev Lett* **58**, 1668-1671 (1987).
20. Jager, N.D., Weber, E.R., Urban, K. & Ebert, P. Importance of carrier dynamics and conservation of momentum in atom-selective STM imaging and band gap determination of GaAs(110). *Phys Rev B* **67**, 165327 (2003).
21. Troost, D., Koenders, L., Fan, L.Y. & Monch, W. Pinning of the Fermi level close to the valence-band top by chlorine adsorbed on cleaved GaAs(110) surfaces. *J Vac Sci Technol B* **5**, 1119-1124 (1987).
22. Monch, W. Virtual gap states and Fermi level pinning by adsorbates at semiconductor surfaces. *J Vac Sci Technol B* **4**, 1085-1090 (1986).
23. Stroscio, J.A. & Feenstra, R.M. Scanning tunneling spectroscopy of oxygen adsorbates on the GaAs(110) surface. *J Vac Sci Technol B* **6**, 1472-1478 (1988).
24. Lewis, N.S. Private communication.

Chapter 3

Azidation of Silicon(111) Surfaces

The contents presented in this chapter are based on Cao, P.G., Xu, K. and Heath, J.R. "Azidation of silicon(111) surfaces," *J Am Chem Soc*, 130, 14910-14911 (2008). (Ref.[1])

3.1 Introduction

The passivation of nonoxidized silicon surfaces has emerged as a potential method for protecting the silicon surface from oxidation,[2-8] for improving the electronic properties of ultrathin silicon films,[9, 10] and for adding new chemical function to those surfaces.[11-19] The Si(111) surface has provided the template for much of this chemistry. In Chapter 1, we have systematically studied the morphology and surface electronic structures modified through capping silicon atop sites with chlorine atoms. While the atop sites on the unreconstructed Si(111) surface may be fully passivated with H, Cl or Br atoms, those surfaces are unstable to oxidation.[20, 21]

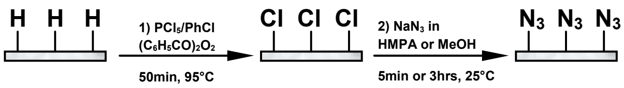

Figure 3.1. A schematic showing the two-step chlorination/azidation surface synthetic process.

Full passivation (close to100%) of the silicon atop sites with methyl[22] or acetyl[23] groups has also been achieved. Those surfaces (H_3C-/Si(111) and HC≡C-/Si(111)) are stable against oxidation, which is reflective of both the high coverage and the stability of the Si-C bond. In this chapter, we report on a two-step chlorination/azidation process (Figure 3.1) for the chemical passivation of Si(111) surfaces with azide groups, and we report on the detailed chemical and structural characterization of those surfaces.

3.2 Experimental

3.2.1 Materials and methods

Anhydrous inhibitor-free tetrahydrofuran (THF, ≥99.9%, water content <0.002%), anhydrous methanol (99.8%, water content <0.002%) and hexamethylphosphoramide (HMPA, 99%) was purchased from Sigma-Aldrich. Prior to use, HMPA is dried with calcium hydride (reagent grade, 90-95%, Sigma Aldrich) overnight. Phosphorus pentachloride (PCl_5, 99.998%) was purchased from Alfa Aesar. These reagents were used as supplied and stored in a glovebox purged with nitrogen. Silicon samples were (111)-oriented, Sb-doped, n-type Si wafers with a low miscut angle of ±0.5° and a resistivity of 0.005-0.02 ohm·cm. Samples were obtained from ITME (Poland).

Silicon wafer was cut into samples of 0.5×1 cm pieces. The crystal orientation was marked according to the flat along the side of the wafer. The silicon wafers were first sonicated in acetone and methanol for 5 min each followed by a standard RCA cleaning process. The samples were then immersed in degassed 40% NH_4F for 15 min to prepare atomically flat H-/Si(111). Chlorination was performed by treating H-/Si with PCl_5 in chlorobenzene at 95^oC for 50 min in a nitrogen-purged glovebox. The Cl-/Si(111) surfaces were then rinsed with tetrahydrofuran (THF) and methanol and exposed at 25^oC under inert atmosphere to solutions of sodium azide (NaN_3, ≥99.5%, Sigma Aldrich) in either HMPA or methanol for 5 min and 3 hrs, respectively. Following the reaction, the sample was removed from the solution and rinsed thoroughly with THF and methanol. After 5-10 min sonication in methanol, the sample was dried under streaming N_2(g).

3.2.2 Instrumentation

X-ray Photoelectron Spectroscopy: All spectra were collected in a UHV vacuum chamber maintained at a pressure of $<1.0\times10^{-9}$ Torr using an M-Probe XPS system that has been described elsewhere.[24] Monochromatic Al Kα source radiation (1486.6 eV) was incident near the middle of the sample at an angle of 35° off the surface. Photoelectrons emitted along a takeoff angle of 35° from the surface were collected by a hemispherical analyzer. The ESCA software (version 102.04, Service Physics, Inc.) available with the instrument was used for both data collection and analysis.

Infrared Spectroscopy Measurements: A Vertex 70 Fourier transform infrared (FT-IR) spectrometer (Bruker Optics, Inc.) was used to collect the attenuated total reflection infrared (ATR-IR) data of the sample. The sample was mounted on a germanium ATR crystal (*G*ATR, Harric Scientific Products, Inc.) with a grazing angle of 65°. The sample compartment was purged with dry and CO_2-eliminated air for ~5 min before each background/sample data collection.

Scanning Tunneling Microscopy and Scanning Tunneling Spectroscopy: The topographic and spectroscopic data were collected on an Omicron low-temperature UHV STM system using mechanically cut Pt/Ir tips. The vacuum pressure was maintained at $<10^{-10}$ Torr. Detailed description can be found in Chapter 2.

3.2.3 Surface coverage calculations

The surface coverage of species was estimated by referencing all peaks to the Si 2p peak at 99.4 binding eV (BeV). For multi-overlayers on the Si(111) surface, a substrate-overlayer model can be used to obtain the fractional monolayer coverage. Assuming negligible difference in the escape depths for photoelectrons excited from overlayer and substrate orbitals (i.e., λ_{ov} (ovBE) ≈ λ_{ov} (sbBE) = λ_{ov}), the overlayer thickness, d_{ov}, was obtained,[25, 26]

$$d_{\mathrm{ov}} = \ln[\left(\frac{I_{\mathrm{ov}}}{I_{\mathrm{Si}}}\right)\left(\frac{SF_{\mathrm{Si}}}{SF_{\mathrm{ov}}}\right)\left(\frac{\rho_{\mathrm{Si}}}{\rho_{\mathrm{ov}}}\right)+1]\lambda_{ov}\mathrm{Sin}\theta \tag{3.1}$$

where θ is the takeoff angle (θ =35°), ρ_{x} and I_{x} are the volumetric density and integrated area of the signal of the overlayer and Si, as indicated, and SF_{Si} and SF_{ov} are the modified sensitivity factors for the Si 2p peak and the chosen overlayer peak, respectively. Here, $SF_{\mathrm{Si\ 2p}}$=0.90, $SF_{\mathrm{C\ 1s}}$=1.00, $SF_{\mathrm{O\ 1s}}$=2.52, $SF_{\mathrm{Cl\ 2p}}$=2.40 and $SF_{\mathrm{N\ 1s}}$=1.80. The overlayer thickness was then divided by the monolayer thickness to estimate the fractional monolayer coverage.

For submonolayer (i.e., the fractional monolayer coverage Φ_{ov}<1), an alternative formulation would be[5, 6]

$$\Phi_{\mathrm{ov}} = \left(\frac{\lambda_{ov}\mathrm{Sin}\theta}{a_{\mathrm{ov}}}\right)\left(\frac{SF_{\mathrm{Si}}}{SF_{\mathrm{ov}}}\right)\left(\frac{\rho_{\mathrm{Si}}}{\rho_{\mathrm{ov}}}\right)\left(\frac{I_{\mathrm{ov}}}{I_{\mathrm{Si}}}\right) \tag{3.2}$$

where a_{ov} is the atomic diameter of the species in the overlayer.

<u>*Azide:*</u> Assuming that 100% coverage of azides on Si(111) is obtained when every atop Si(111) atom is capped by one azide molecule, then the formulation (3.2) for sub-monolayer would be appropriate for the azide coverage calculation, since it is likely Φ_{azide}<1. Furthermore, $a_{\mathrm{ov}}\rho_{\mathrm{ov}}$ can be substituted by $3n_{\mathrm{Si,surf}}$ since one azide moiety

contains three nitrogen atoms. Here, $n_{\mathrm{Si,surf}}$ is the surface number density of Si atoms (7.8×10^{14} atoms cm^{-3} for Si(111)). The escape depth through the azide layer can be approximated using the empirical equation[25] $\lambda_{ov} = 0.41a^{1.5}E^{0.5}$, where E (in eV) is the electron kinetic energy and a is the diameter of the atoms in the monolayer. The attenuation factor for Si 2p and N 1s electrons through the azide monolayer was then calculated to be 2.5 and 2.2 nm, respectively. The former value was used to simplify the calculations.

Chlorine: Similar to the azide case, Equation (3.2) was used for coverage calculations. Here, $a_{\mathrm{ov}}\rho_{\mathrm{ov}} = n_{\mathrm{Si,surf}}$ and $\lambda_{\mathrm{ov}} = 2.6$ nm for the Si 2p electrons.[25]

Carbon: The assumption of 100% coverage is slightly different from the above azide and chlorine cases. The overlayer was assumed to consist of carbon atoms packed with a solid-state volumetric density ($\rho_{\mathrm{ov}} = 1.51\times10^{23}$ atoms cm^{-3}) and to have a monolayer thickness equal to the atomic diameter of carbon in its solid state ($a_{\mathrm{ov}} = 0.19$ nm). This definition is for convenient comparison with that in the literature. Here, the escape depth for the Si 2p electron was calculated to be 1.3 nm. Then the use of the coverage calculation method would depend on the fractional coverage value.

Oxygen: Similar to carbon above, the use of the coverage calculation method also depends on the fractional value. Here, $\lambda_{\mathrm{ov}} = 2.6$ nm, $\rho_{\mathrm{ov}} = 3.46\times10^{22}$ atoms cm^{-3}, and $a_{\mathrm{ov}} = 0.31$ nm.[25]

Equivalent surface oxide monolayer calculations: The amount of surface oxide was determined by examining the high-resolution scan of the Si 2p region. Oxidation of silicon surfaces would lead to shifted Si 2p peaks located between 100 and 104 BeV, corresponding to Si^{+}-Si^{4+} oxides in contrast to the bulk Si 2p peak at 99.4 BeV. The bulk

Si $2p_{1/2}$ and Si $2p_{3/2}$ peaks were not resolved (Figure 5a) due to the scan resolution (<0.6 BeV) used in the present work. The surface oxides and bulk silicon 2p peaks were fitted to two peaks, accordingly. The peak areas were then obtained for further oxide monolayer coverage calculation.

Based on the substrate-monolayer model, the thickness of the SiO_x was determined according to the following equation:[25]

$$d_{\mathrm{SiOx}} = \ln[\left(\frac{I_{\mathrm{ov}}}{I_{\mathrm{Si}}}\right)\left(\frac{I^{\mathrm{o}}_{\mathrm{Si}}}{I^{\mathrm{o}}_{\mathrm{ov}}}\right)+1]\lambda_{\mathrm{SiOx}}\mathrm{Sin}\theta \tag{3.3}$$

where $I^{\mathrm{o}}_{\mathrm{Si}} / I^{\mathrm{o}}_{\mathrm{ov}}$ is an instrument normalization factor (1.3 for our instrument), λ_{SiOx} is, as before, the attenuation factor of the overlayer (2.6 nm).[25] The calculated thickness was divided by the thickness of a monolayer of SiO_2, 0.35 nm, to obtain the approximate monolayer coverage.

For very thin oxide monolayers, the following simple method is used to calculate the coverage. Assuming negligible differences in the photoionization cross-sections of surface and bulk Si species ($S_{\mathrm{Si,oxides}} \sim S_{\mathrm{Si,bulk}} = S_{\mathrm{Si}}$), the total observed Si 2p signal per unit surface area is[22]

$$I_{\mathrm{Si,total}} = I_{\mathrm{Si,oxides}} + I_{\mathrm{Si,bulk}} = n_{\mathrm{Si}} S_{\mathrm{Si}} d_{\mathrm{Si}} \mathrm{Sin}\theta \tag{3.4}$$

where n_{Si} is the atomic number density of Si (5.0×10^{22} atoms cm^{-3}), S_{si} is the photoionization cross-section of Si, d_{Si} is the photoelectron penetration depth (1.6 nm), and θ is, as before, the takeoff angle (35°). The measured signal from oxidized silicon species per unit surface area is given by:[22, 25]

$$I_{\mathrm{Si,oxides}} = n_{\mathrm{Si,surf}} \sigma_{si,oxides} S_{\mathrm{Si}} \tag{3.5}$$

where $\sigma_{\mathrm{Si,oxides}}$ is the equivalent monolayer coverage of SiO_x. Then we have

$$\frac{I_{\mathrm{Si,oxides}}}{I_{\mathrm{Si,total}}}=\frac{n_{\mathrm{Si,surf}}\sigma_{si,oxides}S_{\mathrm{Si}}}{n_{\mathrm{Si}}S_{\mathrm{Si}}d_{\mathrm{Si}}\mathrm{Sin}\theta}=\frac{n_{\mathrm{Si,surf}}\sigma_{si,oxides}}{n_{\mathrm{Si}}d_{\mathrm{Si}}\mathrm{Sin}\theta} \tag{3.6}$$

Substituting into eq. (3.6) yields $\sigma_{si,oxides}=5.88\times(I_{\mathrm{Si,oxides}}/I_{\mathrm{Si,total}})$.

3.3 XPS and IR analysis

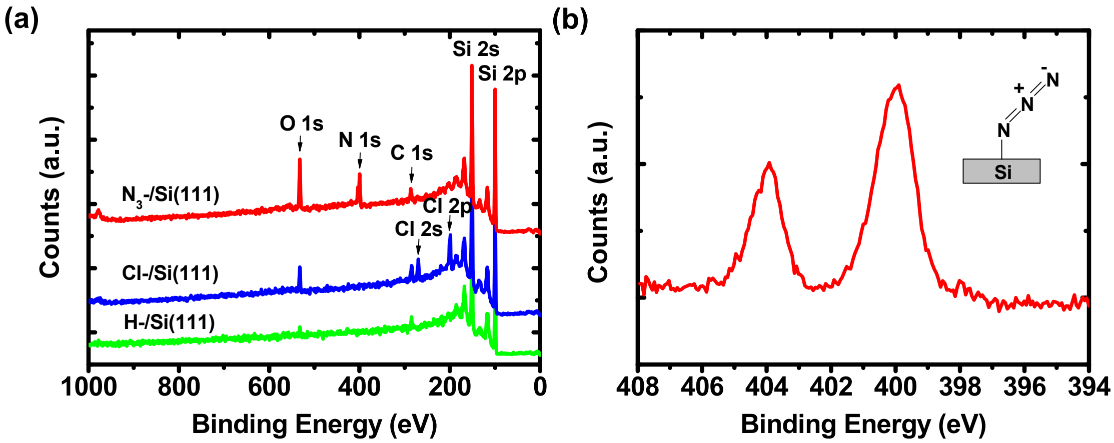

Figure 3.2. XPS analysis of azide-terminated Si(111) surfaces. (a) XPS survey scans following steps of hydrogenation, chlorination and azidation of Si(111) surfaces in Figure 3.1. (b) A high-resolution view of the N (1S) region for N_3^-/Si(111). Inset shows a schematic of the azide-silicon binding configuration. Spectroscopic characterization reveals the surface chemical changes that occur from H-/Si(111) to Cl-/Si(111) to N_3^-/Si(111).

XPS data were collected to follow the steps of the reaction scheme (Figure 3.1) and are summarized in Figure 3.2a. In the azidation step, the striking change is the partial disappearance of Cl (80-90%) and appearance of nitrogen peaks corresponding to the presence of azides. The close-up scan of the N 1s region is also shown in Figure 3.2b. Two peaks are clearly resolved at 400 and 404 eV with an intensity ratio of 2:1, similar to what is seen for azide groups on gold[27] and graphitic[28] surfaces. These characteristic peaks from azide groups show evidence for the presence of azide on the surface. Additionally, no sodium signal was observed from the azide-modified surfaces. This may rule out the possible physically adsorbed species, which may interfere with the spectrum.

Other than these significant changes, peaks from oxygen and carbon are also observable. For instance, a small amount of C and O was observed on H-terminated Si(111) (Figure 3.2a), corresponding to a 0.2±0.1 and 0.3±0.1 monolayer (ML) respectively. After chlorination, these numbers increased to 0.3±0.1 and 0.7±0.2 respectively. The peak ratio of O 1s relative to Si 2p is similar to that observed in the literature.[22] This may be due to adventitiously adsorbed species, since no SiO_x peak was observed through the above two steps (Figure 3.5). In addition, reactions of methanol and THF have also been studied in detail by Amy and coworkers.[29] Partial methoxylation of the surface may also contribute to this. Following azidation, the carbon peak remains similar to that of Cl-/Si, while O 1s increased to 1.3±0.4 ML for both samples prepared from HMPA and methanol. However, assignment of this to oxides would be not possible since the signal from SiO_x in the Si 2p region (Figure 3.5) was almost close to the noise level. It is likely that more water vapor may be adsorbed to the azidated surface while transferring samples to the XPS chamber, since a ~10° decrease in water contact angle has been observed relative to Cl-/Si.

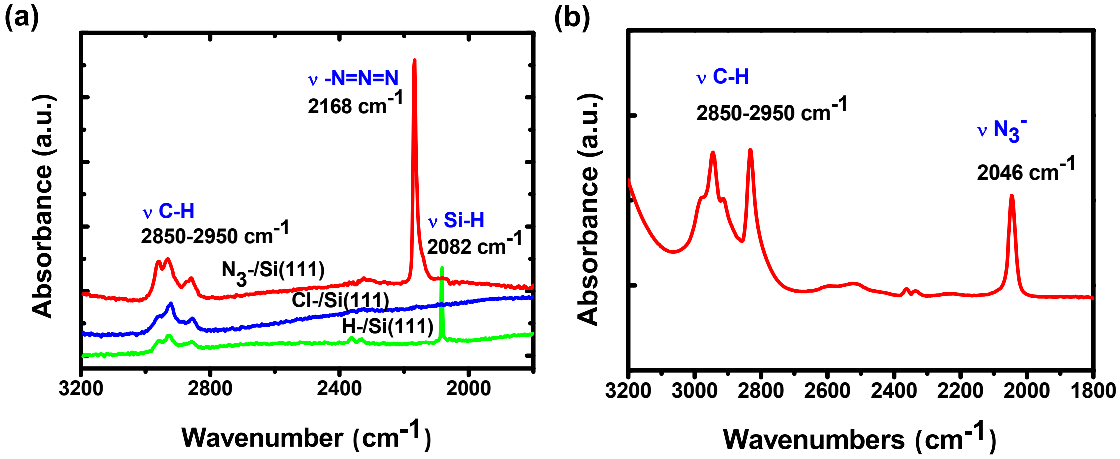

Figure 3.3. ATR-IR data from azide-terminated Si(111) surfaces. (a) IR spectra (referenced to the SiO_2-/Si(111) surfaces) following steps of hydrogenation, chlorination and azidation of silicon surfaces in Figure 3.1. (b) An IR spectrum from sodium azide in a solution of methanol. N_3-/Si(111) surfaces were prepared from the HMPA method. Similar results were also obtained from surfaces prepared from the methanol solution.

The corresponding IR spectra (referenced to SiO_2-/Si(111)) are shown in Figure 3.3a together with that of sodium azide dissolved in methanol. The observation of C-H vibrations in all spectra is due to either adventitiously adsorbed carbon or partial surface methoxylation. The disappearance of the Si-H stretch mode (2082 cm^{-1}) upon chlorination was expected.[24] The most striking feature is the appearance of a unique azide symmetric stretching mode at 2168 cm^{-1}, which is blue-shifted by ~122 and ~63 cm^{-1} with respect to either azides in solution (Figure 3.3b), or organic azides[27, 30] with nitrogen bonded to a carbon atom, respectively. These large frequency shifts suggested the formation of a covalent Si-N bond. The azide symmetric stretch at ~2170 cm^{-1} observed for silyl azide (SiH_3N_3)[31] supports this assignment.

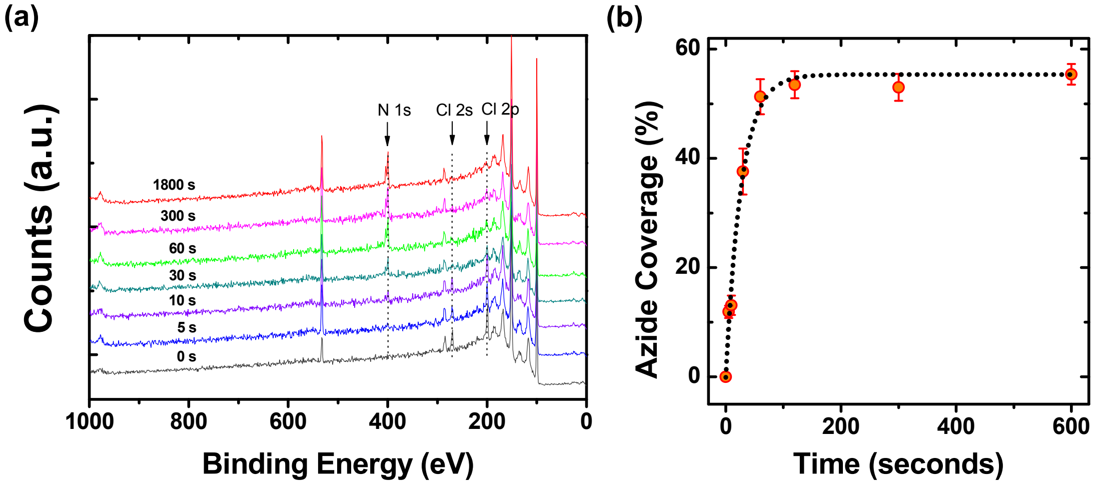

Figure 3.4. Kinetics of azidation of Si(111) surfaces. (a) XPS survey scan of azidated silicon surfaces as a function of reaction time. (b) Plot of surface coverage of azides versus time during the azidation process. The dotted line is a first-order exponential fit of the data from which one can derive a pseudo first-order rate constant of k = 0.037 s^{-1}.

Figure 3.4a shows XPS survey scans of azidated silicon surfaces as a function of reaction time. The opposite trend of the peak intensities of N and Cl elements is clearly observed. By taking the ratio of the normalized, integrated band intensities of N 1s and Si 2p peaks, the coverage of azide on Si(111) was obtained (calculated[25] assuming that 100% coverage means every atop silicon site is capped by an azide group) and plotted as a function of reaction time in Figure 3.4b (circles). For HMPA solvent, the azide coverage reaches about 55%, with a fast, pseudo first-order rate constant of 0.037 s^{-1}. This may be due to the extremely strong solvation ability of cations by HMPA. The corresponding reaction in MeOH was much slower, taking 2-3 hrs to reach a lower level of azide coverage (~25%).

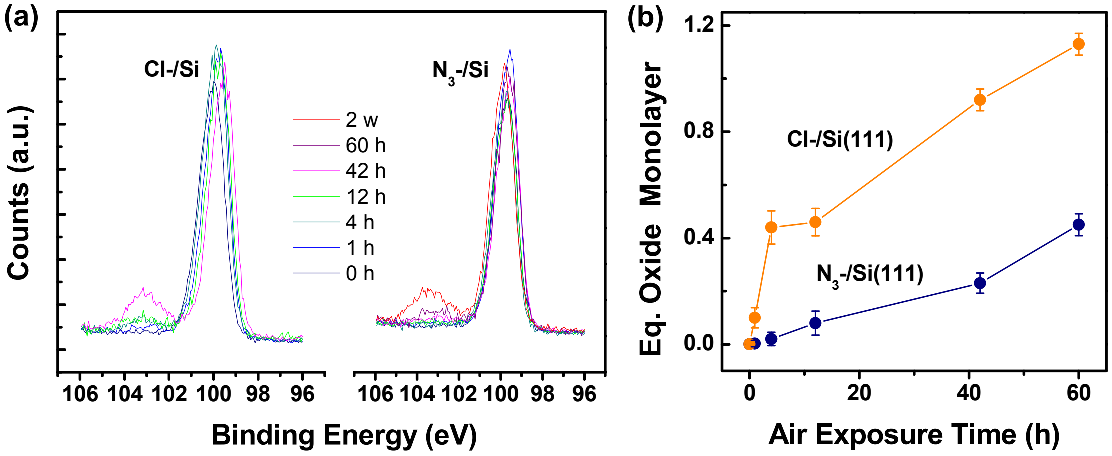

Figure 3.5. Stability of azidated Si(111) surfaces against air oxidation. (a) XPS results for the Si 2p region of azidated silicon surfaces as a function of air exposure time. (b) Plot of equivalent monolayers of SiO_2 formed on the corresponding surfaces in (a) versus time for both N_3-/Si(111) and Cl-/Si(111).

We also utilized XPS to monitor the stability of the N_3-/Si(111) surface in air (relative humidity: ~60%). These data are plotted to show the time-dependent growth of equivalent surface monolayers of SiO_2[22] and are presented in Figure 3.5b. Raw XPS spectral data are in Figure 3.5a, where only the relevant Si 2p region is presented. For freshly prepared Cl-/Si(111) and N_3-/Si(111), signals from silicon oxides at approximately 102-105 BeV are essentially at the noise level. As exposure time increases, signals from this region start to appear, indicating oxide growth on both surfaces. The N_3-/Si(111) surfaces are relatively stable in air compared to chlorinated Si(111), but a full equivalent monolayer of SiO_2 does grow after a 2 week exposure to air. The rapid initial oxidation observed for Cl-/Si(111) was absent for N_3-/Si(111), possibly because the most reactive Cl sites had been replaced with azide. The N_3-/Si(111) is unstable relative to the H_3C-/Si(111) and H_3C-CH_2-/Si(111) surfaces, both of which exhibit higher % coverages, and long-term stability in air.[6, 7]

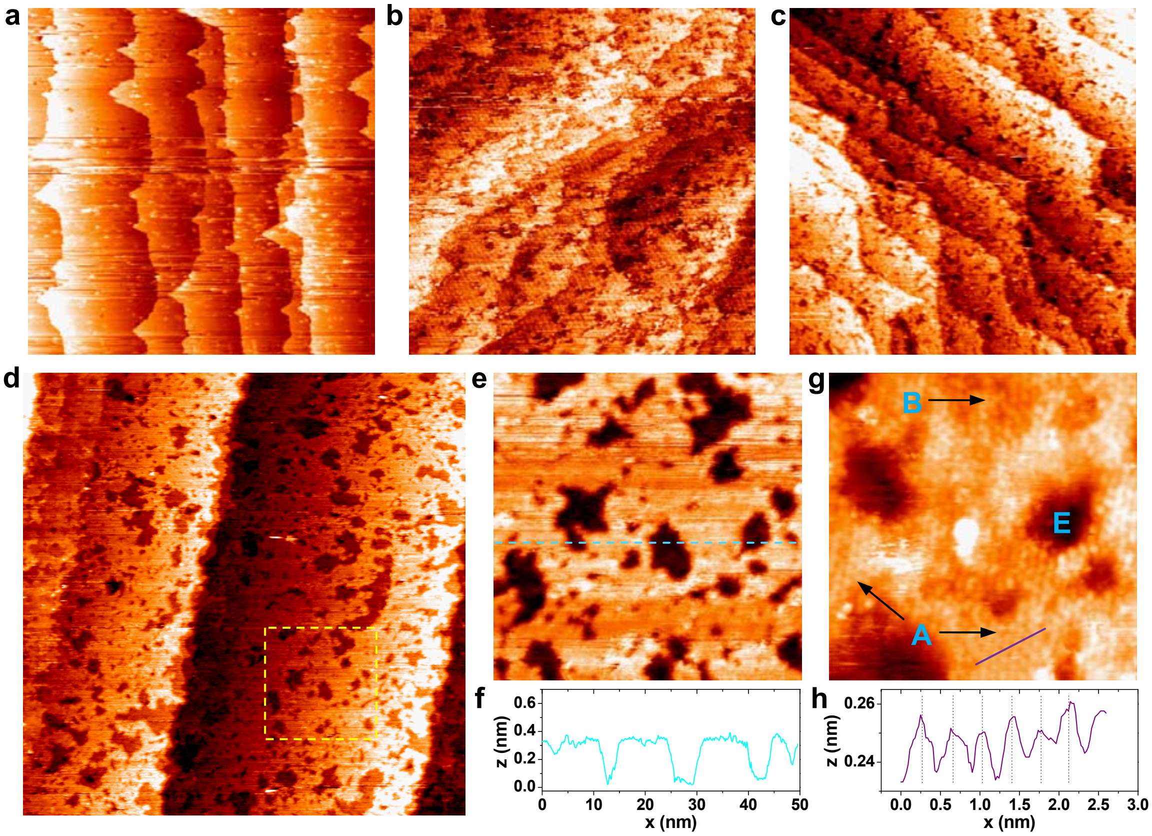

Figure 3.6. Morphology evolutions following the two-step chlorination/azidation process. Constant-current STM images of freshly prepared (a) H-, (b) Cl-, and (c) azide-terminated Si(111) surfaces. (d) Constant-current STM image of another azidated silicon sample prepared from sodium azide in methanol. (e) A close-up of the yellow square in (d). (f) A height profile along the light blue line. (g) A close-up image showing the atoms resolved on the same sample surface as (d). Other than etch pits (dark regions, labeled E), there are also ordered regions (A) and disordered regions (B) coexisting on the image. (h) A height profile along the purple line (left to right) in (g). Dotted lines with a periodicity of 0.38 nm are superimposed on the line profile. Image sizes: 200 nm × 200 nm for (a-d), 50 nm × 50 nm for (e) and 10 nm × 10 nm for (g). Height scales: 1 nm for (a-d) and 0.4 nm for (e)(g).

3.4 STM and STS analysis

The morphology of the azidated surfaces were studied by STM and the images are presented in Figure 3.6c. Figure 3.6d shows another sample with a zoom-in area (yellow box) presented in Figure 3.6e. In these images, brighter colors represent higher regions while darker colors represent lower regions. Both step edges and etch pits were observed. The etch pits are at least one silicon double-layer step lower in height (Figure 3.6f). These observations are similar to that observed from Cl-Si (Figure 3.6b),[32] indicating no significant morphology changes upon azidation. As we have discussed in Chapter 1, these etch pits mainly originate from the chlorination step, since there are significantly fewer etch pits on H-terminated surfaces (Figure 3.6a).

Figure 3.6g displays a constant-current image from the same sample as Figure 3.6d, where atoms (of unknown type) are resolved. Other than the etch pits (labeled E), two types of features are observed on the top layer: ordered (A) and disordered regions (B). Figure 3.6h shows a height profile along the line in the ordered region in Figure 3.6g. Dotted lines with a periodicity of 0.38 nm are also superimposed on the plot. Clearly, the peaks representing atoms are roughly equally spaced in distance with a periodicity of 0.38 nm. This is the characteristic distance between the nearest neighbor silicon atop surface atoms on an unreconstructed Si(111) surface. However, there are also disordered regions (B in Figure 3.6g) where the next neighbor distances are generally not equal to 0.38 nm (height profile not shown here).

To identify the chemical groups on the surface and so as to gain deeper understanding of the surface chemistry, current imaging tunneling spectroscopy (CITS) data are collected (at -1.0V and 77K) from these surfaces (Figure 3.7b), including step and etch pit edges (red), terrace sites (light blue), and regions of high conductivity (green). The simultaneously collected topographic image is presented in Figure 3.7a.

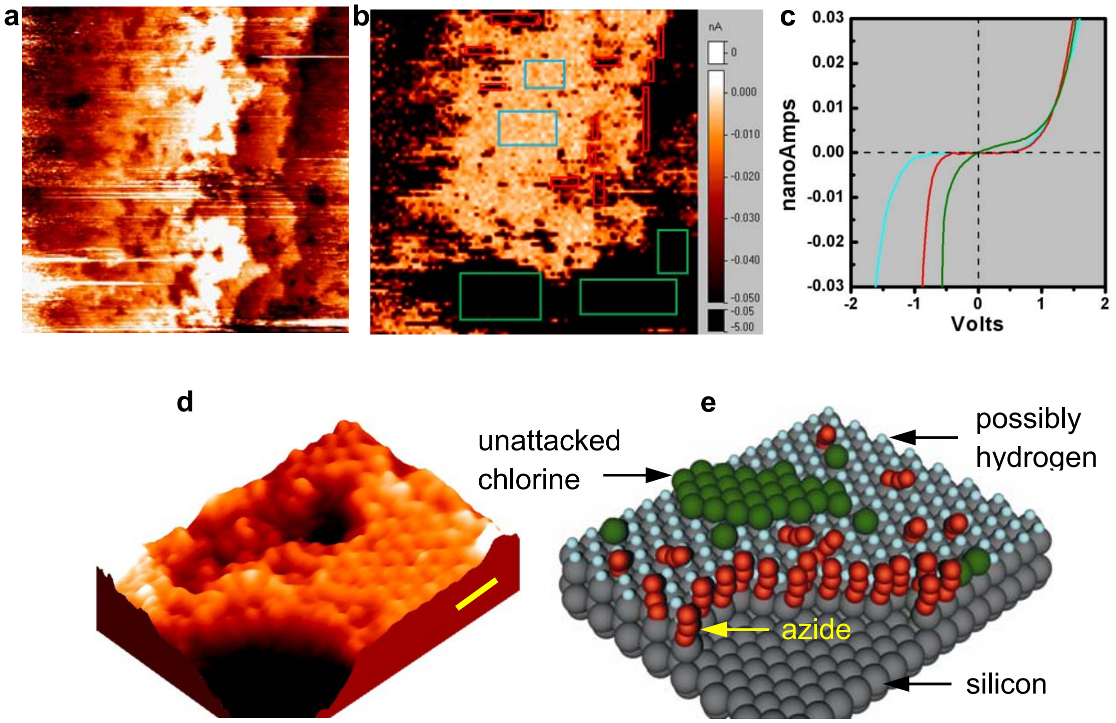

Figure 3.7. Identification of surface chemical groups on azidated Si(111). (a) The topology of the azidated Si(111) surface (at -1.0 V, scale bar: 20 nm). (b) The corresponding CITS image of the same area as (a) together with (c) the averaged STS data (*color-coded*) from various regions of the surface. In this image, *red boxes* encircle step and etch pit edges, *light blue boxes* encircle terrace sites, and *green boxes* encircle regions of high surface conductivity. (d) Constant current STM image of the same Si(111) surface. V_b = 1.85 V, I_t = 0.12 nA, temperature = 77K, scale bar: 1 nm; (e) Graphic illustrating the assigned chemical groups on the azidated Si(111) surface.

Three distinct regions (color-coded on Figures 3.7b-c) were found in terms of yielding distinct I-V tunneling curves, suggesting areas with different chemical origins.

The terrace sites (light blue encircled regions) showed a band gap of about 1.5 V, which is close to that (1.6 V) observed for H-/Si(111),[32] while step and etch pit edges (red) exhibit a gap value of about 0.8 V. The high conductance regions (green) appear similar to that of Cl-/Si(111), namely, nonzero slope or nonzero density of states at zero bias.[32] We thus tentatively assign the red-encircled regions as azide-covered (see the drawing of Figure 3.7e). Figure 3.7d displays a constant-current 3D image from N_3-/Si(111) with low azide coverage (~25%), where atoms are resolved. Upon higher coverage of azide (55%), the three distinct classes of I-V traces are still observed, but are more evenly distributed over the surface (not shown here).[1]

3.5 Conclusion

In this chapter, we have described methods to covalently attach the azide functionality to Si(111) surfaces through a two-step chlorination/azidation process. It is shown to yield different azidation kinetic rates, different final azide coverages, and different surface-area distributions, depending upon the azidation solvent. Similar to the previously reported HC≡C-/Si(111) surface,[23] the N_3-/Si(111) surface should be useful for secondary functionalization through the Cu(I)-catalyzed Huisgen 1,3-dipolar cycloaddition ("click" chemistry).[33] Alternatively, reduction of the N_3-/Si(111) surface using the Staudinger reduction method[34] would be expected to produce an amine-terminated surface for the coupling of carboxylic acid molecules.

3.6 References

1. Cao, P.G., Xu, K. & Heath, J.R. Azidation of silicon(111) surfaces. *J Am Chem Soc* **130**, 14910-14911 (2008).

2. Buriak, J.M. Organometallic chemistry on silicon and germanium surfaces. *Chem Rev* **102**, 1271-1308 (2002).
3. Linford, M.R. & Chidsey, C.E.D. Alkyl monolayers covalently bonded to silicon surfaces. *J Am Chem Soc* **115**, 12631-12632 (1993).
4. Linford, M.R., Fenter, P., Eisenberger, P.M. & Chidsey, C.E.D. Alkyl monolayers on silicon prepared from 1-alkenes and hydrogen-terminated silicon. *J Am Chem Soc* **117**, 3145-3155 (1995).
5. Nemanick, E.J. et al. Chemical and electrical passivation of single-crystal silicon(100) surfaces through a two-step chlorination/alkylation process. *J Phys Chem B* **110**, 14770-14778 (2006).
6. Webb, L.J. et al. High-resolution soft X-ray photoelectron spectroscopic studies and scanning auger microscopy studies of the air oxidation of alkylated silicon(111) surfaces. *J Phys Chem B* **110**, 23450-23459 (2006).
7. Yu, H.B. et al. Scanning tunneling microscopy of ethylated Si(111) surfaces prepared by a chlorination/alkylation process. *J Phys Chem B* **110**, 23898-23903 (2006).
8. Jaeckel, B., Hunger, R., Webb, L.J., Jaegermann, W. & Lewis, N.S. High-resolution synchrotron photoemission studies of the electronic structure and thermal stability of CH3- and C2H5-functionalized Si(111) surfaces. *J Phys Chem C* **111**, 18204-18213 (2007).
9. Haick, H., Hurley, P.T., Hochbaum, A.I., Yang, P.D. & Lewis, N.S. Electrical characteristics and chemical stability of non-oxidized, methyl-terminated silicon nanowires. *J Am Chem Soc* **128**, 8990-8991 (2006).
10. Green, J.E., Wong, S.J. & Heath, J.R. Hall mobility measurements and chemical stability of ultrathin, methylated Si(111)-on-insulator films. *J Phys Chem C* **112**, 5185-5189 (2008).
11. Strother, T., Cai, W., Zhao, X.S., Hamers, R.J. & Smith, L.M. Synthesis and characterization of DNA-modified silicon (111) surfaces. *J Am Chem Soc* **122**, 1205-1209 (2000).
12. Pike, A.R. et al. DNA on silicon devices: On-chip synthesis, hybridization, and charge transfer. *Angew Chem Int Edit* **41**, 615-616 (2002).
13. Linford, M.R. & Chidsey, C.E.D. Surface functionalization of alkyl monolayers by free-radical activation: Gas-phase photochlorination with Cl-2. *Langmuir* **18**, 6217-6221 (2002).

14. Rohde, R.D., Agnew, H.D., Yeo, W.S., Bailey, R.C. & Heath, J.R. A non-oxidative approach toward chemically and electrochemically functionalizing Si(111). *J Am Chem Soc* **128**, 9518-9525 (2006).
15. Fellah, S. et al. Grafting and polymer formation on silicon from unsaturated Grignards: I - Aromatic precursors. *J Phys Chem B* **110**, 1665-1672 (2006).
16. Fellah, S. et al. Grafting and polymer formation on silicon from unsaturated Grignards: II. Aliphatic precursors. *J Phys Chem B* **111**, 1310-1317 (2007).
17. Ciampi, S. et al. Functionalization of acetylene-terminated monolayers on Si(100) surfaces: A click chemistry approach. *Langmuir* **23**, 9320-9329 (2007).
18. Marrani, A.G. et al. Functionalization of Si(100) with ferrocene derivatives via "click" chemistry. *Electrochim Acta* **53**, 3903-3909 (2008).
19. Plass, K.E., Liu, X.L., Brunschwig, B.S. & Lewis, N.S. Passivation and secondary functionalization of allyl-terminated Si(111) surfaces. *Chem Mater* **20**, 2228-2233 (2008).
20. Rivillon, S., Brewer, R.T. & Chabal, Y.J. Water reaction with chlorine-terminated silicon (111) and (100) surfaces. *Appl Phys Lett* **87**, 173118 (2005).
21. Rivillon, S. et al. Chlorination of hydrogen-terminated silicon(111) surfaces. *J Vac Sci Technol A* **23**, 1100-1106 (2005).
22. Webb, L.J. & Lewis, N.S. Comparison of the electrical properties and chemical stability of crystalline silicon(111) surfaces alkylated using Grignard reagents or olefins with Lewis acid catalysts. *J Phys Chem B* **107**, 5404-5412 (2003).
23. Hurley, P.T., Nemanick, E.J., Brunschwig, B.S. & Lewis, N.S. Covalent attachment of acetylene and methylacetylene functionality to Si(111) surfaces: Scaffolds for organic surface functionalization while retaining Si-C passivation of Si(111) surface sites. *J Am Chem Soc* **128**, 9990-9991 (2006).
24. Bansal, A., Li, X.L., Yi, S.I., Weinberg, W.H. & Lewis, N.S. Spectroscopic studies of the modification of crystalline Si(111) surfaces with covalently-attached alkyl chains using a chlorination/alkylation method. *J Phys Chem B* **105**, 10266-10277 (2001).
25. Haber, J.A. & Lewis, N.S. Infrared and X-ray photoelectron spectroscopic studies of the reactions of hydrogen-terminated crystalline Si(111) and Si(100) surfaces with Br-2, I-2, and ferrocenium in alcohol solvents. *J Phys Chem B* **106**, 3639-3656 (2002).
26. Briggs, D. & Seah, M.P. Practical surface analysis, Edn. 2nd. (Wiley; Salle + Sauerländer, Chichester; New York; 1990).

27. Collman, J.P., Devaraj, N.K., Eberspacher, T.P.A. & Chidsey, C.E.D. Mixed azide-terminated monolayers: A platform for modifying electrode surfaces. *Langmuir* **22**, 2457-2464 (2006).

28. Devadoss, A. & Chidsey, C.E.D. Azide-modified graphitic surfaces for covalent attachment of alkyne-terminated molecules by "click" chemistry. *J Am Chem Soc* **129**, 5370-5371 (2007).

29. Amy, S.R. et al. Investigation of the reactions during alkylation of chlorine-terminated silicon (111) surfaces. *J Phys Chem C* **111**, 13053-13061 (2007).

30. Collman, J.P., Devaraj, N.K. & Chidsey, C.E.D. "Clicking" functionality onto electrode surfaces. *Langmuir* **20**, 1051-1053 (2004).

31. Ebsworth, E.A. & Mays, M.J. The preparation and properties of silyl azide. *J Chem Soc*, 3450-3454 (1964).

32. Cao, P.G., Yu, H.B. & Heath, J.R. Scanning tunneling microscopy and spectroscopy of wet-chemically prepared chlorinated Si(111) surfaces. *J Phys Chem B* **110**, 23615-23618 (2006).

33. Devaraj, N.K. & Collman, J.P. Copper catalyzed azide-alkyne cycloadditions on solid surfaces: Applications and future directions. *Qsar Comb Sci* **26**, 1253-1260 (2007).

34. Gololobov, Y.G., Zhmurova, I.N. & Kasukhin, L.F. 60 years of staudinger reaction. *Tetrahedron* **37**, 437-472 (1981).

Chapter 4

Electrical Properties of Graphene Wrinkles and Nanoribbons

Part of the contents presented in this chapter are based on Xu, K., Cao, P.G. and Heath, J.R. "Scanning tunneling microscopy characterization of the electrical properties of wrinkles in exfoliated graphene monolayers," *Nano Lett*, 9, 4446-4451 (2009). (Ref.[1])

4.1 Introduction

Graphene refers to a monolayer of carbon atoms tightly packed into a two-dimensional (2D) honeycomb lattice. The discovery of graphene in an isolated state[2, 3] has generated widespread research interest.[4-6] The linear dispersion spectrum of graphene causes its charge carriers to behave like massless Dirac fermions, leading to various novel electrical properties that are of fundamental interest. Meanwhile, the unique structure of graphene, in which all atoms are surface atoms, makes its electronic band structure and hence electrical properties extremely sensitive to size effects, surface curvatures, as well as environmental interactions.

4.1.1 Wrinkles in graphene

Graphene initially appeared to be a strictly 2D electronic system, and quantum Hall effects were observed in graphene up to room temperature.[7] On the other hand, theory has predicted that strictly 2D crystals are thermodynamically unstable and therefore should not exist at any finite temperature.[8]

This contradiction was reconciled by recent transmission electron microscopy (TEM) studies on suspended graphene, in which a microscopically corrugated three-dimensional structure was revealed,[9, 10] overturning the naïve picture of graphene being a flat 2D crystal. The <1 nm local corrugations ("ripples") discovered in these TEM studies are believed to be intrinsic,[11] and so are important for understanding graphene electrical properties.[5, 12-16] The low resolution of TEM, especially in the vertical direction, however, limits further detailed studies of these corrugations, and how those corrugations can influence the graphene properties. In addition, the structure and properties of suspended graphene may be fundamentally different from graphene deposited on SiO_2 substrates, the most widely studied form of graphene.

Scanning tunneling microscopy (STM) provides a valuable alternative, which probes morphology and electrical properties at atomic resolution in all three dimensions. Atomically resolved STM topographs of graphene on SiO_2 substrates have been reported,[17-21] from which the height of graphene ripples was determined to be 3-5 Å. Meanwhile, attempts to correlate local electrical properties with the observed ripples have achieved only limited success.[21-23]

In this chapter, we report on the STM study of a new class of corrugations in monolayer graphene sheets that have been largely neglected in previous studies, i.e., wrinkles ~10 nm in width and ~3 nm in height. We found such corrugations to be ubiquitous in graphene, and have distinctly different properties in comparison to other regions of graphene that only contain small ripples. In particular, a “three-for-six” triangular pattern of atoms is exclusively and consistently observed on wrinkles, suggesting the local curvature of the wrinkle is a perturbation that breaks the six-fold symmetry of the graphene lattice. Through scanning tunneling spectroscopy (STS), we further demonstrate that the wrinkles have lower electrical conductance when compared to other regions of graphene, and are characterized by the presence of midgap states, which is in agreement with recent theoretical predictions. Our results suggest that, in addition to the previously investigated, low-amplitude ripples, these larger wrinkles likely play an important role in determining the electrical properties of graphene sheets.

4.1.2 Graphene nanoribbons

Although graphene has drawn tremendous attention for studies of its fundamental structural and electronic properties in recent years, the absence of an energy gap in graphene poses a challenge for conventional semiconductor field-effect transistor (FET) device operations.[24] Previous studies have shown that an energy gap can be opened up by patterning graphene into ribbons ~10 nm in width.[25-28] This is explained in terms of a quantum size effect, where the initially 2D carriers are confined into a 1D system.

Experimentally, individual graphene nanoribbons (GNRs) have been fabricated through conventional e-beam lithography (EBL) and individually addressed for transport measurement characterizations.[29, 30] However, the measurement results often vary from sample to sample due to the disorders introduced along the GNR edges during the lithography process. The origin of the energy gap is therefore complicated in this situation. Various theoretical scenarios, including, for example, Coulomb blockade in a series of quantum dots[31] and edge disorder-induced Anderson localization[32] have been invoked to explain the observed large sample variations. Large number of GNRs fabricated in parallel could in overall average out the edge variations and give more consistent results. To our knowledge, such parallel GNR arrays have not been investigated due to the difficulties involved in the fabrication process.

In the remainder of this chapter, we describe our studies on high-density parallel GNR arrays, with the aim of elucidating the effects of GNR width and number of graphene layers on the formation of energy gaps in GNRs. Electron transport in all of our GNR devices exhibits thermally activated behavior, regardless of number of layers: conductance decreases with decreasing temperature. This contrasts with the behavior in “bulk” graphene film, the conductance of which generally increases as temperature decreases.[25] Due to the measurement of large numbers of parallel GNRs (~80) at once in our study, variations observed previously on individual GNR devices are averaged out in our studies. Therefore, we have observed smoother and more consistent development of the depressed conductance region versus gate voltage as temperature decreases. More importantly, we have also for the first time clearly observed how the properties of GNRs evolve as a function of the number of graphene layers, while fixing the width of GNRs to be exactly the same. We found the band gap (and so the on-off ratio) decreases as the number of layers increases. These results suggest that, in addition to single layer graphene, GNRs of different thicknesses can also be harnessed as different building blocks for engineering GNRs for FET applications.

4.2 Experimental

4.2.1 Fabrication of graphene sheets

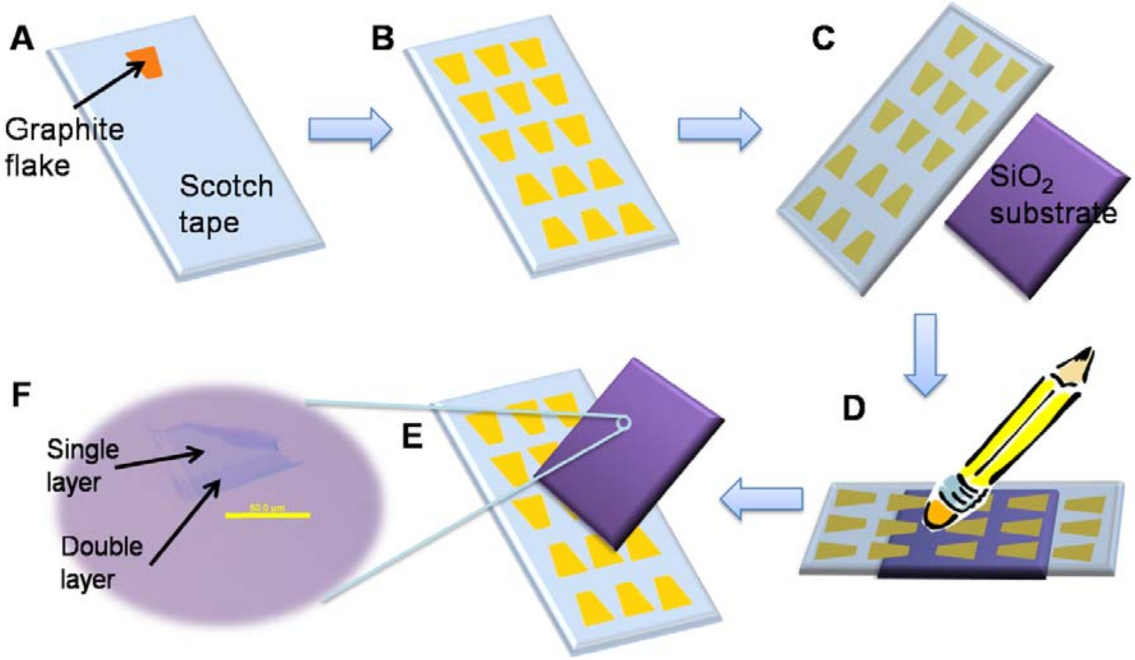

Figure 4.1. Process flow schematics for the fabrication of graphene sheets. (A): A thin Kish graphite flake is stuck onto Scotch tape. (B): By folding and peeling the tape ~10 times, the graphite flake is exfoliated into multiple thinner flakes, covering the entire tape surface. (C): The Scotch tape is turned over, and the graphite flakes on the surface are brought into contact with a freshly cleaned SiO_2 substrate. (D): An eraser is used to rub the back of the tape, to ensure close contact between the graphite flakes and the substrate. (E): The Scotch tape is peeled off from the substrate, leaving graphene sheets and other thin graphitic layers on the SiO_2 substrate. (F): Graphene sheets on the surface are identified though an optical microscope. Single-layer and double-layer parts of the graphene sheet (as confirmed through spatially resolved Raman spectroscopy) are labeled on graph. Scale bar: 50 μm.

The monolayer graphene sheets investigated in this study were fabricated on insulating SiO_2 substrates through mechanical exfoliation of Kish graphite flakes.[3, 33] The detailed process flow is presented in Figure 4.1. It should be noted that this process is time-consuming and low-yielding, and the locations of the resultant graphene sheets are uncontrolled.

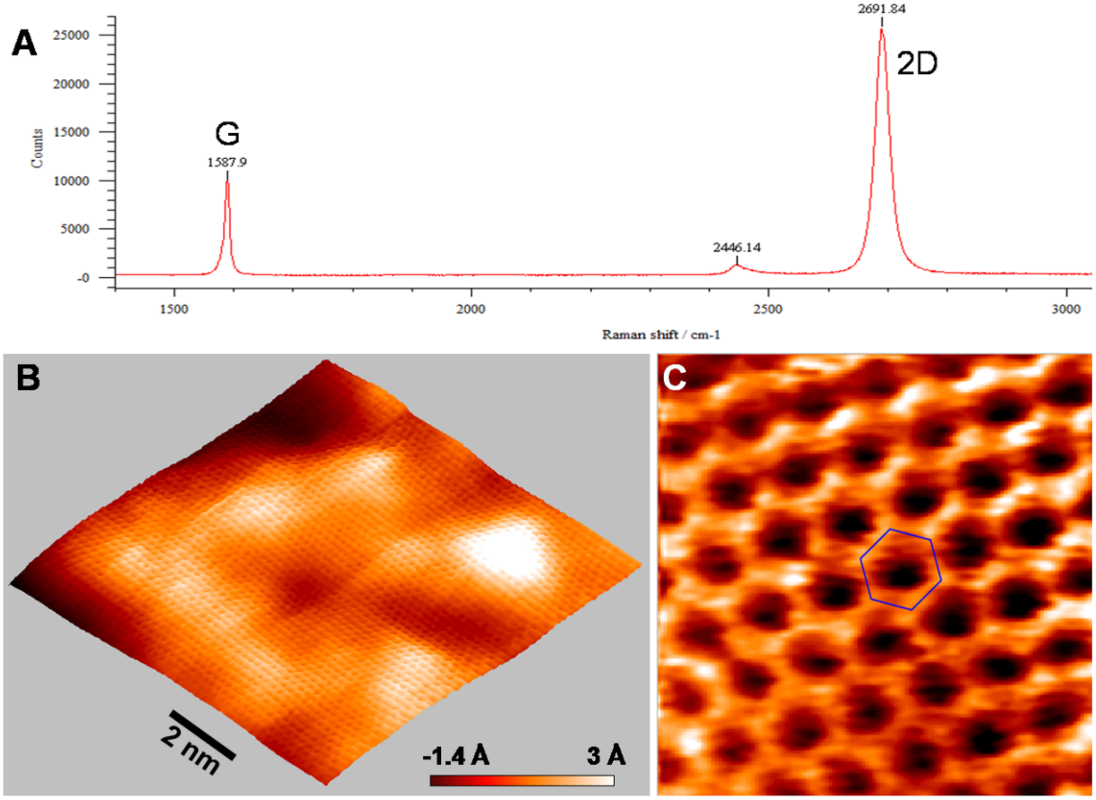

Figure 4.2. Raman spectrum and STM topography of a typical graphene sample. (A): Raman spectrum of the graphene sample. **(B):** Atomically resolved constant-current STM topograph (V_b = 0.5 V, I = 0.22 nA) of the graphene sample. **(C):** A close-up of the honeycomb lattice. The blue hexagon has sides of 1.42 Å.

Monolayer graphene sheets ~20 µm in size were optically identified, and unambiguously confirmed through spatially resolved Raman spectroscopy. As shown in

Figure 4.2A, a symmetric single peak is observed at ~2700 cm^{-1} (2D band) in the Raman spectrum, and the peak height is larger than the G band at ~1580 cm^{-1}. Both features are characteristic of pristine monolayer graphene sheets.[34, 35] Ti/Au electrodes were contacted to the fabricated graphene sheets using electron-beam lithography, and Hall measurements revealed room-temperature carrier mobilities of >6,000 cm^2/Vs, which is typical of high-quality graphene at room temperature.[4]

For STM measurements, the graphene sheets were then contacted at all edges with gold, so that the tunneling current diffused in-plane through the gold film. The electrodes defined in the previous step served as guides for locating the graphene sheets using STM (Figure 4.3). As in previous chapters, STM studies were performed using an Omicron low-temperature UHV STM system with mechanically cut Pt/Ir tips. All STM data were taken at liquid nitrogen (77 K) or liquid helium (4 K) temperatures, and a vacuum of better than 10^{-10} Torr was maintained during experiment.

4.2.2 Fabrication of graphene nanoribbons

Our GNR devices were prepared using a superlattice nanowire pattern (SNAP) transfer technique.[36] SNAP uses a template consisting of alternating layers of GaAs/$Al_xGa_{(1-x)}As$, which is grown by molecular-beam epitaxy (MBE) on top of GaAs wafers, for nanowire (NW) patterning. Through selective etching of either GaAs or $Al_xGa_{(1-x)}As$, layer thickness can be translated to the nanowire width. In principle, this width can be as thin as a few atomic layers since MBE is capable of growing with atomic resolution.

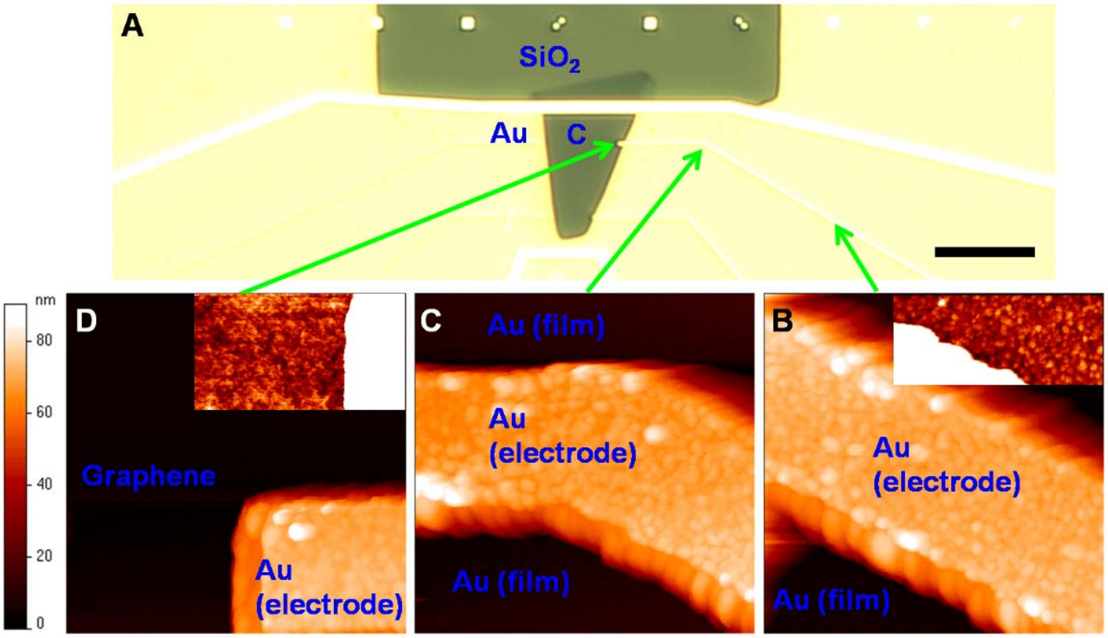

Figure 4.3. Locating the graphene sheet in STM. STM only works for conducting surfaces. To prevent the STM tip from crashing into the sample, it's essential to avoid scanning over insulating surfaces, including the SiO_2 substrate used in this study. On the other hand, positioning of the STM tip under optical microscope has poor location control (~100 μm). This obstacle can be overcome by following the method described here. **(A):** An optical microscope image of a graphene device for STM study. Graphene is labeled as "C" for carbon. Scale bar: 10 μm. The graphene sheet is contacted at all edges with gold, so that the tunneling current diffuses in-plane through the gold film. Under optical microscope, the STM tip can be easily positioned on the conductive gold film (~500 μm × 500 μm). **(B)-(C):** STM topographs (800 nm × 800 nm) demonstrating how the graphene sheet is located for STM imaging. Large scale (~2 μm) scans are first performed to find the raised electrodes in the Au film. The graphene sheet is then located by tracing the electrodes. **(B):** Topograph of an electrode when the tip is far from graphene. Inset shows the topograph of the gold film near the electrode (white) with a 5 nm height scale: At this scale nanoscale gold islands are clearly observed. **(C):** By tracing along the electrode, the tip is moved closer to graphene, and the turn in the electrode unequivocally identifies the tip position on the gold film. **(D):** Topograph obtained at the end of the electrode, where the graphene sheet is reached [cf. (A)]. Inset shows the topograph of the graphene sheet near the electrode (white) on a small (2 nm) height scale: ripples in the graphene are observed.

Figure 4.4 shows representative optical images, illustrating the fabrication process. A thin layer of SiO_2 (~10 nm) was first deposited onto a graphene sheet resting on 300 nm SiO_2/Si substrate (Figure 4.4ab). This is to protect graphene from being etched away during the following reactive ion etching (RIE) steps. A template of an array of metal nanowires (for example, Pt) was then stamped onto and securely bonded to the surface (Figure 4.4c) with a thin layer of epoxy (EpoxyBond 110, Allied High Tech, Rancho Dominguez, CA). The NW array was obtained by e-beam evaporation of Pt onto the raised edges of a differentially etched edge of a GaAs/$Al_xGa_{(1-x)}$As superlattice wafer (IQE, Cardiff, UK).[36] In this way, the atomic control over the film thicknesses of the superlattice stack was translated into control over the width and spacing of NWs. The superlattice and extra exposed epoxy were then removed via selective wet and RIE etch, respectively (Figure 4.4d).

Before the NW patterns were transferred into the underlying graphene film, EBL was used to define a 50 nm thick Al_2O_3 mask for the monolithic contact electrodes (Figure 4.4e). After pattern transfer (Figure 4.4f) and removal of the mask (Figure 4.4g), the so-defined large blocks of graphene (>500 nm in width) were then contacted by Ti/Au electrodes (Figure 4.4h). An advantage of this contact by larger areas of graphene is that the Schottky barrier formation by metal electrodes is absent. The top platinum nanowires and the protecting SiO_2 layer over the nanoribbons are not removed in the following transport measurements and in some cases, the platinum nanowires can be employed as a top gate.

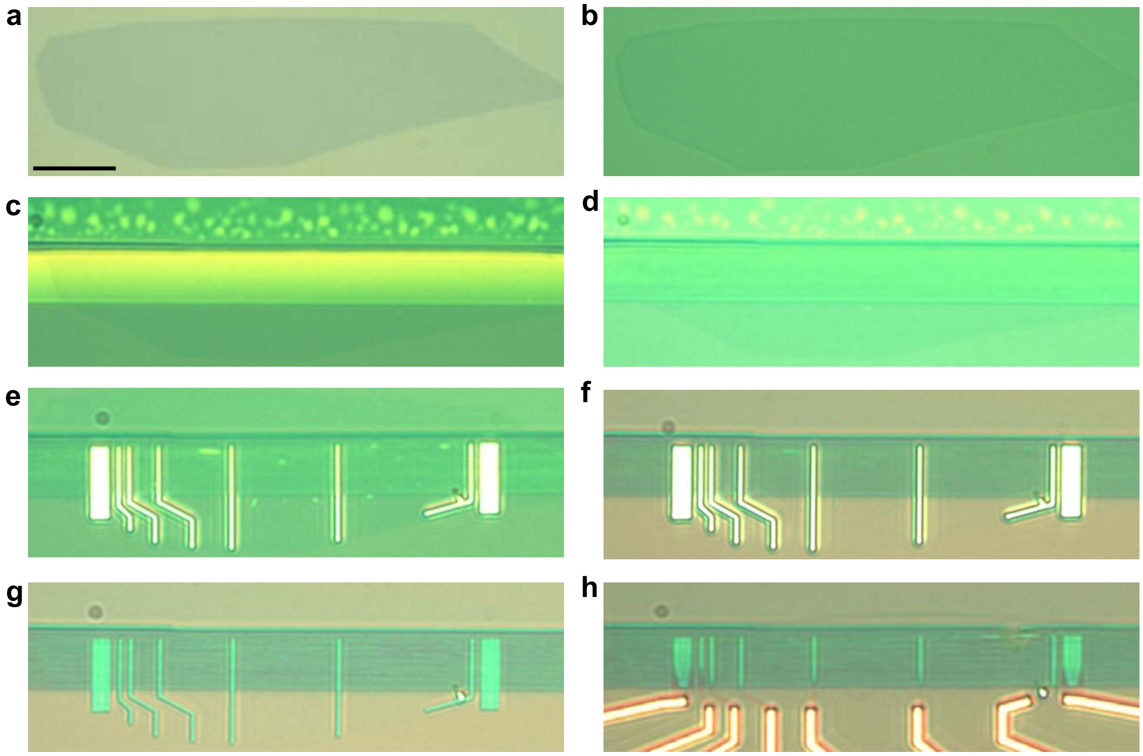

Figure 4.4. Representative bright-field optical images following the GNR fabrication process. (a) Exfoliated graphene on 300 nm SiO_2/Si substrate. (b) Evaporation of 18 nm SiO_2 protection layer, covering both graphene and substrate. (c) Stamping of SNAP Pt nanowires onto graphene via epoxy bonding. (d) Extra epoxy in between nanowires removed by RIE in a 40 MHz Unaxis SLR parallel-plate RIE system ~5 min with O_2 (10 sccm, 5 mTorr, 40 W). (e) Evaporation of 50 nm thick Al_2O_3 mask to define the monolithic contacts. Spacings between the masks were adjusted so as to define GNRs of different lengths (ranging from 0.5 to ~50 μm) but of the same width. (f) Both nanoribbon and electrode patterns were transferred into the graphene film. Exposed SiO_2 and underlying graphene (not protected by Al_2O_3 mask and Pt nanowires) were removed sequentially by highly directional RIE with ~4 min CF_4/He (20/30 sccm, 5 mTorr, 40 W) and with ~2 min O_2 plasma (10 sccm, 5 mTorr, 40W). (g) Al_2O_3 Mask removed by ~30 minutes in 10% H_3PO_4 + 90% H_2O. (h) Evaporation of Ti/Au (20/200 nm) to make metal contacts. The scale bar is 10 μm and applies for all images.

The conductance of GNRs was measured using a standard lock-in technique. A low-noise function generator (DS360, Stanford Research System) was used to supply an AC signal (100 μV at 11 Hz) to the device and the output signal was fed into a lock-in amplifier (SR830, Stanford Research System). The time constant and slope used in the experiments were 300 ms and 12 dB, respectively. The heavily doped silicon substrate below the 300 nm SiO_2 served as a bottom gate electrode to tune the carrier density in the GNRs. The gate voltages were supplied by a Keithley 2400 source meter. Temperature-dependent experiments were carried out in a SQUID cryostat (MPMS-XL, Quantum Design, CA). A program written with Labview 7.1 was used to control the operations.

4.3 Structural and electrical characterizations of graphene wrinkles

Figure 4.2B gives the constant-current STM topograph obtained from a typical graphene device. Atomically resolved, clear honeycomb structures were observed for all samples, with bond lengths in agreement with the known graphene lattice constant (Figure 4.2C). The same honeycomb structures are obtained independent of the specific parameters used for imaging.

No lattice defects were ever observed during our atomically resolved STM study over an accumulated area of ~10^4 nm^2 on different samples, corresponding to >10^5 atoms. This is in agreement with the measured high carrier mobilities, but in contrast with STM results obtained on graphene epitaxially grown on conductive substrates, in which lattice defects are observed at the nanometer scale.[37] Surface corrugations (ripples) of ~4 Å in height are observed for most regions of our graphene samples (Figure 4.2B), in agreement with previous studies.[17-21]

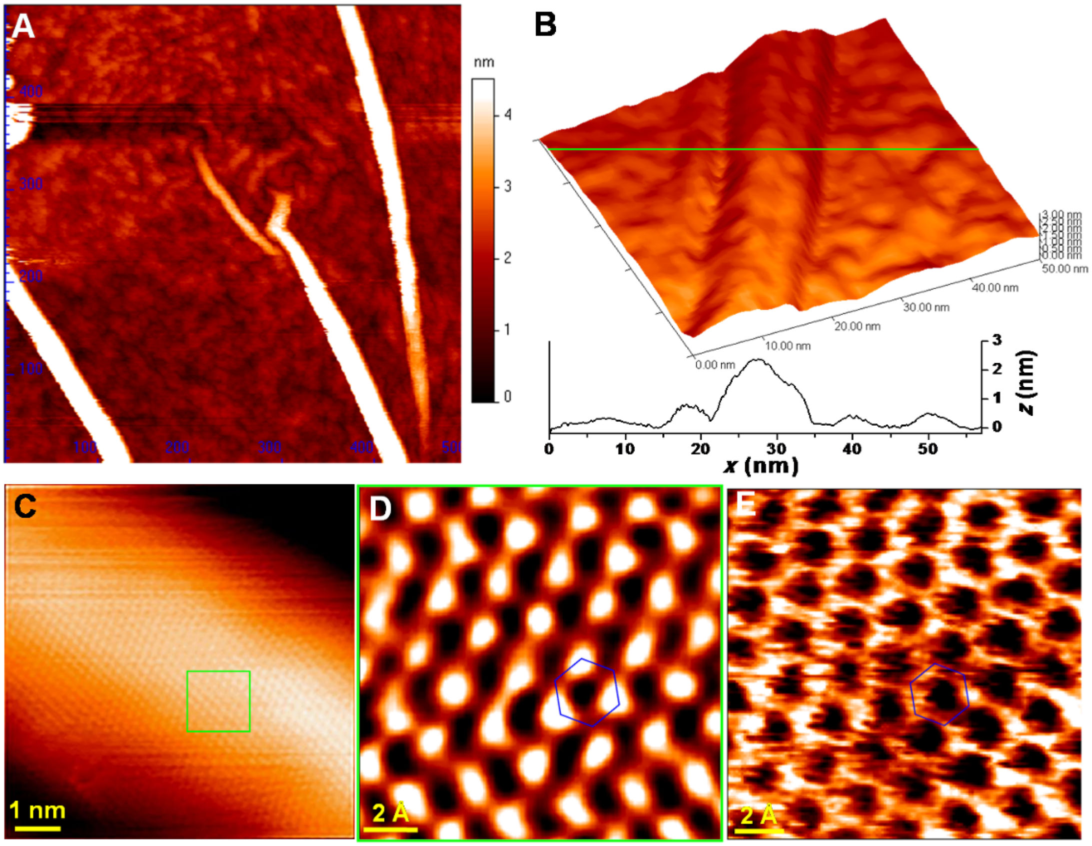

Figure 4.5. STM topographs of graphene wrinkles. (A): A large-area (500 nm by 500 nm) scan of wrinkles in a graphene sheet. A small color scale is used to accentuate the coexisting small ripples. The largest height in this topograph is ~6 nm. (B): A three-dimensional plot of the topograph of a typical wrinkle structure. The coexisting ripple structures are also observed. A height profile through the green line is given. (C): Atomically resolved topograph obtained on the top of the wrinkle. Scale bar: 1 nm. (D): A close-up of the observed “three-for-six” triangular pattern on the wrinkle, corresponding to the green square in (C). Scale bar: 2 Å. The blue hexagon has sides of 1.42 Å, corresponding to the size of one hexagonal carbon ring. (E): Atomically resolved topograph taken right next to the wrinkle, on a “flat” region of the same graphene sheet. Scale bar: 2 Å. The blue hexagon has sides of 1.42 Å.

In addition to the previously observed ripples, we also frequently encounter larger-amplitude wrinkle-like structures that are 5 to 20 nm in width, 2 to 5 nm in height, and have lengths from ~100 nm to ~1 μm. Figure 4.5A presents the topograph obtained from a region of a graphene sample in which multiple wrinkles are observed. The wrinkles appear to be continuous parts of the graphene sheet that buckle up from the underlying substrate (Figure 4.5B), reminiscent of wrinkles that spontaneously occur in thin elastic sheets under stress.[38] However, quite different from a conventional thin sheet, the observed graphene wrinkles are found to be accompanied (both on and near the wrinkles) by the ~4 Å small ripples that are known to be intrinsic[11] to graphene (Figure 4.5B).

Wrinkle-like structures have been seen before in TEM images of suspended graphene sheets[34] and in STM and high-resolution scanning electron microscope (SEM) images of graphene grown on conducting substrates,[39, 40] but their structure and properties have not been carefully characterized. Moreover, wrinkles were not previously known to be present in the high-mobility, mechanically exfoliated graphene sheets on SiO_2 substrates, presumably due to their low occurrence rate and small physical dimensions: features with such dimensions are hard to detect optically, or with an SEM or atomic force microscope. High-resolution STM topographs were only recently achieved for graphene sheets on insulting substrates.[17-21]

The wrinkle structures were found to be ubiquitous on exfoliated graphene sheets on SiO_2. Wrinkles appear randomly across the sheets, and one or more wrinkles are typically observed when the scanning area is larger than ~2 μm^2. Previous STM studies have indicated that wrinkles of similar physical dimensions appear at a similar density on freshly cleaved graphite surfaces obtained through mechanical exfoliation using adhesive tapes.[41] Because a similar exfoliation technique is employed in the fabrication of graphene sheets,[3, 33] it may be that wrinkles are unavoidable for graphene on SiO_2. Recent theoretical studies have also proposed the spontaneous formation of wrinkles for graphene on SiO_2 substrates.[42] We, however, do not dismiss the possibility that the standard microfabrication procedures employed in this study might result in additional wrinkles in the graphene sheet.

Surprisingly, atomically resolved topographs (Figure 4.5C, D) reveal very different structures for the wrinkles in comparison with other parts of graphene. A triangular pattern is observed over the entire graphene wrinkle (Figure 4.5C, D), and the distance between adjacent bright spots is ~2.5 Å, indicating the honeycomb six-fold symmetry of the graphene lattice is broken, and only three of the six carbon atoms in each hexagonal ring is observed (Figure 4.5D). In comparison, the topograph taken on the same graphene sheet adjacent to the wrinkle (Figure 4.5E) reveals the honeycomb structure that is consistently observed on the "flat" (by "flat" we mean only the ~4 Å ripples are present) parts of the monolayer graphene sheets investigated in our study. The "three-for-six" triangular patterns were observed on all (~10) the wrinkles we investigated over a couple of different graphene samples. For example, Figure 4.6 shows the triangular patterns observed on another wrinkle in another graphene sheet.

Most previous STM studies on monolayer graphene sheets on SiO_2 substrates reported honeycomb patterns.[18-21] Small (<1 nm) and random regions of "three-for-six" triangular patterns mixed with honeycomb patterns have been observed in one individual sample.[17] The origin of such patterns was unclear, but was conjectured to be due to the presence of “strong spatially dependent perturbations”, including local curvature or trapped charges.[17, 43] In our study, honeycomb patterns are observed for all “flat” parts of graphene (with ~4 Å high ripples), while triangular patterns are exclusively and consistently observed on the ~3 nm high wrinkles. These results indicate that increased local curvature (and the associated strain) on the wrinkles can provide strong enough perturbations to break the six-fold symmetry and degeneracy of the electronic states in graphene.

Because STM topographs represent the local density of states (DOS) distribution, we were able to further investigate how the “three-for-six” pattern characteristic of the wrinkles reflected the local electronic states and geometric structure of graphene.[44] This can be probed by measuring topographs at both positive and negative sample biases,[44] since such STM measurements will respectively probe the LUMO (empty states) and HOMO (filled states) of the sample.

Figure 4.6A, B gives the atomically resolved STM topographs of the top surface of a graphene wrinkle, obtained at positive and negative sample biases. The same “three-for-six” triangular patterns are observed for positive and negative biases (Figure 4.6C): the center parts of the two topographs, which correspond to the crest of the wrinkle, overlap with each other exactly, and a regular triangular lattice is observed. Small distortions of the triangular lattice are observed for regions away from the center, and the patterns obtained from the two scans gradually mismatch with each other. This suggests that the wrinkle is flexible, and the force from the STM tip causes a slight deformation of the wrinkle during scans. In comparison, on the “flat” part of the same graphene sheet (Figure 4.6D-F), although ~4 Å ripples are present, clear honeycomb structures were observed for both positive and negative biases, and the obtained topographs always exactly overlap, suggesting the ripples are more rigid compared to the wrinkle.

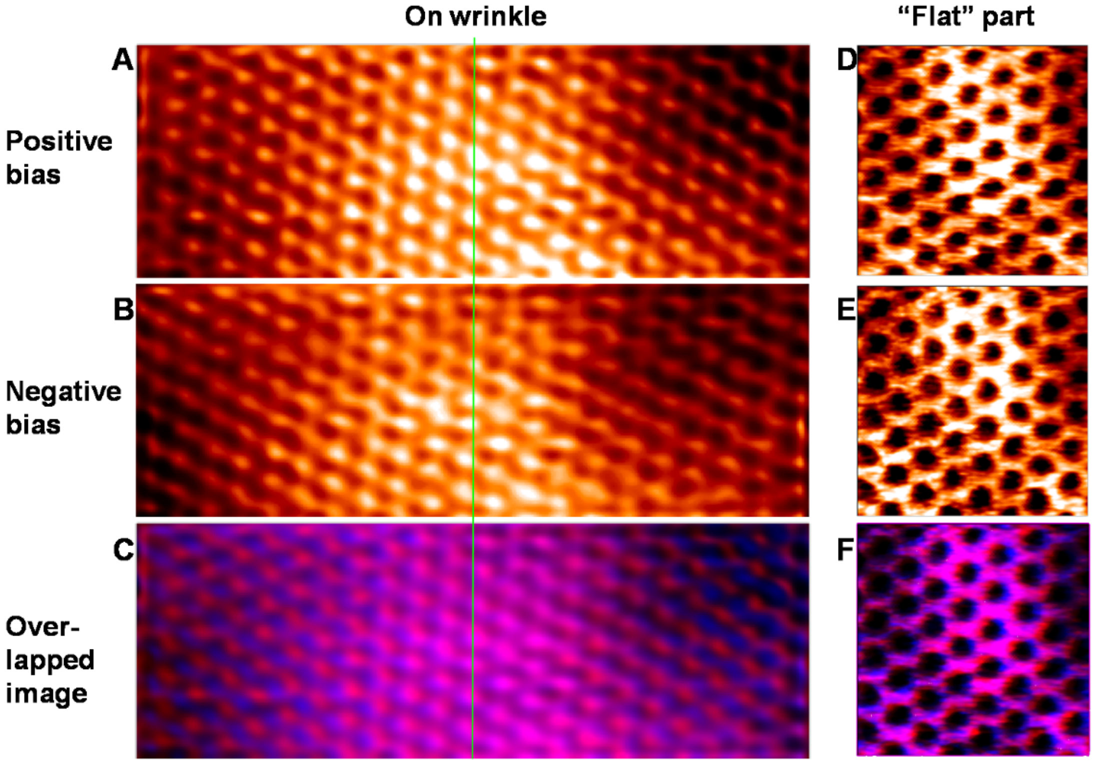

Figure 4.6. Comparison of STM topographs of a graphene wrinkle and a "flat" part of the same graphene sheet, obtained at positive and negative sample biases. (A): STM topograph (4.60 nm × 1.66 nm) of the top of a graphene wrinkle obtained at positive sample bias (V_b = 0.5 V, I = 210 pA). **(B):** STM topograph of the same region obtained at negative sample bias (V_b = -0.5 V, I = -210 pA). **(C):** An overlapped image, in which the topographs obtained at positive bias and negative bias are presented in red and blue, respectively. Overlapped regions thus become purple. The green line marks the center of the topograph, which is also the crest of the wrinkle. **(D):** STM topograph (1.5 nm × 1.5 nm) of a "flat" part of the same graphene sheet, obtained at positive sample bias (V_b = 0.5 V, I = 150 pA). **(E):** STM topograph of the same region obtained at negative sample bias (V_b = -0.5 V, I = -150 pA). **(F):** An overlapped image.

The same "three-for-six" patterns obtained on the wrinkle at positive and negative sample biases suggest the patterns reflect the actual topology of atoms in graphene. Recent experiments on hydrogenation of graphene have suggested that local bending/curvature in graphene may induce some sp^3 hybridization component in the otherwise sp^2-hybridized carbons, which facilitates the breaking of delocalized π-bonds in graphene.[45, 46] With a tendency towards sp^3 hybridization, the six carbon atoms in each hexagon ring of graphene may start to adopt a structure similar to the chair conformation of cyclohexane, and so three of the six atoms protrude up and out of the hexagon ring, leading to the "three-for-six" pattern seen in our STM topographs.

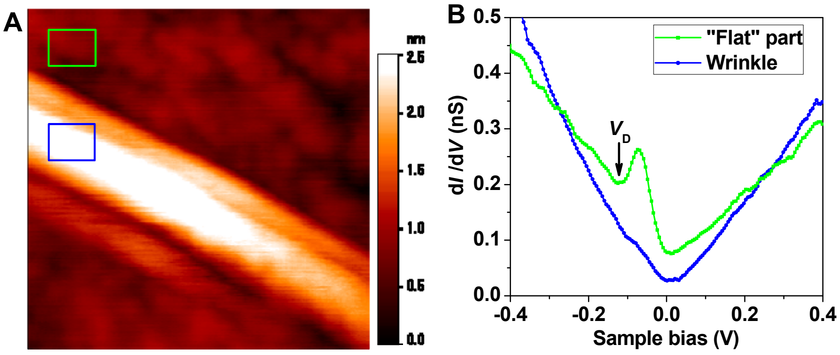

Figure 4.7. Scanning tunneling spectroscopy study of a graphene wrinkle. (A): Constant-current STM topograph (50 nm × 50 nm) of the wrinkle (V = 0.5 V, I = 0.1 nA). The largest height is ~3 nm. **(B):** Differential conductance of the wrinkle [averaged over the blue rectangle in (A)], in comparison with that of a "flat" part [averaged over the green rectangle in (A)] of graphene, where ripples ~4 Å in height are observed.

We have also characterized the electrical properties of graphene wrinkles through spatially resolved STS. Theoretical studies have suggested that corrugations and the associated strain in graphene may alter the local electrical properties of graphene.[5, 14, 15]

On the other hand, recent STS studies on graphene have found very limited or no correlations between corrugations and local electrical properties.[21-23] This is presumably because the previously studied ripples on "flat" parts of graphene were too small (~4 Å in height).

We have found distinctly different electrical properties for the ~3 nm high wrinkles. Figure 4.7B presents the differential conductance behavior of a wrinkle, in comparison with other parts of the graphene sheet, where small ripples are present. Lower conductance is observed for the wrinkle at low bias voltages, indicating the wrinkle is less conductive than other parts of graphene. This is in agreement with our previous discussions that the local bending/curvature effects may weaken delocalized π-bonds. For the "flat" part of graphene, in addition to a soft gap at zero bias, a clear dip (local minimum) of differential conductance is observed at V_D = -0.12 V (Figure 4.7B). This corresponds to the charge-neutral Dirac point of graphene,[19] at which energy the conduction and valance bands of graphene meet at a single point in *k*-space, and so charge carriers vanish. Interestingly, this dip disappears on the wrinkle (Fig 4.7B). This may be explained with recent theoretical studies, which suggest large local corrugations may lead to midgap states, and so a finite density of state is present at the neutrality point.[14, 46, 47]

We have utilized cryo-STM to investigate a new class of corrugations in monolayer graphene sheets, i.e., wrinkles ~10 nm in width and ~3 nm in height. We found such corrugations to be ubiquitous in graphene and have distinctly different properties in comparison to "flat" regions of graphene that only contain small ripples. The observed wrinkles are likely important for understanding the electrical and mechanical properties of graphene. Recently developed graphene manipulation methods[48, 49] may permit the controlled formation of wrinkles, which would be a first step toward harnessing wrinkles to control the electronic landscape of graphene sheets.

4.4 Electron transport in graphene nanoribbons

Figure 4.8 summarizes the conductance measurements as a function of gate voltage for three representative GNR devices of varying numbers of graphene layers (1, 2 and ~20) but the same uniform width (W = 15±1 nm). In our experiments, a heavily doped silicon substrate beneath the 300 nm SiO_2 surface layer was employed as the back gate. The measurements were performed at different temperatures as indicated. All curves exhibit a region of depressed conductance with respect to the gate voltage. As mentioned above, the carrier density in graphene vanishes at the Dirac point, where the conductance and valence bands meet. It is then expected in a low carrier density system that a dip in conductance would occur while tuning the carrier density by gating.[27] In an ideal, undoped device, this should occur at zero gate voltages. In our experiments, however, we often observe different minimal-conductance positions for different devices. Even for the same device, temperature cycling also often induces shifting of the minimal-conductance points and thus hysteresis. These shifts of the observed minimal-conductance points are due to the charges trapped in the underlying SiO_2 and possible adsorbates on top of graphene, which act as an electrostatic gate and modify the carrier types and densities accordingly.[23] For most of our devices, the minimal-conductance point occurs at positive gate voltages, indicating that they are p-type.

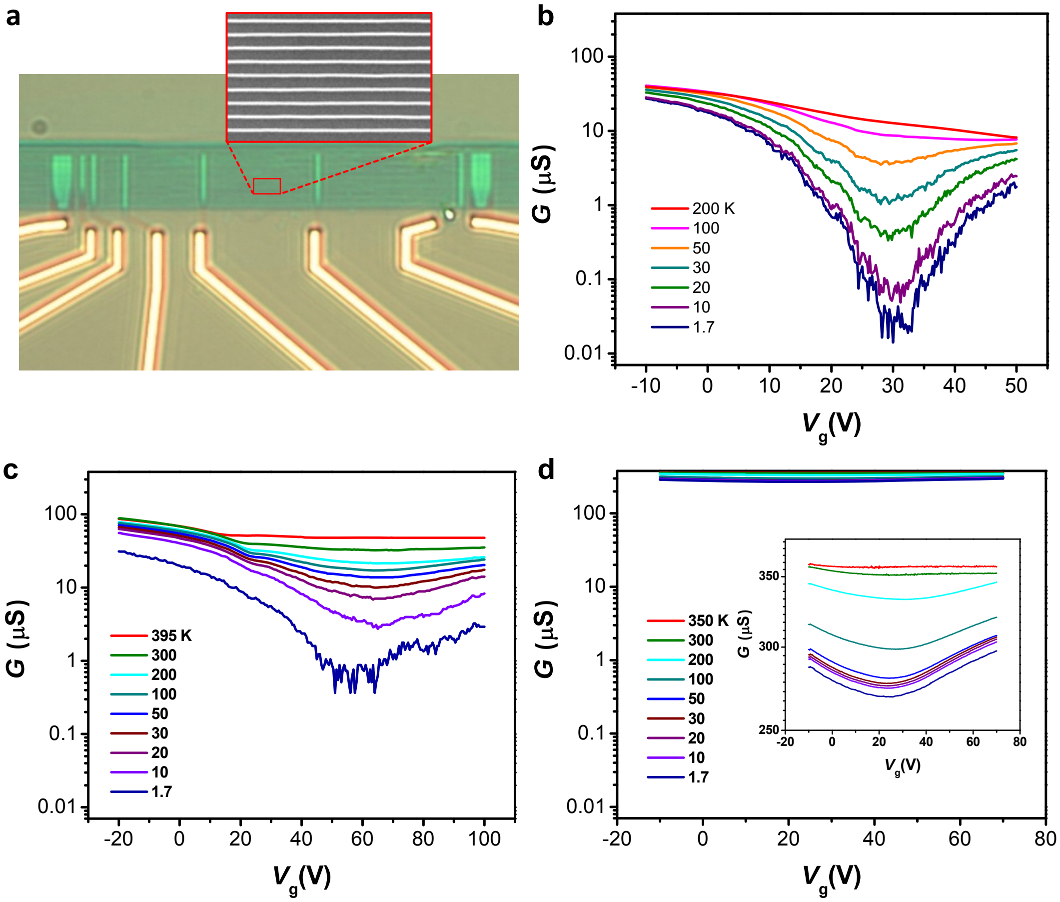

Figure 4.8. Conductance measurements of graphene nanoribbons (GNRs). (a) An optical image of a typical single-layer graphene FET device used in the transport measurements. The heavily doped silicon substrate beneath the 300 nm SiO_2 surface layer was used as the gate. Inset is an SEM micrograph of the GNRs (covered with SiO_2 and Pt wires). The width of the nanoribbon is measured to be 15±1 nm; (b-d) Gate-voltage dependent conductance of single- (b), double- (c), and ~20-layer (d) GNRs measured at different temperatures; The numbers of parallel nanoribbons for (b-d) are 78, 65 and 45, respectively. The lengths of wires for (b-d) are 3, 12 and 2 μm, respectively. Note that the conductance scales are the same for the three sets of devices. Inset in (d) is an expanded view of the same plot.

Our observations of a depressed region of conductance in GNRs are qualitatively in agreement with that in graphene films.[25] In "bulk" graphene, this dip corresponds to the minimum conductivity ~$4e^2/h$, where e and h are electron charge and Planck constant, respectively. At higher temperatures (>200K), a similar behavior is observed in our GNR devices. For instance, at room temperature the single-layer GNR device gives a conductance dip (data not shown here) on the order of $4e^2/h(nW/L)$, where n and L are the number and length of parallel GNRs, respectively.

Remarkably, at low temperatures the minimum conductance decreases by more than an order of magnitude for both single- and double-layer GNRs, whereas the multi-layer device exhibits small decreases (Figure 4.8b-d). These results, i.e., conductance decreases with decreasing temperature regardless of the number of layers, indicate thermally activated behavior. This observed behavior is in general agreement with previous studies on *individual* GNRs, and suggests the opening up of band gaps in GNRs. In contrast, the conductance of bulk graphene films generally increases with decreasing temperature. However, it is noteworthy that in our study, the conductance gaps smoothly and consistently increase as temperature decreases for all GNR devices. This is in contrast to the large, ill-defined variations typically observed in previous studies on individual graphene nanoribbons.[27, 29] This is likely because we are measuring parallel GNRs, and so such sample-dependent variations are averaged out. Meanwhile, the more meaningful general trend becomes much clearer.

As the number of graphene layers increases, the temperature and gate-voltage dependence of conductance both weakens, suggesting smaller energy gaps in thicker GNRs. For the ~20 layer GNRs in our study, the gap practically vanishes. This clear observation that the band gap (and so the on-off ratio) decreases as the number of layers increases highlights the precisely controlled GNR width afforded by our SNAP technique. In contrast, previous experiments have not been able to tell the property differences between GNRs made of different numbers of layers, due to the difficulties in obtaining GNRs of well-defined widths.

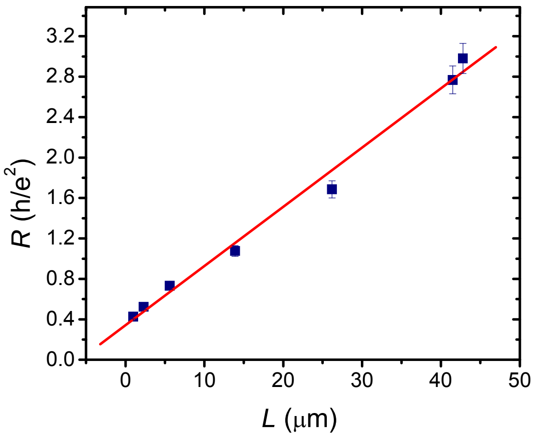

Figure 4.9. Linear dependence of GNR resistance on ribbon length. A plot of the resistance of single-layer graphene nanoribbons versus length, measured at room temperature with zero back-gate voltage. The number of ribbons in parallel is 78. Similar linear relationships were also observed for double- and multi-layer GNRs.

Figure 4.9 shows the total resistance of GNR arrays as a function of GNR length. A clear linear dependence is observed, which highlights the high quality of our GNRs with uniform properties. The small nonzero resistance at zero GNR length is likely due to the residue contact resistance which is independent of the ribbon length and can be subtracted from the curve. The hole mobility of our single-layer GNRs is estimated from the above back-gate FET measurements and plotted versus temperature in Figure 4.10a. The mobility slightly increases as the temperature drops from 200 K and peaks at about

25 K. The average value is slightly higher than previous studies (~200 cm^2/Vs),[29] likely due to smoother edges of the GNR.

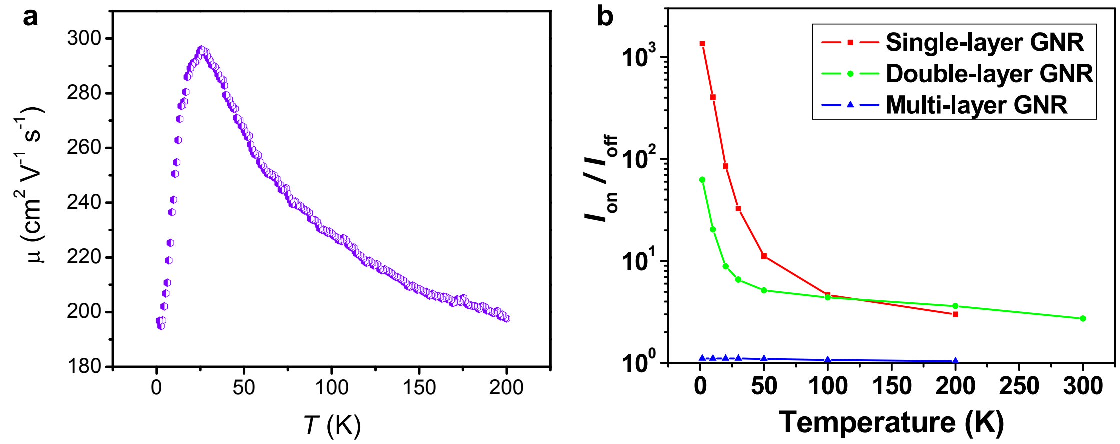

Figure 4.10. Mobility and current on/off ratio analysis. (a) Hole mobility versus temperature. The mobility data were extracted in the carrier density range: ~1.1-1.8 × 10^{12} cm^{-2}. (b) I_{on}/I_{off} versus temperature for various types of devices indicated.

Figure 4.10b summarizes our observation of the on-off current switching ratio (I_{on}/I_{off}) for our GNR FET devices. For both single- and double-layer GNR FET devices, we observed a dramatic increase in I_{on}/I_{off} as the temperature decreases. Over 3 orders of magnitude in I_{on}/I_{off} was observed for the single-layer FET at temperature <10 K. This further suggests our GNRs are semiconducting and a band gap is induced. The energy gap could be extracted according to the thermally activated behavior of the GNR devices. The on-off current switching is proportional to $\exp(E_g/k_BT)$, where E_g is the gap energy.[26] We obtained an E_g of ~6.5 and ~1.5 meV for single- and double-layer graphene GNR FET devices respectively. According to an empirical form of $E_g = \alpha/W$,[25] we obtained α~0.1 eV nm. In recent density functional theory studies,[50-52] the energy gap is predicted to be inversely proportional to the ribbon channel width, with a corresponding α value ranging from 0.2-1.5 eV nm, which is largely consistent with our observation.

4.5 Conclusion

In this chapter, we report on the scanning tunneling microscopy study of a new class of corrugations in exfoliated monolayer graphene sheets, i.e., wrinkles ~10 nm in width and ~3 nm in height. We found such corrugations to be ubiquitous in graphene, and have distinctly different properties when compared to other regions of graphene. In particular, a “three-for-six” triangular pattern of atoms is exclusively and consistently observed on wrinkles, suggesting the local curvature of the wrinkle provides a sufficient perturbation to break the six-fold symmetry of the graphene lattice. Through scanning tunneling spectroscopy, we further demonstrate that the wrinkles have lower electrical conductance and are characterized by the presence of midgap states, in agreement with recent theoretical predictions. The observed wrinkles are likely important for understanding the electrical properties of graphene.

We also studied the effect of width and number of graphene layers on the electronic transport in graphene nanoribbons (GNRs). As the lateral size decreases to nanometer range, conductance of *all* our GNR samples (regardless of number of layers) shows thermally activated behavior. Noticeable conductance gaps open up in both single- and double-layer GNR devices. The gaps smoothly and consistently increase as temperature decreases for all GNR devices. This contrasts with bulk graphene films, the conductance of which generally increases with decreasing temperature. Due to the precisely controlled GNR width afforded by SNAP, we have also for the first time clearly observed how the properties of GNRs evolve as a function of number of layers: the band gap (and so the on-off ratio) decreases as the number of layers increases.

4.6 References

1. Xu, K., Cao, P.G. & Heath, J.R. Scanning tunneling microscopy characterization of the electrical properties of wrinkles in exfoliated graphene monolayers. *Nano Lett.* **9**, 4446-4451 (2009).
2. Novoselov, K.S. et al. Electric field effect in atomically thin carbon films. *Science* **306**, 666-669 (2004).
3. Novoselov, K.S. et al. Two-dimensional atomic crystals. *Proc. Natl. Acad. Sci. U. S. A.* **102**, 10451-10453 (2005).
4. Geim, A.K. & Novoselov, K.S. The rise of graphene. *Nat. Mater.* **6**, 183-191 (2007).
5. Neto, A.H.C., Guinea, F., Peres, N.M.R., Novoselov, K.S. & Geim, A.K. The electronic properties of graphene. *Rev. Mod. Phys.* **81**, 109-162 (2009).
6. Geim, A.K. Graphene: status and prospects. *Science* **324**, 1530-1534 (2009).
7. Novoselov, K.S. et al. Room-temperature quantum hall effect in graphene. *Science* **315**, 1379-1379 (2007).
8. Mermin, N.D. Crystalline order in two dimensions. *Physical Review* **176**, 250-254 (1968).
9. Meyer, J.C. et al. The structure of suspended graphene sheets. *Nature* **446**, 60-63 (2007).
10. Meyer, J.C. et al. On the roughness of single- and bi-layer graphene membranes. *Solid State Commun.* **143**, 101-109 (2007).
11. Fasolino, A., Los, J.H. & Katsnelson, M.I. Intrinsic ripples in graphene. *Nat. Mater.* **6**, 858-861 (2007).
12. Morozov, S.V. et al. Strong suppression of weak localization in graphene. *Phys Rev Lett* **97**, 016801 (2006).
13. Morozov, S.V. et al. Giant intrinsic carrier mobilities in graphene and its bilayer. *Phys Rev Lett* **100**, 016602 (2008).
14. Guinea, F., Katsnelson, M.I. & Vozmediano, M.A.H. Midgap states and charge inhomogeneities in corrugated graphene. *Phys Rev B* **77**, 075422 (2008).
15. Kim, E.A. & Neto, A.H.C. Graphene as an electronic membrane. *Epl* **84**, 57007 (2008).
16. Herbut, I.F., Juricic, V. & Vafek, O. Coulomb interaction, ripples, and the minimal conductivity of graphene. *Phys Rev Lett* **100**, 046403 (2008).

17. Ishigami, M., Chen, J.H., Cullen, W.G., Fuhrer, M.S. & Williams, E.D. Atomic structure of graphene on SiO_2. *Nano Lett.* **7**, 1643-1648 (2007).
18. Stolyarova, E. et al. High-resolution scanning tunneling microscopy imaging of mesoscopic graphene sheets on an insulating surface. *Proc. Natl. Acad. Sci. U. S. A.* **104**, 9209-9212 (2007).
19. Zhang, Y.B. et al. Giant phonon-induced conductance in scanning tunnelling spectroscopy of gate-tunable graphene. *Nat. Phys.* **4**, 627-630 (2008).
20. Geringer, V. et al. Intrinsic and extrinsic corrugation of monolayer graphene deposited on SiO_2. *Phys Rev Lett* **102**, 076102 (2009).
21. Deshpande, A., Bao, W., Miao, F., Lau, C.N. & LeRoy, B.J. Spatially resolved spectroscopy of monolayer graphene on SiO_2. *Phys Rev B* **79**, 205411 (2009).
22. Teague, M.L. et al. Evidence for strain-induced local conductance modulations in single-layer graphene on SiO_2. *Nano Lett.* **9**, 2542-2546 (2009).
23. Zhang, Y., Brar, V.W., Girit, C., Zettl, A. & Crommie, M.F. Origin of spatial charge inhomogeneity in graphene. *Nat. Phys.* **5**, 722-726 (2009).
24. Han, M.Y., Brant, J.C. & Kim, P. Electron transport in disordered graphene nanoribbons. *Phys Rev Lett* **104**, 056801 (2010).
25. Han, M.Y., Ozyilmaz, B., Zhang, Y.B. & Kim, P. Energy band-gap engineering of graphene nanoribbons. *Phys Rev Lett* **98**, 206805 (2007).
26. Li, X.L., Wang, X.R., Zhang, L., Lee, S.W. & Dai, H.J. Chemically derived, ultrasmooth graphene nanoribbon semiconductors. *Science* **319**, 1229-1232 (2008).
27. Chen, Z.H., Lin, Y.M., Rooks, M.J. & Avouris, P. Graphene nano-ribbon electronics. *Physica E* **40**, 228-232 (2007).
28. Jiao, L.Y., Zhang, L., Wang, X.R., Diankov, G. & Dai, H.J. Narrow graphene nanoribbons from carbon nanotubes. *Nature* **458**, 877-880 (2009).
29. Wang, X.R. et al. Room-temperature all-semiconducting sub-10-nm graphene nanoribbon field-effect transistors. *Phys Rev Lett* **100**, 206803 (2008).
30. Bai, J.W., Duan, X.F. & Huang, Y. Rational fabrication of graphene nanoribbons using a nanowire etch mask. *Nano Lett.* **9**, 2083-2087 (2009).
31. Sols, F., Guinea, F. & Neto, A.H.C. Coulomb blockade in graphene nanoribbons. *Phys Rev Lett* **99**, 166803 (2007).
32. Martin, I. & Blanter, Y.M. Transport in disordered graphene nanoribbons. *Phys Rev B* **79**, 235132 (2009).

33. Zhang, Y.B., Tan, Y.W., Stormer, H.L. & Kim, P. Experimental observation of the quantum Hall effect and Berry's phase in graphene. *Nature* **438**, 201-204 (2005).
34. Ferrari, A.C. et al. Raman spectrum of graphene and graphene layers. *Phys Rev Lett* **97**, 187401 (2006).
35. Graf, D. et al. Spatially resolved Raman spectroscopy of single- and few-layer graphene. *Nano Lett.* **7**, 238-242 (2007).
36. Melosh, N.A. et al. Ultrahigh-density nanowire lattices and circuits. *Science* **300**, 112-115 (2003).
37. Rutter, G.M. et al. Scattering and interference in epitaxial graphene. *Science* **317**, 219-222 (2007).
38. Cerda, E. & Mahadevan, L. Geometry and physics of wrinkling. *Phys Rev Lett* **90**, 074302 (2003).
39. Biedermann, L.B., Bolen, M.L., Capano, M.A., Zemlyanov, D. & Reifenberger, R.G. Insights into few-layer epitaxial graphene growth on 4H-SiC(0001) substrates from STM studies. *Phys Rev B* **79**, 125411 (2009).
40. Li, X.S. et al. Large-area synthesis of high-quality and uniform graphene films on copper foils. *Science* **324**, 1312-1314 (2009).
41. Chang, H.P. & Bard, A.J. Observation and characterization by scanning tunneling microscopy of structures generated by cleaving highly oriented pyrolytic-graphite. *Langmuir* **7**, 1143-1153 (1991).
42. Guinea, F., Horovitz, B. & Le Doussal, P. Gauge fields, ripples and wrinkles in graphene layers. *Solid State Commun.* **149**, 1140-1143 (2009).
43. Stolyarova, E. et al. Scanning tunneling microscope studies of ultrathin graphitic (graphene) films on an insulating substrate under ambient conditions. *J Phys Chem C* **112**, 6681-6688 (2008).
44. Kane, C.L. & Mele, E.J. Broken symmetries in scanning tunneling images of carbon nanotubes. *Phys Rev B* **59**, R12759-R12762 (1999).
45. Ryu, S. et al. Reversible basal plane hydrogenation of graphene. *Nano Lett.* **8**, 4597-4602 (2008).
46. Elias, D.C. et al. Control of graphene's properties by reversible hydrogenation: evidence for graphane. *Science* **323**, 610-613 (2009).
47. Wehling, T.O., Balatsky, A.V., Tsvelik, A.M., Katsnelson, M.I. & Lichtenstein, A.I. Midgap states in corrugated graphene: Ab initio calculations and effective field theory. *Epl* **84**, 17003 (2008).

48. Bao, W. et al. Controlled ripple texturing of suspended graphene and ultrathin graphite membranes. *Nature Nanotechnology* **4**, 562-566 (2009).

49. Li, Z., Cheng, Z., Wang, R., Li, Q. & Fang, Y. Spontaneous formation of nanostructures in graphene. *Nano Lett.* **9**, 3599-3602 (2009).

50. Son, Y.W., Cohen, M.L. & Louie, S.G. Energy gaps in graphene nanoribbons. *Phys Rev Lett* **97**, 216803 (2006).

51. Son, Y.W., Cohen, M.L. & Louie, S.G. Half-metallic graphene nanoribbons. *Nature* **444**, 347-349 (2006).

52. Barone, V., Hod, O. & Scuseria, G.E. Electronic structure and stability of semiconducting graphene nanoribbons. *Nano Lett.* **6**, 2748-2754 (2006).

Chapter 5

Imaging through Graphene Templating

The contents presented in this chapter are based on Xu, K., Cao, P.G. and Heath, J.R. "Graphene visualizes the first water adlayers on mica at ambient conditions," *Science*, 329, 1188-1191 (2010) (Ref.[1]) and Cao, P.G., Xu, K., Varghese, J.O. and Heath, J.R. "Atomic force microscopy characterization of room-temperature adlayers of small organic molecules through graphene templating," *J Am Chem Soc*, 133, 2334-2337 (2011). (Ref.[2])

5.1 Introduction

In the previous chapter, we have described the electrical properties of graphene wrinkles and nanoribbons. Here we explore the application of graphene for imaging surface adlayers (for example, water) at ambient conditions. Under usual operating conditions, imaging of these dynamic adlayers through scanning probe microscopy is often prohibitively challenging because of the significant intervening force exerted by the probe tip. In our newly developed technique, graphene is used as an ultrathin (one atom thick) coating layer to fix the otherwise fragile surface adlayers, which enables characterization through atomic force microscopy (AFM) at room temperature.

5.1.1 Water

Water coats all hydrophilic surfaces under ambient conditions, and the first water adlayers on a solid often dominate the surface behavior.[3-6] Although scanning tunneling microscopy (STM) and other ultrahigh vacuum surface characterization techniques have been extensively employed to study water (ice) adlayers on solids at cryogenic temperatures,[3, 4] such techniques are not applicable to room-temperature studies because of the high vapor pressure of water.[4, 5] Various optical methods have been used at ambient conditions to probe the averaged properties of water adlayers over macroscopic areas.[5, 7-9] Atomically resolved studies have remained challenging. For example, although thin ice layers have been studied with atomic force microscopy (AFM) below freezing temperatures,[10, 11] reliable AFM imaging of water adlayers under ambient conditions is confounded by tip-sample interactions.[4] For example, the capillary menisci formed between the tip and the sample strongly perturb the water adlayers on solids.[12]

Scanning polarization force microscopy (SPFM) has been utilized to image water adlayers.[4, 13, 14] For SPFM, the tip-sample distance is kept at tens of nanometers. By briefly contacting the tip on a mica surface to induce capillary condensation, metastable island-like structures were observed in SPFM images. These islands were interpreted as a second adlayer on a monolayer of water.[4, 14] However, the lateral resolution of SPFM is relatively low, and the measured apparent heights reflect local polarizability instead of actual heights. Furthermore, the structure of the *first* adlayer was not observed, likely because of the low lateral resolution and/or the dynamic nature of the first adlayer.[14]

In this chapter, we report on the use of monolayer graphene sheets as ultrathin coatings for enabling an AFM study of the first water adlayers on mica. Sputtered carbon is commonly used to coat biological systems, such as cells, for electron microscopy imaging. The carbon enables the imaging experiments by providing a protective (and conductive) coating. The graphene coating used here plays a somewhat similar role; graphene can tightly seal what are otherwise elusive adlayers, and stably “fix” the water adlayer structures, thus permitting the detection of the structure of the first water adlayers under ambient conditions. Humidity-dependent experiments further reveal how the structure of the water adlayers evolves at the nanometer and molecular scale.

5.1.2 Organic molecules

The first layers of organic molecules adsorbed to solid surfaces often determine the physics and chemistry of both the adsorbate and the substrate, and thus play a crucial role in many applications, including, for example, heterogeneous catalysis, corrosion, adhesion, lubrication and environmental control.[15-17] For instance, the adsorption of volatile organic molecules on ambient surfaces plays an important role in determining the environmental fate of airborne organic pollutants.[16]

However, most of our current knowledge of adsorption processes has been gained from macroscopic measurements on large areas of surfaces, which provide limited information on the microscopic structures of adlayers. In particular, the structures of adlayers at the interfaces between solids and *vapors* of small organic molecules are poorly understood at ambient temperatures. The reasons are two-fold. First, organic compounds capable of forming vapors at room temperatures are inevitably volatile, and so molecularly thin adlayers on surfaces quickly evaporate away in the vacuum environments required by many surface characterization techniques. Second, when vacuum is not required, the microscopic structure of the adlayers is still difficult to probe due to the mobile nature of small molecules on surfaces, although certain area- and time-averaged properties can be determined (e.g., the averaged thickness of adlayers[18]).

As a result of these difficulties, previous experimental work on the room-temperature structures of weakly bound organic molecule adlayers (or molecularly thin films) on solids has largely been limited to nonvolatile molecules (boiling point >>~250 °C) with high molecular weight (number of carbon atoms >>10).[19-25] Such adlayers (thin films) are typically obtained through coating from a solution phase, and so are fundamentally different from adlayers in equilibrium with a vapor. Alternatively, adlayers of small organic molecules have been studied at low temperatures (T<<200 K), where the vapor pressure and mobility of molecules are drastically reduced.[15, 17, 26, 27] However, the adlayer structures are found to be highly temperature-dependent,[17, 26] and thus the low-T results cannot be directly compared with the room-temperature vapor adsorption one encounters in everyday life.

In the remainder of this chapter, we report on the use of graphene sheets as an ultrathin coating/template for AFM characterization of the room-temperature structures of the adlayers at the interfaces between mica surfaces and vapors of small organic molecules. We show that graphene, albeit only one-atom thick, can prevent the evaporation of molecularly thin adlayers of volatile small organic molecules, and slows down, but doesn't fully prevent, the motions of the adsorbed molecules on the solid surface, thus allowing AFM observation of both the *structure* and *dynamics* of the adlayers at room temperature. Two common small organic molecules, tetrahydrofuran (THF) and cyclohexane, each representing one of the two classes of polar and non-polar organic solvents, were investigated and compared with water.

5.2 Experimental

5.2.1 Materials

Anhydrous inhibitor-free tetrahydrofuran (THF, ≥99.9%, water content <0.002%) and anhydrous cyclohexane (99.5%, water content <0.001%) were purchased from

Sigma-Aldrich. These reagents were used as supplied and stored in a glove-box purged with nitrogen. Muscovite mica (Grade V1; round disks of diameter 10 mm) was obtained from Ted Pella. Kish graphite was obtained from Covalent Materials US Inc.

5.2.2 Sample preparation

Single and few-layer graphene sheets were prepared by the standard method of mechanical exfoliation[28, 29] of Kish graphite on freshly cleaved muscovite mica. All experiments were performed at room temperature (22±2 °C). Humidity was monitored using a Fluke 971 temperature humidity meter. For graphene deposited on mica at ambient conditions, the ambient relative humidity (RH) was measured to be in a range of 36% to 42%. The low-humidity experiment was carried out in a glove-bag (Sigma-Aldrich AtmosBag) that was purged and protected under a continuous flow of ultrahigh purity argon. Mica disks were first heated in air at 200 °C for 10 min to remove any absorbed moisture, and then transferred into the glove-bag. The mica surface was cleaved in the glove-bag and allowed to equilibrate for ~5 min before graphene was deposited. A reading of RH = 1.8% to 2.1% was recorded for the process. The high-humidity experiment was carried out in a chamber with a beaker of water at the center. The mica surface was cleaved in the chamber and allowed to equilibrate for ~5 min before graphene was deposited. A reading of RH = 89±2% was recorded during the process.

For adsorption of organic molecules on mica, the mica was heated as mentioned above and transferred to the glove-bag in a low-humidity environment(<2%). The mica surface was cleaved in the glove-bag and exposed to organic vapors for ~10 s to ~1 min. The partial pressure of organic molecules at the mica surface, which determines the surface coverage at equilibrium, was adjusted by varying the distance between the vapor source and the mica surface.

5.2.3 Identification of graphene layers

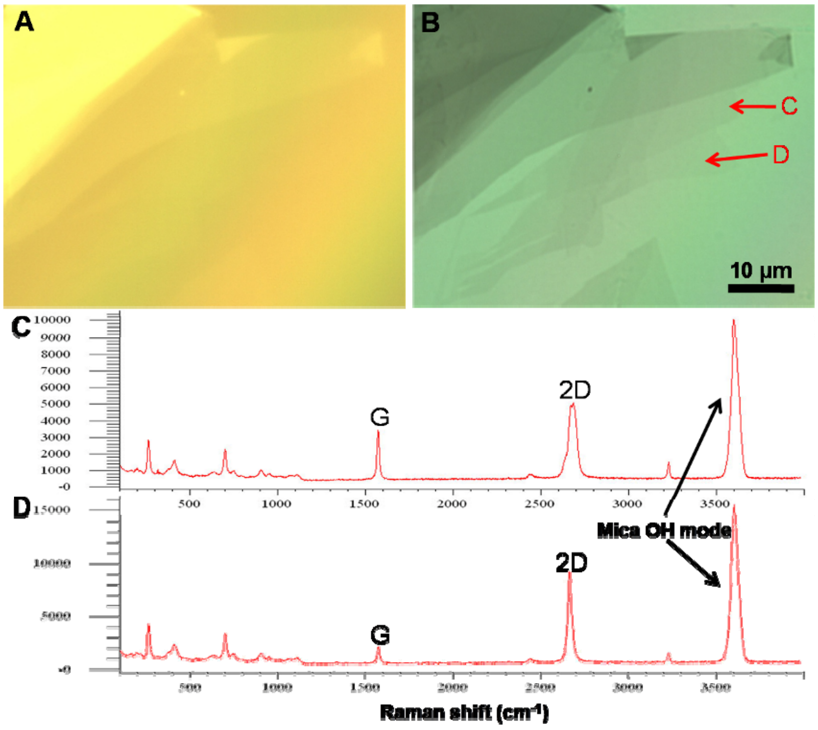

Figure 5.1. Few-layer graphene sheets are most readily observed through transmission optical microscopy. (**A**) In reflective optical microscopy, the thinnest graphene sheets are hard to see. (**B**) Transmission optical microscopy of the same area reveals the thinnest graphene sheets. (**C** and **D**) Raman spectra of two different regions of the graphene sheets as indicated in (B), corresponding to bilayer and monolayer graphene, respectively.

Graphene mono- and few-layers were identified through optical microscopy and confirmed by spatially resolved Raman spectroscopy. In the optical search process, we found it was easier to identify the thinnest graphene sheets using transmitted light (the mica substrate is translucent and the graphene layers absorb white light[30]). Figure 5.1 A, B compares the optical images taken at reflection and transmission modes, respectively. The edges of the thinnest graphene layers are clearly resolved in the latter mode.

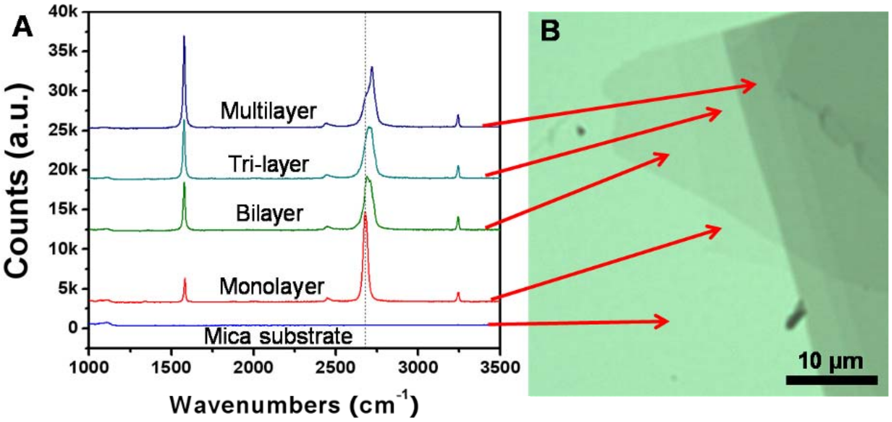

Figure 5.2. Identification of numbers of graphene layers in a representative sample. Spatially resolved Raman spectra of different regions in (**B**) are given in (**A**). Sample was made at ambient conditions.

Raman spectra were recorded with a Renishaw M1000 Micro Raman spectrometer system using a 514.5 nm laser beam and a 2400 lines per mm grating. A confocal optical microscope with a ×100 objective lens was used to record spectra with a spatial resolution of 2 μm. The numbers of grapheme layers were unambiguously confirmed through spatially resolved Raman spectroscopy.[31, 32] As shown in Figures 5.1 and 5.2, no noticeable D peak was observed in the Raman spectra of the deposited graphene, which is suggestive of high-crystalline order of our samples. The sizes of the identified graphene mono- and few-layers range from tens of micrometers to more than 100 micrometers.

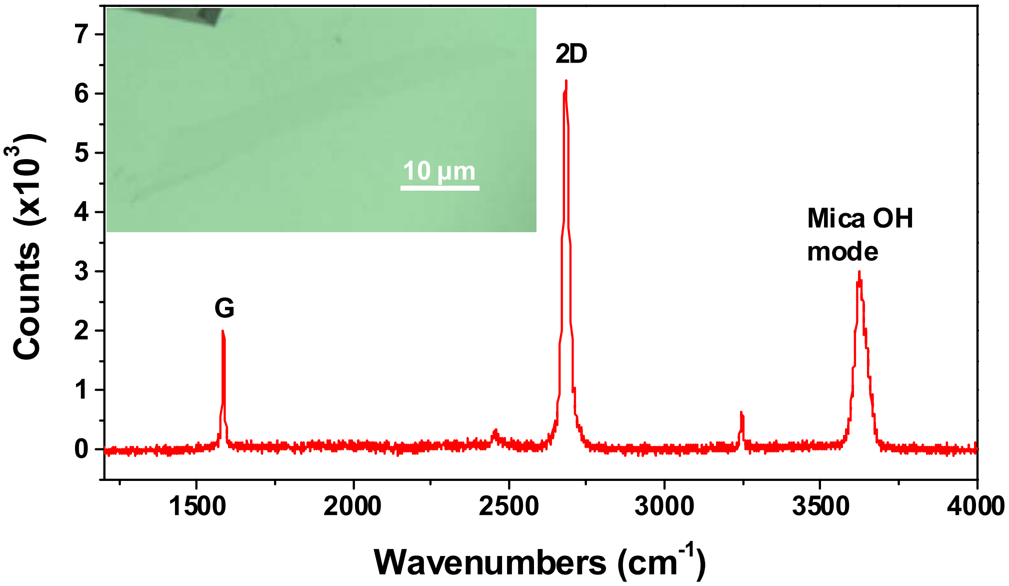

Figure 5.3. Raman spectrum of a monolayer graphene sheet deposited on a mica surface that was in equilibrium with a THF vapor. Inset: transmission optical image of the graphene sheet at the center. The 2D and G bands of graphene and the OH mode of mica are labeled. Similar Raman spectra were also observed for monolayer graphene sheets deposited on mica surfaces that were in equilibrium with cyclohexane vapors.

The layers of graphene for small organic molecules were identified in the same way as above and a typical spectrum for single-layer on THF adsorbed mica is presented in Figure 5.3.

5.2.4 Atomic force microscopy

All AFM images were acquired under tapping mode on a Digital Instrument Nanoscope IIIA at ambient conditions. A sharp TESP tip (Veeco) with a radius of end of 8 nm was used. Typical values for the force constant and resonance frequency were 42 N/m and 320 kHz, respectively. Height calibrations were performed using the step heights of freshly cleaved graphite samples. Due to the super-flatness of the samples, sometimes the laser interference pattern along the slow-scan axis was hard to avoid, which is more noticeable in large-area scanning and has a period of twice the wavelength of the laser. This is caused by the constructive interference of laser reflected from the sample surface and that reflected from the cantilever. The broad stripe-like features seen in Figure 5.12ab were due to this effect.

5.3 Water on mica

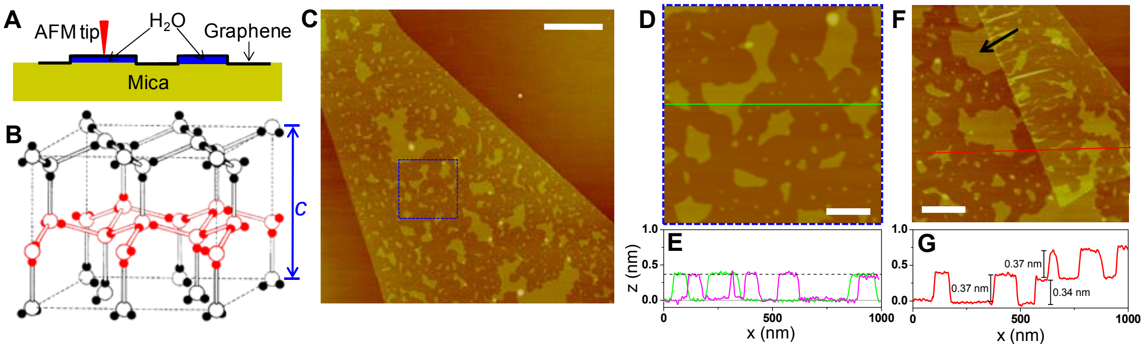

Figure 5.4. Graphene visualizes the first water adlayer on mica surface at ambient conditions. (**A**) A schematic of how graphene locks the first water adlayer on mica into fixed patterns, and severs as an ultrathin coating for AFM. (**B**) The structure of ordinary ice (ice I_h). Open balls represent O atoms, and smaller, solid balls represent H atoms. A single "puckered bilayer" is highlighted with red. Inter-layer distance is $c/2$ = 0.369 nm when close to 0 °C. Adapted from (Ref.[33]). (**C**) AFM image of a monolayer graphene sheet deposited on mica at ambient conditions. (**D**) A close-up of the blue square in (C). (**E**) Height profiles along the green line in (D) and from a different sample (Figure 5.6A). The dashed line indicates z = 0.37 nm. (**F**) AFM image of another sample, where the edge of a monolayer graphene sheet is folded underneath itself. Arrow points to an island with multiple 120° corners. (**G**) The height profile along the red line in (F), crossing the folded region. Scale bars: 1 μm for (C) and 200 nm for (D)(F). The same height scale (4 nm) is used for all images.

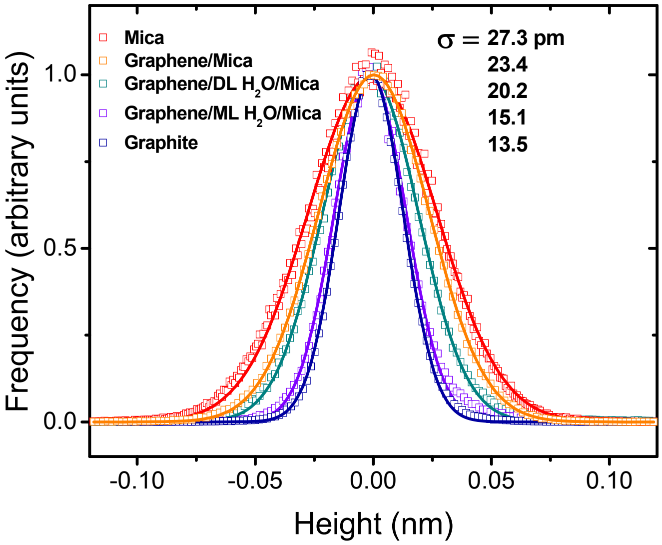

Figure 5.5. Comparison of the roughness of different surfaces. Height histograms (open squares) are given for a freshly cleaved mica surface, graphene on bare mica surface (from a sample prepared at 2% RH), graphene on a single water adlayer on mica (labeled as ML H_2O; from a sample prepared at 90% RH), graphene on top of two water adlayers (labeled as DL H_2O; from a sample prepared at 90% RH), and a freshly cleaved graphite surface. The statistics are obtained from scanning over 200 nm × 200 nm regions, similar to the conditions used in a previous study on graphene-on-mica [29]. The histograms are well fit by Gaussian distributions (solid lines). Standard deviations (σ) obtained from the Gaussian fits are listed in the figure. The measured surface roughness of mica and graphene on mica (27.3 and 23.4 pm) is similar to a previous study (34.3 and 24.1 pm).[29] On the other hand, the roughness of the graphite surface is measured to be considerably lower (13.5 pm vs. 22.6 pm), likely due to the differences in the specific settings of AFM. In general we find graphene on water adlayers has slightly lower surface roughness when compared to graphene on mica, which in turn is slightly smoother than the mica surface. These results suggest water molecules may be able to fill in surface defects on the atomic scale. However, as suggested in the previous study,[29] the measured roughness is likely limited by the noise of AFM.

In Figure 5.4 we present typical AFM images of graphene deposited on mica at ambient conditions [room temperature; relative humidity (RH) ~40%]. In agreement with a recent study,[29] we found graphene sheets spread atomically flat on mica over areas of 100-200 nm on a side (Figure 5.5). Over larger areas, however, island-like plateaus varying from a couple nanometers to a few micrometers in lateral size are observed across all the graphene samples (see also Figures 5.6, 5.8). These plateaus appear atomically flat (Figure 5.5), and plateaus from different samples have the same height of 0.37±0.02 nm (Figure 5.4, E and G), regardless of the lateral dimensions. Although dot-like thicker features are occasionally present, no plateaus with heights smaller than ~0.35 nm were observed.

The observed plateaus are not flakes of graphene or mica layers: such structures are not observed on the exfoliated surfaces of graphite and mica, or graphene deposited on SiO_2 substrates (Figure 5.6). In addition, the ~0.37 nm height is not consistent with the layer thicknesses of graphene (0.335 nm) or mica (0.99 nm), and, as described below, the structures themselves are dependent upon the relative humidity (RH) of the experimental conditions.

Figure 5.4FG presents data for the case in which the edge of a monolayer graphene sheet is folded underneath itself. A ~0.34 nm step height is observed for the folded graphene, while the same ~0.37 nm height is observed for plateaus both in and out of the folded region. Plateaus with the same height are also observed in bilayer graphene sheets, and the plateaus appear to be continuous across monolayer/bilayer borders (Figure 5.6). Our phase images further indicate that the plateau structures are under the graphene sheets (Figure 5.7). Plateau-like structures a few tenths of nms in height have been noticed for multi-layer graphene on mica, and were also identified as gases or moisture trapped under graphene.[34] Indeed, albeit only one-atom thick, monolayer graphene is known to be robust and impermeable to liquid and gas.[35, 36]

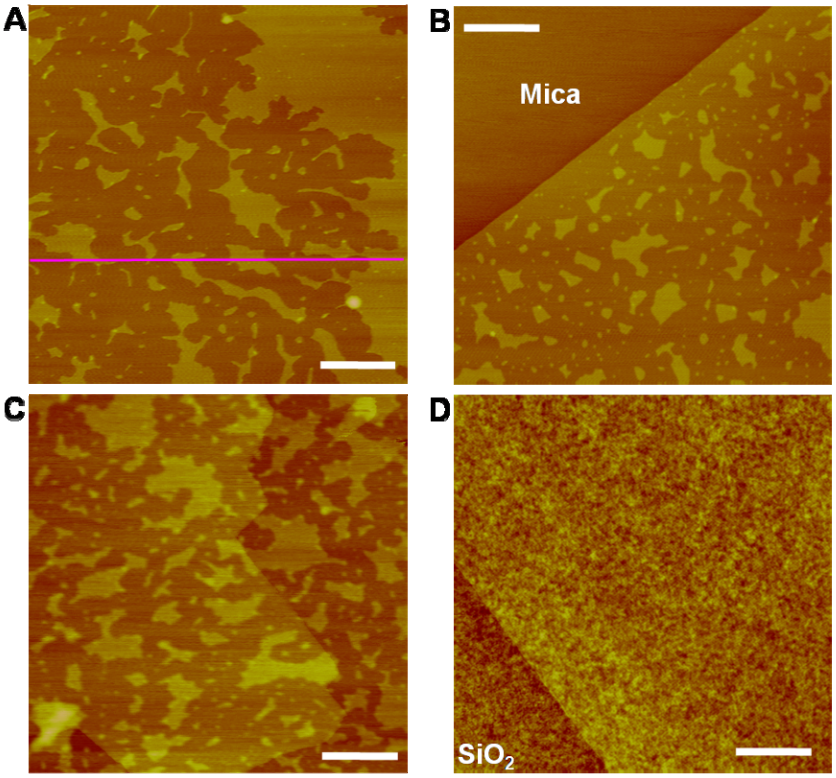

Figure 5.6. Additional AFM images of graphene deposited on mica and SiO_2 substrates under ambient conditions. (**A**, **B**) Additional images of monolayer graphene sheets deposited on mica. Pink line corresponds to the pink height profile in Figure 5.4E. (**C**) Image of another graphene-on-mica sample, at the border between bilayer (left) and monolayer (right) graphene sheets. (**D**) Image of a monolayer graphene sheet deposited on SiO_2 at ambient conditions. SiO_2 surfaces have very large surface roughness (standard deviations in height ~0.2 nm), and so adsorbed water molecules cannot form two-dimensional islands. Scale bars: 200 nm for (A) and (C). 500 nm for (B) and (D). The same height scale (4 nm) is used for all images.

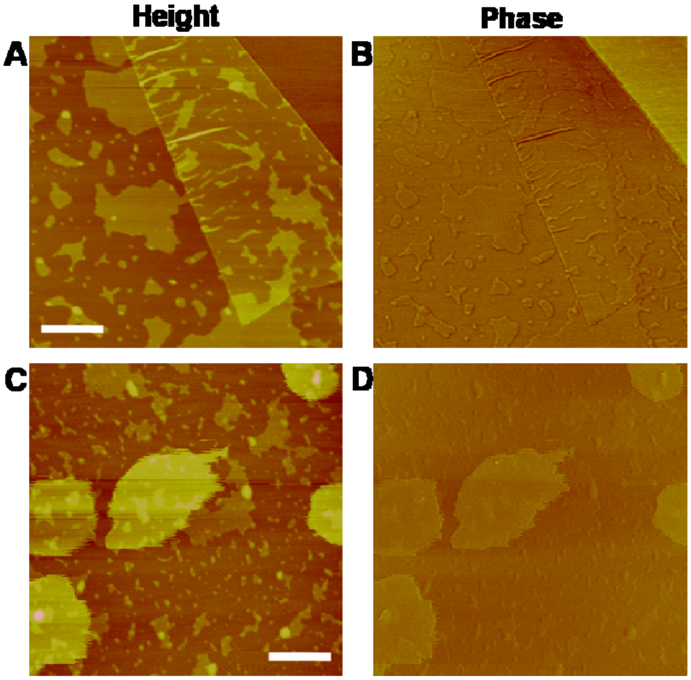

Figure 5.7. AFM phase images indicate the island-like plateau structures are under the graphene sheets. (**A**) Same as Figure 5.4F. The edge of the graphene sheet is folded underneath itself. (**B**) The corresponding phase image. Significant phase difference is observed between the mica (upper right corner) and graphene surfaces, reflecting the difference in surface properties.[37] In contrast, the same phase is observed for the plateaus and other parts of graphene (except for edges, which are always highlighted in phase images), indicating the AFM tip is interacting with the same surface (graphene), and the plateaus are underneath graphene. (**C**) AFM height image of a monolayer graphene sheet deposited on mica at ambient conditions, and then contaminated on the surface by the application of Scotch tape. (**D**) The corresponding phase image of (C). Contrasting phases are observed for the drop-like contaminants on the surface. On the other hand, the same phase is again observed for the plateaus and lower parts of graphene. In agreement with a recent study on friction force microscopy,[34] these results indicate the island-like plateau structures are under the graphene sheets. Scale bars: 200 nm. The same height scale (4 nm) is used for (A) and (C).

The observation of atomically flat plateaus that have well-defined heights and depend upon the RH indicates that the observed structures are not random gas molecules trapped between the graphene and mica surfaces, but instead are ordered water adlayers (Figure 5.4A). Previous SPFM studies have observed water layers on mica surfaces forming two-dimensional islands tens of nanometers to several microns in lateral size.[4, 13, 14] The shapes and size distribution of those water islands are in good agreement with the trapped structures in Figure 5.4, except that the presence of water islands smaller than a few tens of nanometers were not previously known, likely due to the ~10 nm lateral resolution of SPFM. The heights of the water islands were also not accurately determined with SPFM. The ~0.37 nm height we measured is in good agreement with the height of a monolayer of a "puckered bilayer" of ice ($c/2$ = 0.369 nm; Figure 5.4B),[33] a widely assumed model for how water molecules arrange in the first adlayer on a solid.[3, 6, 38]

We emphasize that although morphologically similar, the islands observed in the previous SPFM studies were the *second* water adlayer artificially induced on top of the first adlayer.[4, 14] The nature of the first adlayer was largely unknown due to the high mobility of water molecules at room temperature.[14] As will become more evident in the RH-dependent experiments (Figures 5.9 and 5.10), the plateaus we observed on samples prepared at ambient conditions (Figure 5.4) are the *first* water adlayer on the mica surface: the second adlayer only appears with high frequency at RH >~90%. For our case, graphene severs as an ultrathin coating and locks the first water adlayer into fixed patterns for AFM imaging.

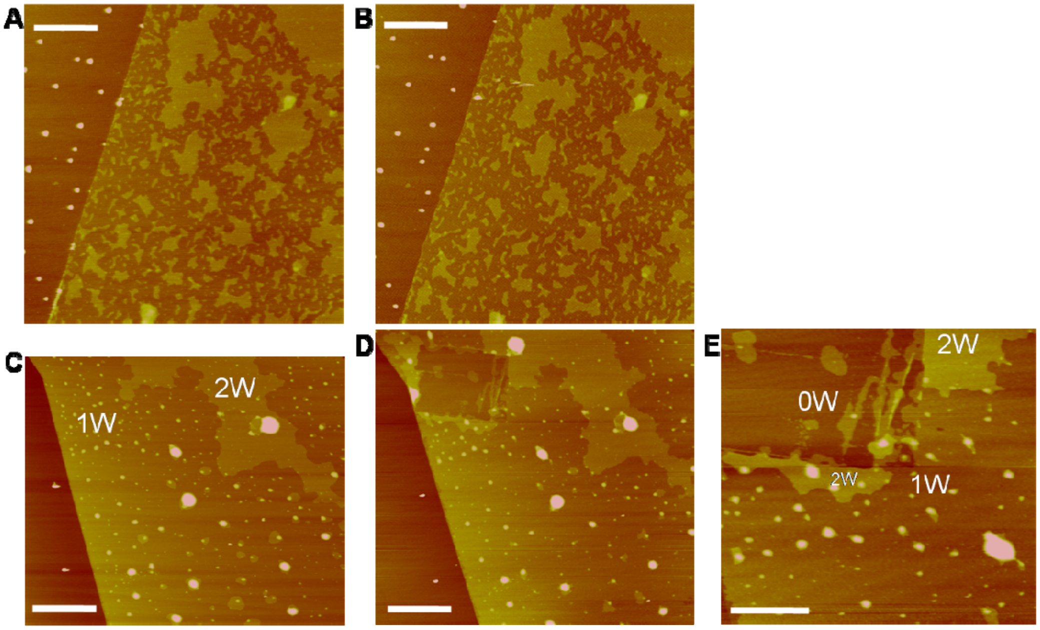

Figure 5.8. Stability of the graphene-fixed water patterns. (**A**) Another representative AFM image of a monolayer graphene sheet deposited on mica at ambient conditions. (**B**) The same sample, after being kept at ambient conditions for 25 days. No appreciable change of morphology is observed for the water patterns fixed by graphene. (**C**) An AFM image of monolayer graphene covering both the first (1W) and the second (2W) water adlayers on a mica substrate [from Figure 5.10D; realigned with Figure 5.8(D)]. (**D**) The same sample, after the entire mica substrate (~0.1 mm thick) was bent upwards by ~15 degrees. This excessive bending caused shear and partial displacement of graphene, and the water adlayer reorganized accordingly (upper left corner of the image). (**E**) A close-up of the change in (D). 0W, 1W, and 2W label the regions where graphene is on top of 0, 1, and 2 adlayers of water, respectively. During bending, water was squeezed out of a square ~1 μm in size and piled up at the edges of the square. Wrinkle-like features attributable to bending were also observed. Such square-like and wrinkle-like features are not observed in any samples that have not been subjected to extensive bending. Scale bars: 500 nm for (A), (B), and (E). 1 μm for (C) and (D). The same height scale (4 nm) is used for all images.

The fixed patterns are remarkably stable: besides preventing any appreciable changes of morphology during the several hours of our AFM operation, we found the patterns are stable for weeks under ambient conditions (Figure 5.8). We note, however, that the water adlayer can become mobile again when the mica substrate is subjected to extensive bending (Figure 5.8). Bending causes significant shear and displacement of graphene on the mica surface, thus releasing the locked water. The adlayer reorganizes accordingly, reflecting its dynamic nature.

The boundaries of the islands formed by the first water adlayer often exhibit fascinating polygonal shapes, with preferred angles of ~120°. For example, the arrow in Figure 5.4F points to an island with multiple 120° corners. This suggests at ambient conditions, the first water adlayer has an ice-like structure that is in epitaxial relationship with the substrate, similar to what was previously observed for the second water adlayer.[4, 13] This conclusion is further corroborated by the fact that all the islands have the same height as a single layer of ice, and is consonant with previous sum-frequency-generation spectroscopy results obtained over large areas.[8] The observed submonolayer coverage at ambient conditions is also consistent with previous macroscopic optical studies,[5, 7, 9] which indicated one statistical monolayer coverage at RH~75%, and a surface coverage of ~50% at RH~40%. In stark contrast to mica, graphitic surfaces (including graphene) are highly hydrophobic,[39, 40] and water is known to only adsorb on graphitic surfaces below ~150 K.[41] Therefore, in the sandwich structure (Figure 5.4A) no water is expected to come from the graphene side. The occasionally observed dot-like thicker features are possibly due to surface defects that attract water, as discussed below.

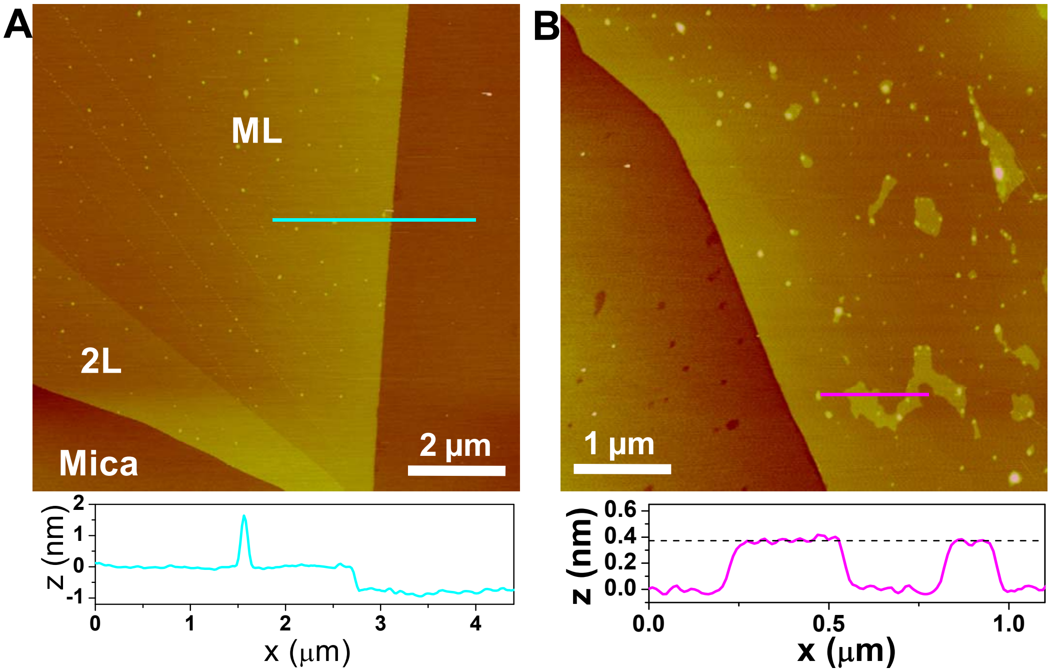

Figure 5.9. AFM images of graphene deposited on mica at RH ~2%, revealing the influence of surface defects on water adlayer nucleation. (**A**) A representative sample. ML: monolayer graphene. 2L: bilayer graphene. A dot-like defect is highlighted in the height profile across the cyan line. (**B**) Image of monolayer graphene deposited on a mica surface with high density of surface defects. A height profile is given for the pink line. The dash line indicates z = 0.37 nm. The same height scale (4 nm) is used for both images.

To investigate how the water adlayers evolve as the environmental humidity varies, we deposited graphene onto mica under controlled RH, and characterized the samples with AFM at ambient conditions. These studies also permitted investigations into the role that surface defects play in the initial formation of water adlayers. Figure 5.9A presents an AFM image of graphene deposited on mica under dry conditions (RH ~2%). No island-like structures are observed for most samples prepared in this way: graphene lies atomically flat[29] (Figure 5.5) without observable features, except for sporadic dot-like structures ~2 nm in height, which are likely due to surface defects. This agrees with previous optical studies, which indicated[7, 9] no reliably detectable water adsorption on mica surfaces at RH~2%.

The measured height of monolayer graphene on bare mica surface is sensitive to the specific settings of AFM, and can vary from 0.4-0.9 nm. Similar height variations are observed for monolayer graphene on SiO_2 (0.5 to 1 nm),[31, 42] and are attributed to the large chemical contrast between graphene and the substrate.[31] This is why Raman spectroscopy provides such a useful probe for distinguishing graphene monolayers from bilayers and thicker films. The heights of the water islands in this study, however, can be accurately determined: the AFM tip is always interacting with the *same* material (graphene) that uniformly coats the underlying sample (Figure 5.4A); variations in tip-sample interactions are avoided.

Patchy islands are occasionally observed for graphene deposited at 2% RH, on mica surfaces that are characterized by a high density of surface defects (Figure 5.9B). The same height of ~0.37 nm is again measured for those islands, indicating a single adlayer of water. Interestingly, most islands connect nearby defects, suggesting the importance of defects for water adlayer nucleation. The adlayer boundaries appear round near the defect sites, but resume the 120° polygonal shape away from the defects, indicating a competition between capillary interactions and the epitaxial interactions with the substrate.

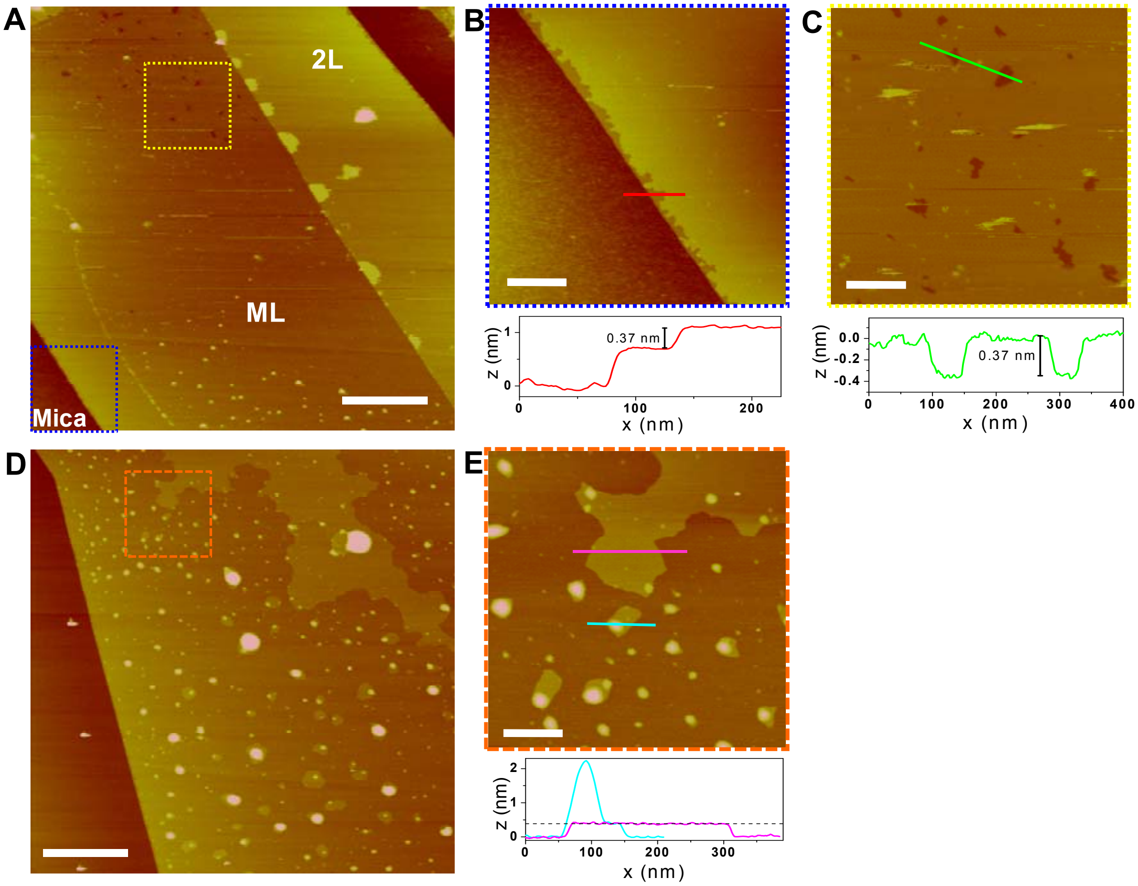

Figure 5.10. AFM images of graphene deposited on mica at RH ~90%, revealing the structure of the second water adlayer. (**A**) A representative sample. ML: monolayer graphene. 2L: bilayer graphene. (**B**) A close-up of the graphene edge, corresponding to the blue square at the bottom left of (A). A height profile is given for the red line. The first step (~0.7 nm in height) corresponds to monolayer graphene on bare mica. The second step (~0.37 nm) corresponds to the first water adlayer on mica, which has been sealed by the graphene. **(C)** A close-up of the pinholes, corresponding to the yellow square in (A). A height profile is given for the green line. (**D**) Image of monolayer graphene deposited on mica with a high density of surface defects. (**E**) A close-up of the *second* adlayer islands, corresponding to the orange square in (D). Height profiles are given for the pink and cyan lines. The dash line indicates z = 0.38 nm. Scale bars: 1 μm for (A) and (D), 200 nm for other images. The same height scale (4 nm) is used for all images.

When graphene is deposited on mica at high humidity (RH ~90%), the samples typically appear flat over large areas (Figure 5.10A). However, a closer look at the edge of the graphene sheets reveals that the graphene rides on top of a near-complete monolayer of water adlayer (Figure 5.10B). At about 10 nm from the edge of the graphene-water-mica sandwich structure, water evaporates away and graphene comes into direct contact with the mica surface, sealing and preserving the remaining water adlayers. The ~0.37 nm height (Figure 5.10B) indicates that the trapped water is a single adlayer. Polygonal pinholes ~10 nm in lateral size and ~0.37 nm in depth are also observed on the overall continuous adlayer (Figure 5.10C), indicating the monolayer is not 100% complete.

Different results are obtained for graphene deposited, at 90% RH, on a mica characterized by a high density of surface defects (Figure 5.10D). Besides a completed (no pinholes) first adlayer of water that is only missing at the graphene sheet edge, islands of various lateral sizes are observed on *top* of the first adlayer, often surrounding or connecting local defect sites. These islands are atomically flat (Figure 5.5), and are 0.38±0.02 nm in height over the first adlayer (Figure 5.10E), again in agreement with the height of a single "puckered bilayer" of ice (0.369 nm). The observed ~120° polygonal shapes of these islands agree with previous SPFM results on tip-induced second water adlayers.[4, 13, 14] Thus, the islands observed in Figure 5.10DE are the *second* water adlayer, which also has an ice-like structure at room temperature and is in epitaxial relationship with the first adlayer. Bulge-like features a few nanometers in height are also observed, but appear to be liquid-like (roundish) and have varying heights. No ice-like islands or plateaus were observed beyond the second adlayer. Previous optical studies[5, 7, 9] indicated only a few statistical adlayers on the mica surface exist at RH~90%, but with large sample-to-sample variations - a result that is consistent with the observations reported here.

In summary, we find that graphene monolayers can provide an atomically flat surface coating that can enable measurements of the structures of the first water adlayers on mica at room temperature and at variable humidity. Under ambient conditions, water adlayers grow epitaxially on mica in a strictly layer-by-layer fashion: the second adlayer only forms after the first adlayer is fully completed. In the submonolayer regime, two-dimensional islands form due to interactions between adsorbed molecules, possibly akin to the Frank-van-der-Merwe growth mechanism in heteroepitaxy.[43] This result is consistent with previous studies that indicated the absence of dangling O-H bonds[8] and a minimum in entropy[9] at one statistical monolayer coverage. It also explains why water adsorption isotherms cannot be modeled with theories based on continuum models[7]. Our findings also highlight the role that surface defects play in water adsorption: defects apparently serve as nucleation centers for the formation of both the first and second adlayers. The importance of surface defects helps explain the large sample-to-sample variations previously reported in isotherm measurements.[5, 7] The use of STM[44-46] to characterize the atomic structures of graphene on water adlayers represents an exciting future challenge.

5.4 THF and cyclohexane on mica

Figure 5.11a shows a schematic of the graphene templating technique for investigating the structures of molecular layers of small organic molecules weakly adsorbed on the mica surface.

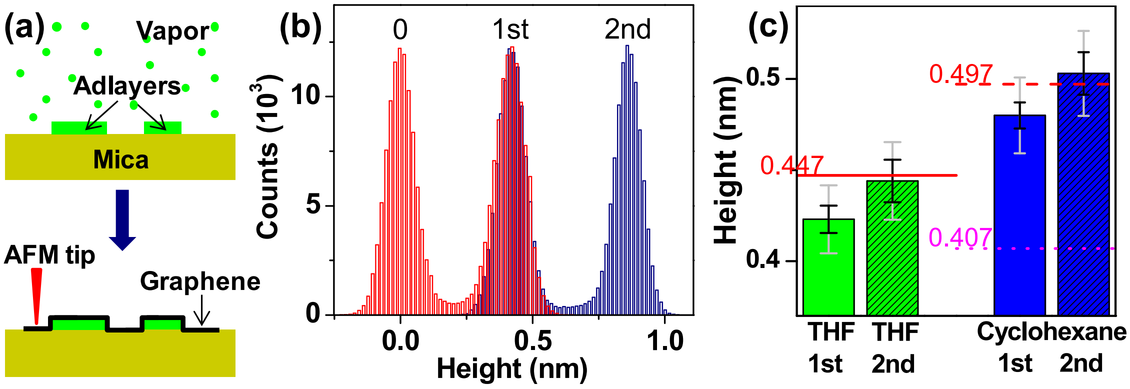

Figure 5.11. Graphene templating illustration (a) and representative measurements of adsorbed adlayer thicknesses (b,c). (b): Representative measurements of THF adlayer heights, from two AFM images, at the borders between 0 and 1 (red), and 1 and 2 (blue) adlayers. The two distributions are overlaid according to the peak centers of the first adlayer. The heights for the first and second adlayers are respectively determined to be 0.420 and 0.446 nm for the two specific samples. **(c)**: Statistics of the measured heights for the first and second adlayers of THF and cyclohexane on mica, obtained from ~10 samples for each adlayer. The indicated uncertainties (95% confidence) are for when the systematic error in height calibration is excluded (black) and included (grey). Red lines mark the known layer heights in the bulk crystals of THF (monoclinic) and cyclohexane (Phase I) that are in agreement with our data. The pink dotted line marks the layer height for a different crystal phase (Phase II) of cyclohexane crystal, and is in clear disagreement with our data.

Samples were prepared at room temperature (~22 °C) and a relative humidity of <2%, under which the adsorption of water on mica surfaces can be neglected.[1] Freshly cleaved mica surfaces were brought into contact with organic vapors and allowed to equilibrate for ~1 min. The partial pressure of organic molecules at the mica surface, which determines the surface coverage at equilibrium, was adjusted by varying the distance between the vapor source and the mica. Graphene sheets were deposited onto the mica surface, sealing and preserving the adlayer structures. Samples were then removed from the organic vapors and imaged with AFM under ambient conditions.

Adlayer heights in each sample were determined by scanning over small (~200 nm) areas across adlayer borders, and plotting the distribution of all height values within the AFM images (Figure 5.11b). The final heights reported for THF and cyclohexane adlayers were summarized from the height values thus obtained from ~10 different images (Figure 5.11c).

Figure 5.12 presents typical AFM images of monolayer graphene sheets deposited on mica surfaces that were in equilibrium with THF vapors. Atomically flat islands/plateaus are observed across all graphene sheets. In comparison, no such structures are observed on mica surfaces that are not covered by graphene. Phase images,[1] which are more reflective of the local chemical properties of the surface rather than the topography,[37] indicate that the observed flat islands are THF adlayers trapped under the graphene, similar to the case of water adlayers in our previous study.[1] The numbers of THF adlayers, as labeled in Figure 5.12, were determined from measured heights and careful tracing of the extreme edges of graphene sheets, where the adlayers under graphene tend to evaporate away and leave the graphene in direct contact with the bare mica surface.[1]

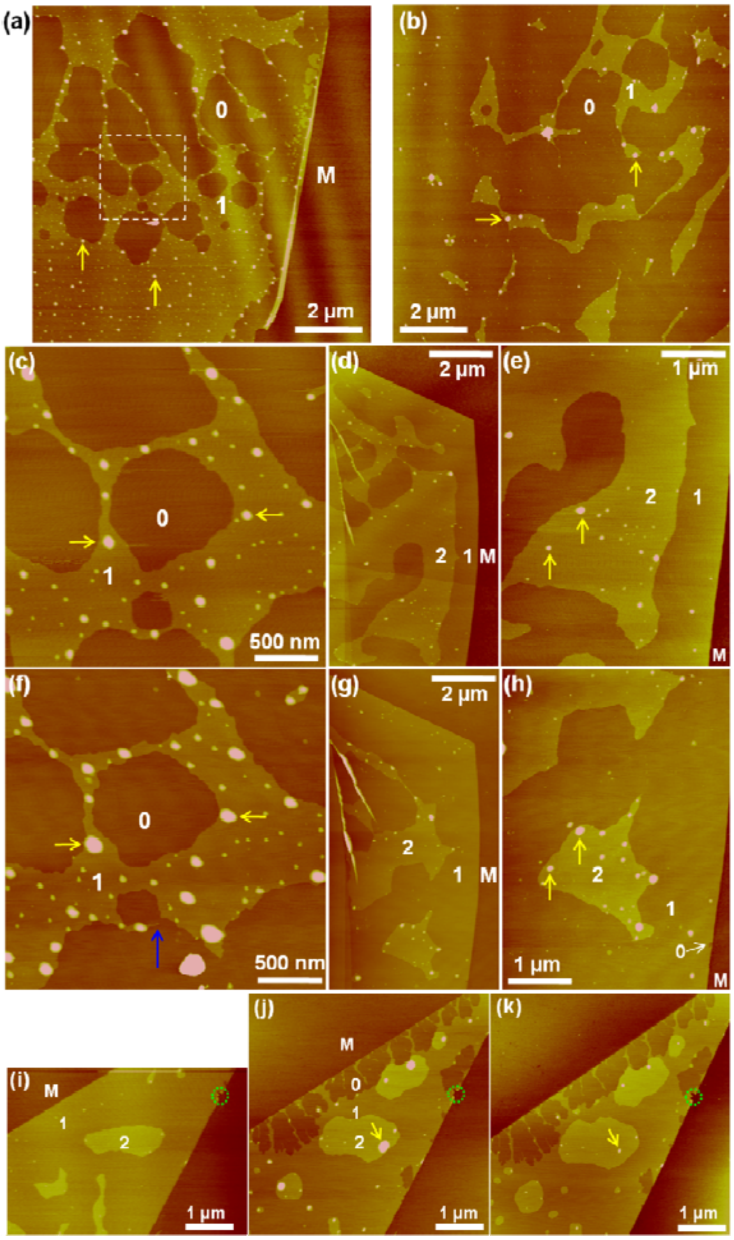

Figure 5.12. AFM images of graphene-templated THF adlayers reveal both structural and dynamical information. M labels the mica surface, and 0, 1 and 2 label regions where monolayer graphene is on top of 0, 1 and 2 adlayers of THF, respectively. Yellow arrows point to droplets. (a)-(e) were taken within a few hours after graphene sheets were deposited. **(a)**: The case in which the trapped adlayer is a submonolayer. **(b):** Another sample with very low surface coverage of THF. **(c):** Zoom-in of the square in (a). **(d):** Another sample showing the second THF adlayer on top of the first. **(e):** Zoom-in of the second adlayer in (d). **(f-h):** The same areas as (c-e), after the samples were kept at ambient conditions for 2 months. **(i-k):** Another sample freshly prepared (i), and after being kept at ambient conditions for 60 days (j) and 68 days (k). The green circles mark a defect on the graphene edge, which served as a reference point for aligning the images.

Interestingly, similar to what was found for water,[1] a layer-by-layer growth mechanism is observed for the first two adlayers of THF molecules: the second adlayer only forms after the first adlayer is completed (Figure 5.12de), and two-dimensional (2D) flat islands are observed for both layers, similar to the Frank-van-der-Merwe growth mechanism in heteroepitaxy.[43] No molecularly flat, island-like structures are seen beyond the second adlayer; droplets are observed to coexist with both the first and second adlayers. This general mechanism, however, is not universal: it can be altered by chemical modification of the mica surface. For example, very different behavior is observed for water adlayers adsorbed on trimethylchlorosilane-functionalized (somewhat hydrophobic; H_2O contact angle ~ 40^o) mica. The adlayer structures that initially adsorb, as observed via graphene templating, are three-dimensional nanodroplets only, with no obvious crystalline structure (Figure 5.13). Those results indicate multiple types of adlayer growth mechanisms can be achieved via chemical modification of the underlying mica substrate, and can be preserved and imaged using graphene templating.

Figure 5.12a-c present the case in which the trapped adlayer is a submonolayer. Large, interconnecting islands coexist with areas where no adlayer is present. At low surface coverage, the adlayers tend to form narrow “necks” as opposed to isolated small islands (Figure 5.12b). This contrasts with what is seen for submonolayers of water, where isolated and scattered small islands, typically ~10 nm in lateral size, are observed[1] (see also Figure 5.8). This result suggests that, relative to water, THF molecules interact more weakly with the mica surface, so the interactions between THF molecules dominate and lead to more continuous adlayers.

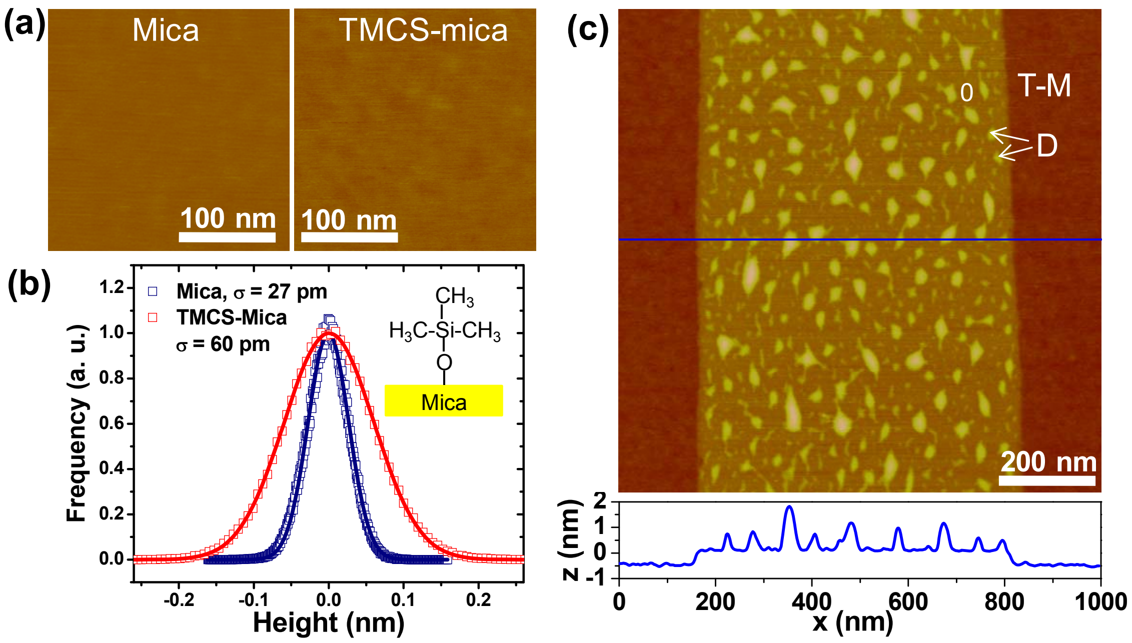

Figure 5.13. Water adsorption on TMCS-functionalized mica surfaces at ambient conditions. (a): AFM images indicate a uniform surface passivation of mica by TMCS. However, the functionalized surface, although still very flat, is rougher than what is observed for freshly cleaved mica. **(b):** Height histograms of a fresh mica surface and a TMCS-functionalized mica surface. The measured RMS roughness of fresh mica (27 pm) is likely limited by the noise of AFM, whereas the roughness of TMCS-functionalized mica surface is significantly higher (60 pm). There is, however, no evidence that TMCS functionalization introduces etch pits or other large defects into the mica. The inset is a simple molecular drawing of TMCS-functionalized mica. **(c):** Graphene-templating reveals that under ambient conditions (~40% RH), water adsorbs as nanometer-sized droplets on the relatively hydrophobic TMCS-functionalized mica surface. “T-M” labels TMCS-functionalized mica surface, “0” labels where monolayer graphene is in direct contact with the TMCS-functionalized mica surface, and “D” points to two droplets. A cross-sectional profile is given for the blue line, which indicates the droplets have varying heights on the order of ~1-2 nm. These results contrast with the flat 2D islands typically observed for adlayers on fresh (hydrophilic) mica surfaces.

The boundaries of the islands formed by the first THF adlayers often appear rounded (Figure 5.12a-c). Similar rounded boundaries are also observed at the missing edges of full monolayers (not shown here). These results suggest that the first THF adlayer has at least some liquid-like characteristics. The second adlayers (Figure 5.12de), on the other hand, exhibit both rounded and faceted boundaries. As will be discussed below, the rounded boundaries of THF adlayers become increasingly faceted over time scales of weeks, suggesting, again, that these adlayers possess both liquid and solid properties at room temperature. These results also contrast with water, for which both the first and second adlayers appear ice-like at room temperature, and are characterized by faceted boundaries with preferred angles of ~120°.[1, 4, 13]

The heights of the first and second THF adlayers on the mica surface were measured, across ~10 samples, to be 0.42±0.02 and 0.44±0.02 nm, respectively (95% confidence; Figure 5.11c). The height of the second adlayer is in good agreement with the layer thickness in THF crystals: THF crystallizes in the monoclinic space group $C2/c$, and the layer thickness in the b direction is $b/2$ = 0.447 nm (Figure 5.11c).[47-49] In this direction, THF molecules "stand up" with the oxygen atoms in the rings alternatively pointing towards and away from the substrate.[49] This also corresponds to the polarity direction for THF molecules. The height of the first adlayer is statistically thinner than the second adlayer: when the (systematic) uncertainty in height calibration is ignored, the heights of the first and second THF adlayers can be expressed as 0.423±0.008 and 0.444±0.012 nm, respectively. This result suggests the first THF adlayer may be slightly thinner than the layer thickness in the crystal (Figure 5.11c), possibly indicating that the first adlayers are slightly tilted due to interactions with the substrate (Figure 5.15ab), a phenomenon often encountered in self-assembled monolayers on substrates.[50]

Although the graphene-templated THF adlayers are stable over time scales of hours (e.g., the same structures are observed for images taken at different magnifications over periods of several hours), noticeable structural changes are observed over the time scale of weeks. This result is in contrast to graphene-templated water adlayers, which are stable for at least months under ambient conditions (Figure 5.8).[1] In most cases, the THF adlayers shrink in lateral dimensions to form droplets (Figure 5.12f-h). Narrow "necks" in the adlayers thus tend to break (blue arrow in Figure 5.12f). The boundaries of the THF adlayers also often adopt facets during the reorganization (Figure 5.12f-h). These observations are reminiscent of the coalescence of molecularly thin clusters/islands often encountered during the post-deposition relaxation processes in thin film deposition.[51-53] In our case, adlayers are sealed under graphene, so the vapor-adlayer equilibrium is removed for the otherwise volatile molecules. The adlayers thus relax in a manner that is similar to deposited nonvolatile thin films. We further note that after the adlayers are allowed to relax for sufficiently long periods (Figure 5.12ij); reverse processes, in which droplets shrink in size to form larger adlayer islands, are also occasionally observed (Figure 5.12k). Such reversible island-droplet-island transitions are likely due to thermal fluctuations, and are consistent with the idea that all of the adlayer structures observed here are within a few k_BT of energy.

The observations on the THF adlayers imply both liquid-like and crystalline characteristics at room temperature. This is remarkable since room temperature is ~130 K higher than the bulk melting point of THF (-108.4 °C). The coexistence of solid-like and liquid-like layers have been recently observed for the ionic liquid Bmim-PF_6 on mica surfaces.[54] However, the melting point of Bmim-PF_6 (6.6 °C) is close to room temperature, and the liquid-like and solid-like structures observed in Bmim-PF_6 films, which are of unknown thicknesses,[54] likely only reflect the differences between bulk and adlayer properties. The faceted yet mobile adlayers we observed have not been previously reported. One possible explanation of our result is that the THF adlayers are in a "hexatic" phase that is between the solid and liquid phases. In three dimensions, liquid-solid transitions are necessarily first-ordered and abrupt; for 2D systems the liquid-solid transition may occur continuously, through the intermediate "hexatic" phase, and over a wide temperature range.[55-57]

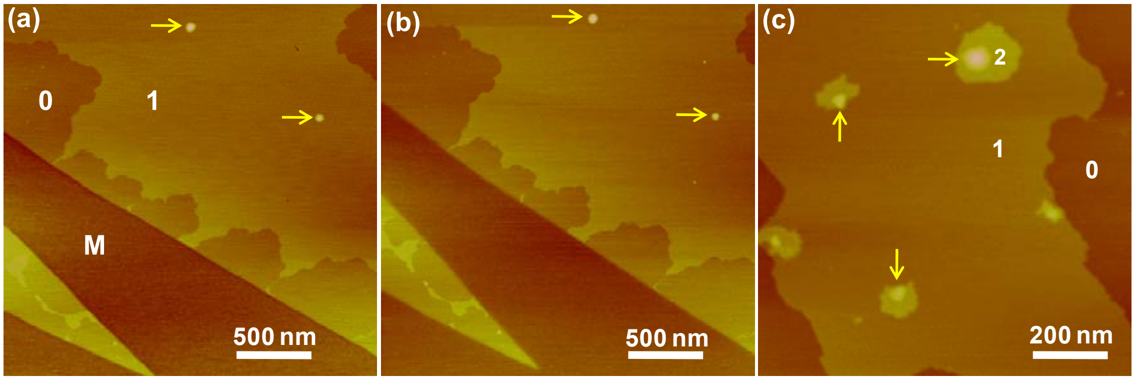

Figure 5.14. AFM images of graphene-templated cyclohexane adlayers. M labels the mica surface, and 0, 1 and 2 label regions where monolayer graphene is on top of 0, 1, and 2 adlayers of cyclohexane, respectively. Yellow arrows point to droplets. **(a):** A typical image of graphene-templated submonolayer cyclohexane adlayer, taken within a few hours after graphene was deposited. **(b):** The same area, but imaged after the sample was stored at ambient conditions for 2 months. **(c):** Another sample showing the second cyclohexane adlayers.

Figure 5.14 presents typical AFM images of monolayer graphene deposited on mica surfaces that were in equilibrium with cyclohexane vapors at room temperature. Similar to the case of both water and THF adlayers, a layer-by-layer growth mechanism is generally observed for cyclohexane adlayers, and atomically flat 2D islands are observed for both the first and the second adlayers. The surface coverage of cyclohexane on the mica surface is usually low, and so the second adlayer was only occasionally observed, typically surrounding droplets that are likely attracted by surface defects (Figure 5.14c). This result possibly reflects the weaker interaction between the non-polar cyclohexane molecules and the mica surface.

Similar to the case of THF, but different from water, cyclohexane adlayers form large, continuous islands on mica, indicating weak molecule-substrate interactions. On the other hand, similar to the case of water but different from THF, the boundaries of all cyclohexane adlayers appear faceted, suggesting the adlayers are crystal-like at room temperature. In addition, under ambient conditions the graphene-templated cyclohexane adlayers are found to be stable for months without noticeable structural changes (Figure 5.14b), again indicating that the adlayers are solid-like at room temperature, similar to the case of water adlayers (Figure 5.8). The crystallinity of the cyclohexane adlayers, relative to THF adlayers, is likely due to the large difference in melting points (6.7 ^{o}C vs. -108.4 ^{o}C), and suggests that the interaction between adsorbed molecules plays an important role in determining the adlayer structure.

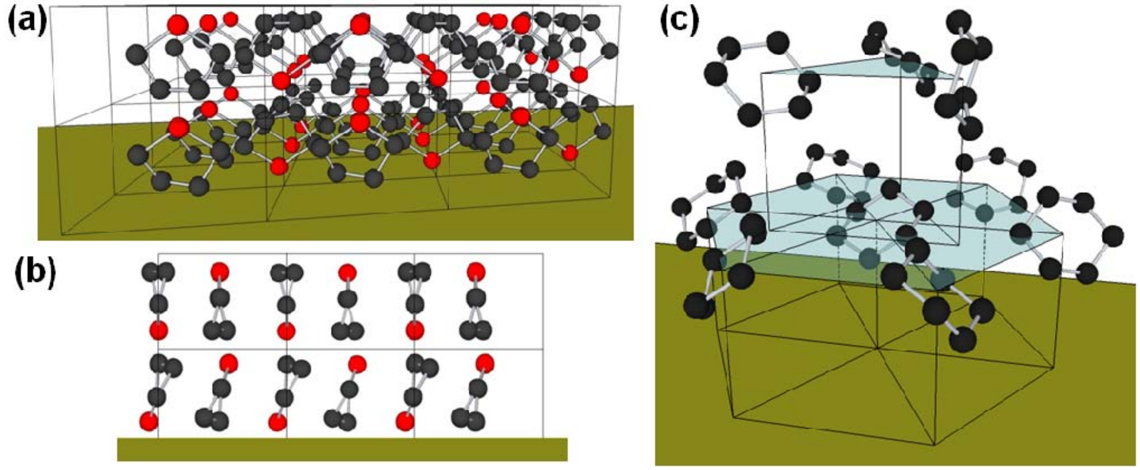

Figure 5.15. Possible structural models for THF and cyclohexane adlayers. Black and red balls represent carbon and oxygen atoms, respectively. Hydrogen atoms are omitted for clarity. **(a,b):** Possible structure of the first two adlayers of THF, basing on the monoclinic crystal structure of THF. (a): Perspective view. (b): Side view. The first adlayer may be tilted due to molecule-substrate interactions. **(c):** Instantaneous view of the possible structure of the first two adlayers of cyclohexane. The structure is based on the (111) direction of the fcc lattice of the Phase I "plastic crystal" structure of cyclohexane. Each molecule is free to rotate about its center, and so this view represents one instantaneous snapshot. The rotational freedom may be lower for the first adlayer.

The heights of the first and second cyclohexane adlayers on the mica surface, across different samples, are measured to be 0.48±0.02 and 0.50±0.02 nm, respectively (Figure 5.11c). These values are in good agreement with the layer thickness of the Phase I crystal structure of cyclohexane. Phase I is the stable phase for bulk cyclohexane between 279.8 K and 186 K. The unit cell is face-center cubic (fcc) with a = 0.861 nm.[58, 59] The layer thickness in the (111) direction (i.e., a close-packed hexagonal single layer; Figure 5.15c) is thus $a/\sqrt{3}$ ~0.497 nm (Figure 5.11c). Previous low-energy electron diffraction (LEED) studies[26, 27] over large areas of cyclohexane adlayers on Pt(111) and Ag(111) surfaces indicated that for $T <\sim 200$ K, cyclohexane adsorbs as a monoclinic phase, which is consistent with the Phase II crystal structure. That structure is known to be stable for $T < 186$ K in bulk. According to the Phase II arrangement, the cyclohexane rings would lie roughly parallel to the substrate,[26, 27] and the layer thickness should be $\sim c/2 \sin\beta = 0.407$ nm.[58] That value is significantly smaller than the adlayer heights we measured (Figure 5.11c). No LEED patterns were observed in previous studies for $T >\sim 200$ K, where cyclohexane adlayers evaporated in vacuum.[26, 27] Thus, our results suggest at room temperature, cyclohexane adlayers crystallize as Phase I (Figure 5.15c). Phase I of cyclohexane is plastic crystal, meaning that although molecules form ordered crystal lattices, they are still free to rotate about the lattice points.[58, 59] The layer height is larger than for the case of Phase II, in which all molecules lie "flat" on substrate. Similar to the case of THF, and neglecting the systematic uncertainty in height calibration, the height of the first adlayer of cyclohexane (0.480±0.007) is statistically thinner than the second adlayer (0.503±0.012 nm) (Figure 5.11c). One possibility is that interactions with the substrate may restrain the rotation of first adlayer cyclohexane molecules on the mica surface (Figure 5.15c).

We have reported on the room-temperature structures and dynamics of weakly bound adlayers at the interfaces between solids and vapors of small organic molecules by using graphene templating. We found cyclohexane adlayers on mica are crystal-like at room temperature, whereas THF adlayers possess both liquid and solid properties. The heights of the second adlayers of THF and cyclohexane are in agreement with the layer thicknesses in the monoclinic crystal structure of THF and the Phase I "plastic crystal" structure of cyclohexane. The first adlayers of both molecules appear slightly thinner, indicative of molecule/mica interactions. A layer-by-layer growth mechanism has so far been consistently observed for the first two adlayers of water, THF, and cyclohexane molecules on freshly cleaved mica. Previous studies indicated that for nonvolatile, large organic molecules, layer-by-layer spreading also occurs on flat substrates, both for molecules that are solid[21, 23, 24] and liquid[19, 20, 54] at room temperature. The striking consistency and similarity across different systems suggest that the layer-by-layer mechanism may be broadly applicable for molecular adsorbates on many atomically flat surfaces, although more experiments are required to validate this hypothesis.

An outstanding question involves the influence that the graphene exerts on the adlayer structure. All of our findings to date indicate that graphene templating permits unprecedented high-resolution views of weakly bound molecular adlayers, and the resultant data is wholly consistent with previous findings. This indicates that, at least for some systems, graphene templating provides a relatively innocent structural probe. However, it is likely that detailed quantum mechanical calculations will be required to more fully address this question, and that the answer will be system-dependent.

5.5 Conclusion

In this chapter, graphene templating is utilized to visualize the first adlayers of water and small organic molecules (THF and cyclohexane) on mica at ambient conditions, revealing how the atomic structure of the adlayers evolves at the nanometer/molecular scale.

Due to its dynamic nature, the room-temperature microscopic structure of the first water adlayers on solid surfaces has been challenging to detect. By employing graphene as an atomically flat coating for atomic force microscopy, we measured the structure of the water adlayers on mica at room temperature, and as a function of relative humidity. We found that water adlayers grow epitaxially on the mica substrate in a layer-by-layer fashion. Submonolayers form atomically flat, faceted islands of height 0.37±0.02 nm, in agreement with the height of a monolayer of ice. The second adlayers, observed at higher relative humidity, also appear ice-like, and thicker layers appear liquid-like. Our results also indicate nanometer-scale surface defects serve as nucleation centers for the formation of both the first and second adlayers.

In the remainder of the chapter, we report on the use of graphene templating to investigate the room-temperature structure and dynamics of weakly bound adlayers at the interfaces between solids and vapors of small organic molecules. Monolayer graphene sheets are employed to preserve and template molecularly thin adlayers of tetrahydrofuran (THF) and cyclohexane on atomically flat mica substrates, thus permitting a structural characterization of the adlayers under ambient conditions through atomic force microscopy. We found the first two adlayers of both molecules adsorb in a layer-by-layer fashion, and atomically flat two-dimensional islands are observed for both the first and the second adlayers. THF adlayers form initially as rounded islands, but over a time period of weeks evolve into faceted islands, suggesting that the adlayers possess both liquid and solid properties at room temperature. Cyclohexane adlayers form crystal-like faceted islands, and are immobile under the graphene template. Precise adlayer height measurements further permitted the identification of the crystal structures of the adlayers. The heights of the second adlayers of THF and cyclohexane are measured to be 0.44±0.02 and 0.50±0.02 nm, respectively, in good agreement with the layer thicknesses in the monoclinic crystal structure of THF and the Phase I “plastic crystal” structure of cyclohexane. The first adlayers appear slightly thinner for both molecules, indicative of interactions of the molecules with the mica substrate.

5.6 References

1. Xu, K., Cao, P.G. & Heath, J.R. Graphene visualizes the first water adlayers on mica at ambient conditions. *Science* **329**, 1188-1191 (2010).
2. Cao, P.G., Xu, K., Varghese, J.O. & Heath, J.R. Atomic force microscopy characterization of room-temperature adlayers of small organic molecules through graphene templating. *J Am Chem Soc* **133**, 2334-2337 (2011).
3. Thiel, P.A. & Madey, T.E. The interaction of water with solid-surfaces: fundamental aspects. *Surf. Sci. Rep.* **7**, 211-385 (1987).
4. Verdaguer, A., Sacha, G.M., Bluhm, H. & Salmeron, M. Molecular structure of water at interfaces: Wetting at the nanometer scale. *Chem Rev* **106**, 1478-1510 (2006).
5. Ewing, G.E. Ambient thin film water on insulator surfaces. *Chem Rev* **106**, 1511-1526 (2006).
6. Feibelman, P.J. The first wetting layer on a solid. *Phys. Today* **63(2)**, 34-39 (2010).
7. Beaglehole, D., Radlinska, E.Z., Ninham, B.W. & Christenson, H.K. Inadequacy of Lifshitz theory for thin liquid-films. *Phys Rev Lett* **66**, 2084-2087 (1991).
8. Miranda, P.B., Xu, L., Shen, Y.R. & Salmeron, M. Icelike water monolayer adsorbed on mica at room temperature. *Phys Rev Lett* **81**, 5876-5879 (1998).
9. Cantrell, W. & Ewing, G.E. Thin film water on muscovite mica. *J Phys Chem B* **105**, 5434-5439 (2001).
10. Bluhm, H. & Salmeron, M. Growth of nanometer thin ice films from water vapor studied using scanning polarization force microscopy. *J. Chem. Phys.* **111**, 6947-6954 (1999).
11. Ogawa, K. & Majumdar, A. Molecular-level imaging of ice crystal structure and dynamics by atomic force microscopy. *Microscale Thermophys. Eng.* **3**, 101-110 (1999).
12. Piner, R.D. & Mirkin, C.A. Effect of water on lateral force microscopy in air. *Langmuir* **13**, 6864-6868 (1997).

13. Hu, J., Xiao, X.D., Ogletree, D.F. & Salmeron, M. Imaging the condensation and evaporation of molecularly thin-films of water with nanometer resolution. *Science* **268**, 267-269 (1995).

14. Xu, L. & Salmeron, M. in Nano-Surface Chemistry. (ed. M. Rosoff) 243-287 (Marcel Dekker, New York; 2001).

15. Weaver, J.F., Carlsson, A.F. & Madix, R.J. The adsorption and reaction of low molecular weight alkanes on metallic single crystal surfaces. *Surf. Sci. Rep.* **50**, 107-199 (2003).

16. Goss, K.U. The air/surface adsorption equilibrium of organic compounds under ambient conditions. *Crit. Rev. Environ. Sci. Technol.* **34**, 339-389 (2004).

17. Bruch, L.W., Diehl, R.D. & Venables, J.A. Progress in the measurement and modeling of physisorbed layers. *Rev. Mod. Phys.* **79**, 1381-1454 (2007).

18. Beaglehole, D. & Christenson, H.K. Vapor adsorption on mica and silicon - entropy effects, layering, and surface forces. *J. Phys. Chem.* **96**, 3395-3403 (1992).

19. Xu, L., Salmeron, M. & Bardon, S. Wetting and molecular orientation of 8CB on silicon substrates. *Phys Rev Lett* **84**, 1519-1522 (2000).

20. Xu, L. et al. De-wetting of lubricants on hard disks. *J. Chem. Phys.* **112**, 2952-2957 (2000).

21. Lazar, P., Schollmeyer, H. & Riegler, H. Spreading and two-dimensional mobility of long-chain alkanes at solid/gas interfaces. *Phys Rev Lett* **94**, 116101 (2005).

22. Riegler, H. & Kohler, R. How pre-melting on surrounding interfaces broadens solid-liquid phase transitions. *Nat. Phys.* **3**, 890-894 (2007).

23. Trogisch, S. et al. Atomic force microscopy measurements of topography and friction on dotriacontane films adsorbed on a SiO_2 surface. *J. Chem. Phys.* **123**, 154703 (2005).

24. Cisternas, E.A. et al. Crystalline-to-plastic phase transitions in molecularly thin n-dotriacontane films adsorbed on solid surfaces. *J. Chem. Phys.* **131**, 114705 (2009).

25. Giancarlo, L.C. & Flynn, G.W. Scanning tunneling and atomic force microscopy probes of self-assembled, physisorbed monolayers: peeking at the peaks. *Annu Rev Phys Chem* **49**, 297-336 (1998).

26. Firment, L.E. & Somorjai, G.A. Surface-structures of normal paraffins and cyclohexane monolayers and thin crystals grown on (111) crystal-face of platinum - low-energy electron-diffraction study. *J. Chem. Phys.* **66**, 2901-2913 (1977).

27. Firment, L.E. & Somorjai, G.A. Low-energy electron-diffraction study of surface of thin crystals and monolayers of normal paraffins and cyclohexane on Ag(111) crystal-surface. *J. Chem. Phys.* **69**, 3940-3952 (1978).

28. Novoselov, K.S. et al. Two-dimensional atomic crystals. *Proc. Natl. Acad. Sci. U. S. A.* **102**, 10451-10453 (2005).

29. Lui, C.H., Liu, L., Mak, K.F., Flynn, G.W. & Heinz, T.F. Ultraflat graphene. *Nature* **462**, 339-341 (2009).

30. Nair, R.R. et al. Fine structure constant defines visual transparency of graphene. *Science* **320**, 1308-1308 (2008).

31. Ferrari, A.C. et al. Raman spectrum of graphene and graphene layers. *Phys Rev Lett* **97**, 187401 (2006).

32. Graf, D. et al. Spatially resolved Raman spectroscopy of single- and few-layer graphene. *Nano Lett.* **7**, 238-242 (2007).

33. Fletcher, N.H. The chemical physics of ice. (Cambridge Univ. Press, London; 1970).

34. Lee, C. et al. Frictional characteristics of atomically thin sheets. *Science* **328**, 76-80 (2010).

35. Bunch, J.S. et al. Impermeable atomic membranes from graphene sheets. *Nano Lett.* **8**, 2458-2462 (2008).

36. Stolyarova, E. et al. Observation of graphene bubbles and effective mass transport under graphene films. *Nano Lett.* **9**, 332-337 (2009).

37. Garcia, R. & Perez, R. Dynamic atomic force microscopy methods. *Surf. Sci. Rep.* **47**, 197-301 (2002).

38. Doering, D.L. & Madey, T.E. The adsorption of water on clean and oxygen-dosed Ru(001). *Surf Sci* **123**, 305-337 (1982).

39. Leenaerts, O., Partoens, B. & Peeters, F.M. Water on graphene: hydrophobicity and dipole moment using density functional theory. *Phys Rev B* **79**, 235440 (2009).

40. Shin, Y.J. et al. Surface-energy engineering of graphene. *Langmuir* **26**, 3798-3802 (2010).

41. Bolina, A.S., Wolff, A.J. & Brown, W.A. Reflection absorption infrared spectroscopy and temperature-programmed desorption studies of the adsorption and desorption of amorphous and crystalline water on a graphite surface. *J Phys Chem B* **109**, 16836-16845 (2005).

42. Novoselov, K.S. et al. Electric field effect in atomically thin carbon films. *Science* **306**, 666-669 (2004).

43. Herman, M.A., Richter, W. & Sitter, H. Epitaxy: physical principles and technical implementation. (Springer, Berlin; 2004).

44. Ishigami, M., Chen, J.H., Cullen, W.G., Fuhrer, M.S. & Williams, E.D. Atomic structure of graphene on SiO_2. *Nano Lett.* **7**, 1643-1648 (2007).

45. Stolyarova, E. et al. High-resolution scanning tunneling microscopy imaging of mesoscopic graphene sheets on an insulating surface. *Proc. Natl. Acad. Sci. U. S. A.* **104**, 9209-9212 (2007).
46. Xu, K., Cao, P.G. & Heath, J.R. Scanning tunneling microscopy characterization of the electrical properties of wrinkles in exfoliated graphene monolayers. *Nano Lett.* **9**, 4446-4451 (2009).
47. David, W.I.F. & Ibberson, R.M. A reinvestigation of the structure of tetrahydrofuran by high-resolution neutron powder diffraction. *Acta Crystallogr. Sect. C-Cryst. Struct. Commun.* **48**, 301-303 (1992).
48. Luger, P. & Buschmann, J. Twist conformation of tetrahydrofuran in the crystal. *Angew. Chem.-Int. Edit. Engl.* **22**, 410-410 (1983).
49. Dziubek, K.F., Jeczminski, D. & Katrusiak, A. Pressure-generated hydrogen bonds and the role of subtle molecular features in tetrahydrofuran. *J. Phys. Chem. Lett.* **1**, 844-849 (2010).
50. Ulman, A. Formation and structure of self-assembled monolayers. *Chem Rev* **96**, 1533-1554 (1996).
51. Zinkeallmang, M., Feldman, L.C. & Grabow, M.H. Clustering on surfaces. *Surf. Sci. Rep.* **16**, 377-463 (1992).
52. Venables, J.A., Spiller, G.D.T. & Hanbucken, M. Nucleation and growth of thin-films. *Rep. Prog. Phys.* **47**, 399-459 (1984).
53. Evans, J.W., Thiel, P.A. & Bartelt, M.C. Morphological evolution during epitaxial thin film growth: Formation of 2D islands and 3D mounds. *Surf. Sci. Rep.* **61**, 1-128 (2006).
54. Liu, Y.D., Zhang, Y., Wu, G.Z. & Hu, J. Coexistence of liquid and solid phases of Bmim-PF_6 ionic liquid on mica surfaces at room temperature. *J Am Chem Soc* **128**, 7456-7457 (2006).
55. Strandburg, K.J. Two-dimensional melting. *Rev. Mod. Phys.* **60**, 161-207 (1988).
56. Binder, K., Sengupta, S. & Nielaba, P. The liquid-solid transition of hard discs: first-order transition or Kosterlitz-Thouless-Halperin-Nelson-Young scenario? *J. Phys.-Condes. Matter* **14**, 2323-2333 (2002).
57. Gasser, U., Eisenmann, C., Maret, G. & Keim, P. Melting of crystals in two dimensions. *ChemPhysChem* **11**, 963-970 (2010).
58. Kahn, R., Fourme, R., Andre, D. & Renaud, M. Crystal structures of cyclohexane I and II. *Acta Crystallogr. Sect. B-Struct. Commun.* **B 29**, 131-138 (1973).

59. Shigematsu, K., Hondo, H., Kumagai, T. & Takahashi, Y. Pressure effect on the solid I-liquid and solid III-solid I equilibrium forms of cyclohexane. *Cryst. Growth Des.* **9**, 4674-4679 (2009).

Chapter 6

Quartz Tuning Fork Based Low Temperature Atomic Force Microscopy

6.1 Introduction

The invention of scanning tunneling microscopy (STM) in 1982[1] and atomic force microscopy (AFM) in 1986[2] has enabled people to "see" atoms on solid surfaces, which is important to the understanding of surface microscopic structures and their relationship to both surface and bulk electronic and mechanical properties. Although AFM has a relatively lower resolution when compared to STM, the advantage of probing both conducting and non-conducting materials makes AFM a very popular tool in the surface science community.[3, 4] Over the past two decades, various efforts have been made to improve both the resolution and throughput of the AFM technique.[5] This includes sensor design in both static and dynamic AFM operation modes.

In static mode, a cantilever probe is brought to the surface and the deflection due to the sample-tip interactions is monitored via a laser detection system (Figure 6.1, left). The interaction force is thereby straightforwardly obtained from Hooke's law. The surface topography is mapped out by raster scanning the probe while controlling the distance via a feedback system to maintain a constant interaction force. Thus a three-dimensional image z(x, y, $F_{ts} \approx$ constant) is created, where z is height and the sample surface stays in the x-y plane. The early report of "atomic" resolution of the periodic lattice of NaCl(001) was obtained using this technique.[6]

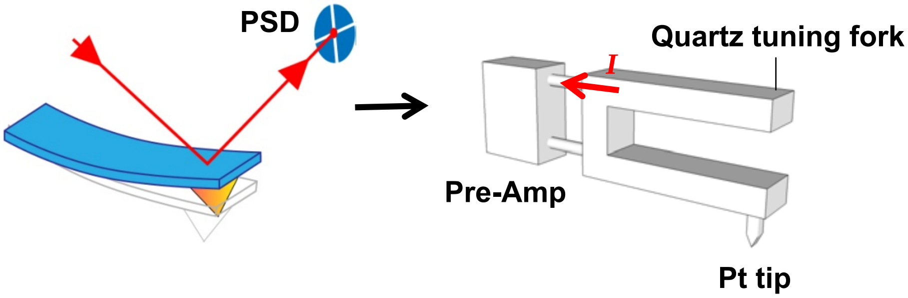

Figure 6.1. A schematic of AFM detection systems. Left, laser detection system. The tip-sample interaction force is sensed by the readout of the position changes of the laser spot through a photo sensitive diode (PSD). Right, quartz-tuning-fork-force-sensor detection system. The tip-sample interaction force is transduced to electric signals through the piezoelectric effect of quartz, which is then sensed by a pre-amplifier.

However, static AFM suffers from several problems. First, low stiffness (0.01-1 N m^{-1}) cantilever has to be used in order to increase the sensing of the force. This relatively soft cantilever is easily subject to thermal drifts. It is then rather difficult for the feedback system to maintain a constant interaction force during image acquisition. Furthermore, since the cantilever stiffness (k_c) is very low, a jump-to-contact instability occurs whenever the maximum interaction force gradient ($k_{ts} = |dF_{ts}/dz|$) exceeds k_c. This usually crashes an initially sharp tip and interferes with the feedback signal. In static contact mode, the image resolution is limited to the tip-surface contact radius (>10 nm). Most often, many "minitips" would be in contact with the surface and the resolution is typically >10 nm. It is also worthwhile to mention that since the tip is moved laterally in contact, the relatively large interaction force would be detrimental to samples, in particular soft bio-samples.

In order to overcome the accompanying problems with static AFM, dynamic operation mode was developed in the past decade, which led to a significant transformation of AFM.[5] Dynamic AFM has been emerging as a powerful and versatile technique for atomic and nanometer-scale characterization and manipulation of a variety of surfaces. High-resolution images of DNA, proteins and polymers have been obtained in air and liquids.[7]

Basically, dynamic AFM uses a vibrating cantilever instead of a static one. The vibration of the cantilever is typically monitored by the laser detection system. Changes of the vibration amplitude or frequency due to the tip-sample interaction force are used as feedback signal to control the tip positions. A thorough understanding of the tip motion dynamics is then critical for the understanding of the feedback mechanism, detection sensitivity and improvement of resolution.

Usually, a harmonic approximation is used to describe the dynamics of the tip with damping.[5] In this approximation, the cantilever-tip ensemble is modeled as a harmonic oscillator with effective mass m* and spring constant k_c. If we assume the average distance between the tip and sample surface is z_0 (see Figure 6.2), and the deflection of the cantilever from its equilibrium position is z, the instantaneous position of the tip relative to the surface is then z_0+z.

The equation of motion for the tip is then

$$m^{*}\ddot{z} + k_c z + \frac{m\omega_0}{Q_0}\dot{z} = F_{ts} + F_0\cos(\omega t) \tag{6.1}$$

in which F_0 and ω are the amplitude and angular frequency of the exciting force exerted by the driving piezo on the cantilever. Q_0, ω_0 and k_c are the quality factor, free angular resonance frequency and force gradient of the cantilever-tip ensemble, respectively.

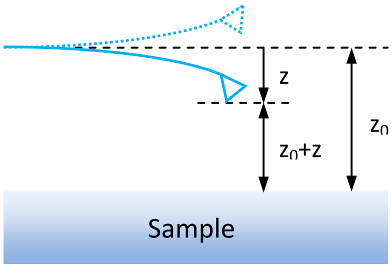

Figure 6.2. A scheme of the relevant spatial distances in dynamic AFM. The instantaneous position of the tip is defined with respect to the average position of the tip. The up deflection of the cantilever is defined to be positive z.[5]

Hence, in the absence of interaction force, Eq. (6.1) describes the motion of a forced harmonic oscillator with damping. This will generally give a solution of both static and transient states. Solving this equation with $F_{ts} = 0$ and ignoring the transient solution, the free amplitude of vibration as a function of frequency is obtained by the Lorenztian expression[5]

$$A(\omega) = \frac{F_0 / m}{[(\omega_0^2 - \omega^2)^2 + (\omega\omega_0 / Q_0)^2]^{1/2}} \tag{6.2}$$

and the phase shift by

$$\tan\varphi = \frac{\omega\omega_0 / Q_0}{\omega_0^2 - \omega^2} \tag{6.3}$$

where φ, the phase shift, is the angle by which the driving force leads the deflection of cantilever. When the tip is brought to the proximity of the surface, the interaction force will modify the vibration of the tip. The force acting on the tip is a complicated function of tip-sample distance $F_{ts}(d = z+z_0)$. Generally, there is no analytical solution for Eq. (6.1). Applying a small-amplitude approximation, in which the force can be written as

$$F_{ts}(d) = F(z_0) - k_{ts} z \tag{6.4}$$

where k_{ts} is force gradient evaluated at the equilibrium position z_0 of the tip. Thus Eq. (6.2) becomes

$$A(\omega) = \frac{F_0 / m}{[(\omega_e^2 - \omega^2)^2 + (\omega\omega_e / Q(z_0))^2]^{1/2}} \tag{6.5}$$

where the effective resonance frequency is calculated by

$$\omega_e = \sqrt{(k_c + k_{ts}) / m^*} \tag{6.6}$$

and the quality factor becomes a function of the average distance z_0 between tip and sample,

$$Q(z_0) = Q_0 \frac{\omega_e}{\omega_0} \tag{6.7}$$

assuming the damping coefficient γ is constant within a whole tip vibrating cycle.

Therefore, due to a change of the resonance frequency from ω_0 to ω_e, the amplitude and phase shift are then expected from Eqs. (6.2) and (6.3). These three parameter changes then can be used as feedback control to keep the tip in a constant equilibrium position relative to the sample atoms. Based on different feedback mechanisms, dynamic AFM technique includes two major types: amplitude modulation atomic force microscopy (AM-AFM) and frequency modulation atomic force microscopy (FM-AFM).

In AM-AFM, the cantilever-tip ensemble is vibrated at a constant frequency, which is the same of or near its free resonance frequency. The oscillation amplitude is used as a feedback control to measure the surface topography. Most of the AM-AFM experiments are performed in air or in liquids.[5] Although considerable achievements have been made by using this technique, attaining true atomic resolution image still encounters significant problems. Firstly, since AM-AFM tends to use a large oscillation amplitude (10-100 nm) and a relative stiff (of the order of a few 10 N/m) cantilever, the small amplitude approximation is not applicable. The analysis of the tip dynamics is complicated by several factors. The force gradient would vary considerably during a vibration cycle and induce nonlinear features in the dynamics of the tip motion. Several dissipative processes, such as surface adhesion hysteresis, viscoelasticity and electronic dissipation would be involved in the tip motion. Secondly, an intrinsic bi-stable state exists for the AM-AFM operation. This bi-stable state refers to the existence of two amplitude values with respect to a fixed frequency, and is due to the co-existence of attractive and repulsive forces between tip and sample surface. Therefore, it interferes with the amplitude feedback and causes instabilities during acquisition process. Additionally, AM-AFM is rarely used in ultrahigh vacuum (UHV) environment, although the UHV system may potentially boost the detection sensitivity. This is because the relatively high quality factor of the cantilever in vacuum will extend the lifetime (τ =

$2Q_0/\omega_0$) of the transient state of the tip motion, and result in a delay in amplitude feedback response.

Fortunately, most of the above-mentioned problems can be largely avoided by employing FM-AFM, which was invented by Albrecht and colleagues in 1991 for magnetic force microscopy.[8] In FM-AFM, the cantilever-tip ensemble is vibrated at its resonance frequency ω_e at all times. This is achieved by phase shifting the deflection signal and feeding it back to the piezo actuator which drives the cantilever. By scanning a cantilever across the sample (in the x-y plane) and adjusting z such that the frequency shift is constant, a map $z(x, y, \Delta\omega \approx \text{constant})$ is created.

By using a large amplitude (34 nm), a true atomic resolution image of the reactive Si(111)-(7×7) reconstruction surface was first obtained in UHV by Giessibl in 1995.[9] Since then a number of studies on conductive and insulating surfaces have been performed by using FM-AFM.[10] It has been found that the amplitude should be large when compared to the range of F_{ts} to attain optimal resolution:[11] jump-to-contact would still occur if a relatively small amplitude were used instead. On the other hand, the use of large amplitudes (>10 nm) is not comparable to the short range of chemical bonds, which have a range of ~1 Å. Therefore, a better understanding of the frequency shift with respect to the tip-sample interaction would be expected to provide insights to the choice of parameters in order to improve the sensitivity and resolution.

Giessibl et al.[12] have shown that reduced noise would be expected if we used small oscillation amplitude. By modeling the tip-sample interaction force as an exponential function of the tip-sample distance, the vertical noise δz was derived as follows:[12]

$$\delta z \propto \frac{\left(1+\sqrt{\frac{\pi}{2}}\left(\frac{A}{\lambda}\right)^{3/2}\right)}{A}\sqrt{TB} \tag{6.8}$$

where λ, T and B is the interaction force range, temperature, and detection bandwidth. According to Eq. (6.8), a minimal noise is expected when A ≈ λ (Å range) and the product of temperature and bandwidth is minimized. However operation with such very small amplitudes is not possible with conventional cantilevers due to the instabilities caused by jump-to-contact and perturbations of the oscillation by tip-sample dissipation. To overcome these problems, a cantilever with rather large stiffness (more than 1000 N/m) is required.

Because the commercial silicon cantilevers cannot afford such high stiffness, a piezoelectric quartz tuning fork usually used in watch industry (Fig. 6.1, right) has been used instead by researchers.[13-17] In addition, instead of the conventional laser-PSD detection scheme, the vibration of the quartz tuning fork can be directly monitored electronically, as the mechanical vibration of the tuning fork is transduced to electric signals through the piezoelectric effect of quartz, which is then detected by a pre-amplifier. High-resolution images have been obtained at room temperature by Giessibl et al.[18, 19] Additionally, when compared to silicon cantilevers, the relative frequency shift with respect to temperature is rather small for quartz tuning forks, which results in an enhanced stability of the force sensor. These studies show the potential application of quartz tuning forks in AFM imaging. However, the construction of quartz-tuning-fork-based AFM systems suitable for low-temperature measurements remains challenging. This is because silicon-based pre-amplifiers were used to sense the vibration of the quartz tuning forks in previous studies,[18-20] but silicon-based amplifiers are not functional at cryogenic temperatures due to carrier freeze-out. To carry out cryogenic (~ 4 K) temperature experiments with such systems, in previous attempts a thermal shield box was used to house the electronics.[21, 22] However, the close proximity of the box to the force sensor induces mechanical coupling to the tuning fork. Furthermore, heavy liquid helium consumption is expected due to the relatively high temperature inside the box (~ -40ºC).

In this chapter, we investigated the mechanical properties of quartz-tuning-fork-based force sensor and integrated it into a low-temperature AFM system. The optical detection scheme will be replaced by a home-made electronics design. A GaAs field effect transistor (FET)-based pre-amplifier, which functions at cryogenic temperatures, will be designed and coupled to the force sensor. Our goal is to construct a quartz tuning fork-based high-speed, high-resolution FM-AFM system applicable to especially low temperature and UHV environments. In Section 6.2, we outline the methods to design the pre-amplifier, the setup of the low-noise detection system and the assembly of the tuning-fork-tip ensemble. Noise and quality factor performance of the designed electronics, as well as feasibility of the force sensor, will be discussed in Section 6.3.1 and 6.3.2. The preliminary experiments on silicon surfaces will be discussed in Section 6.3.3. Conclusions will be presented in Section 6.4.

6.2 Experimental

6.2.1 Pre-amplifier

In the present study, a GaAs FET-based pre-amplifier was used instead of the conventional silicon-based circuits, since carrier freeze-out would not occur for GaAs at cryogenic temperatures. The circuit consists of a first-stage pre-amplifier and a second-stage op amp (see Fig 6.5). The first-stage preamplifier is put in the low temperature environment for the AFM test, while the second-stage op amp stays at room temperature.

The circuit was built on a copper-covered circuit board. Briefly, a designed electronic circuit was transferred to the covered copper using a conventional method followed by lift-off of the exposed copper by ferric chloride solution. Special care was taken to avoid wire crossing and ground loops, with a common ground being used throughout on the circuit board. The electronic units (op amps, resistors and capacitors) were then connected to the wires on the other side of the board. Since generally most of the noise comes from the first-stage amplifier,[23] the resistors used in this stage were metal film type with a relatively small thermal noise level and carbon resistors were used in other parts of the circuit instead.

Low-noise high-gain heterojunction GaAs MESFETs were used in this work for the first-stage amplifier. We choose three brands for comparison purposes: EPB018A5 from Excelics, ATF-35143-BLK from Agilent Technologies and FHX13X(14X,45X) from Fujitsu. Since the accumulation of static charge on the gate capacitor would induce a breakdown gate-to-source voltage, protective diodes were also used.

The op amp with large gain and wide bandwidth was preferred in the present design. We chose an OPA602 amplifier from Burr-Brown as the second stage. Several other types of op amps were also tested, such as OPA111 and OP27.

6.2.2 Low noise measurements

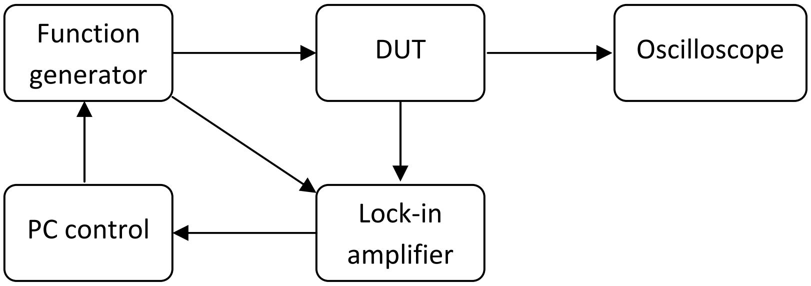

Figure 6.3. A schematic of the low-noise detection system.

The low-noise detection system was performed by using a lock-in amplifier (Figure 6.3). To evaluate the noise performance of the device under test (DUT), an alternating voltage signal was triggered by the function generator and fed to the DUT. A synchronized reference signal was sent to the Lock-in amplifier, which is used to test the noise level at various reference frequencies. The output of the DUT was connected to the input of Lock-in amplifier. The control of frequency tuning, measurement of output signal from DUT and tuning of reference frequency in Lock-in were realized through GPIB connection to a computer. A program written with Labview 6.1 was used to control the operations. Additionally, an oscilloscope was also connected to the DUT when necessary to monitor the signal and noise levels. To minimize the noise level induced by the different ground connections, the ground line from all the instruments including the DUT were connected to a common ground point.

The function generator used in this paper was a DS360 model from Stanford Research Systems. It exhibits a steady 25 ppm frequency stability and the frequency range is from 10 mHz to 200 kHz. The noise level of this generator is < -100 dBc. The low-distortion property enables us to use a sine wave with a small voltage of 4 μV (root mean square, rms) to excite the tuning fork.

Noise level detection was performed by using a SR830 DSP Lock-in amplifier (Stanford Research Systems). The time constant and slope used in the experiments is 300 ms and 12 dB, respectively. The oscilloscope was HP 54520A model from Hewlett Packard and was used as a monitor to adjust the offset potential at the converting terminal of the op amp. Additionally, it is also used in the evaluation of the amplifier gain.

To evaluate the noise performance at cryogenic temperature (~ 4 K), a cryostat of Model STVP-100 from Janis was used. The low temperature was obtained by injecting liquid helium into the chamber inside the cryostat. The temperature was monitored with a thermometer of Model 330 from Lakeshore. The circuit board was mounted on the end of a long rod equipped with the cryostat. Although the long rod may induce some mechanical vibration, which could be coupled to the circuit, the frequency of this vibration is rather low and so this coupling effect can be ignored. The temperature sensor (silicon diodes) was also attached to the end of the metal rod and in close proximity to the circuit board.

6.2.3 Tuning-fork-tip assembly

The quartz tuning fork used in this paper was from ECS Company. The free resonance frequency $f_{\mathrm{bare}} = 32.768$ kHz, and the spring constant is over 1000 N/m. The Q-factor is about 90,000 in a sealed state. The temperature stability is -0.04 ppm / ºC.

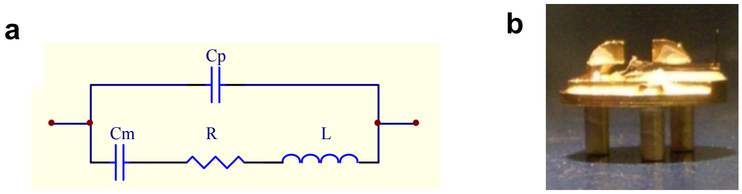

Figure 6.4. Quartz-tuning-fork-tip assembly. (a) Equivalent circuit of a tuning fork. (b) An optical image of the quartz-tuning-fork-tip assembly. One prong of the quartz tuning fork is glued to the tip holder. The Pt-Ir tip (appearing black) is glued perpendicularly to the other prong of the tuning fork.

The piezoelectric quartz tuning fork can be viewed as a parallel connection of the shunt capacitance C_p and motional units, C_m, R, L (inductor) as shown in Figure 6.4a. The series resonance corresponds to the cancellation of the impedance from the motional capacitor and that of the inductor, indicating a minimum of the absolute impedance value. The vibrational frequency of the quartz tuning fork is thus transduced into the electrical resonance frequency of the equivalent circuit. This resonance is used in the present study and the frequency shift due to the tip-sample interaction is used as a feedback signal to control the tip-sample separations.

The force sensor is made by attaching a tungsten tip to the end of the prong (Figure 6.4b). Silver paint was used so that the tip was electrically connected to one of the electrodes of tuning fork. The connection of the electrodes to the pre-amplifier circuit is realized by using an ultrathin Au wire with a diameter of 12 μm. This is to minimize the stress applied to the tuning fork.

6.3 Results

6.3.1 Noise performance

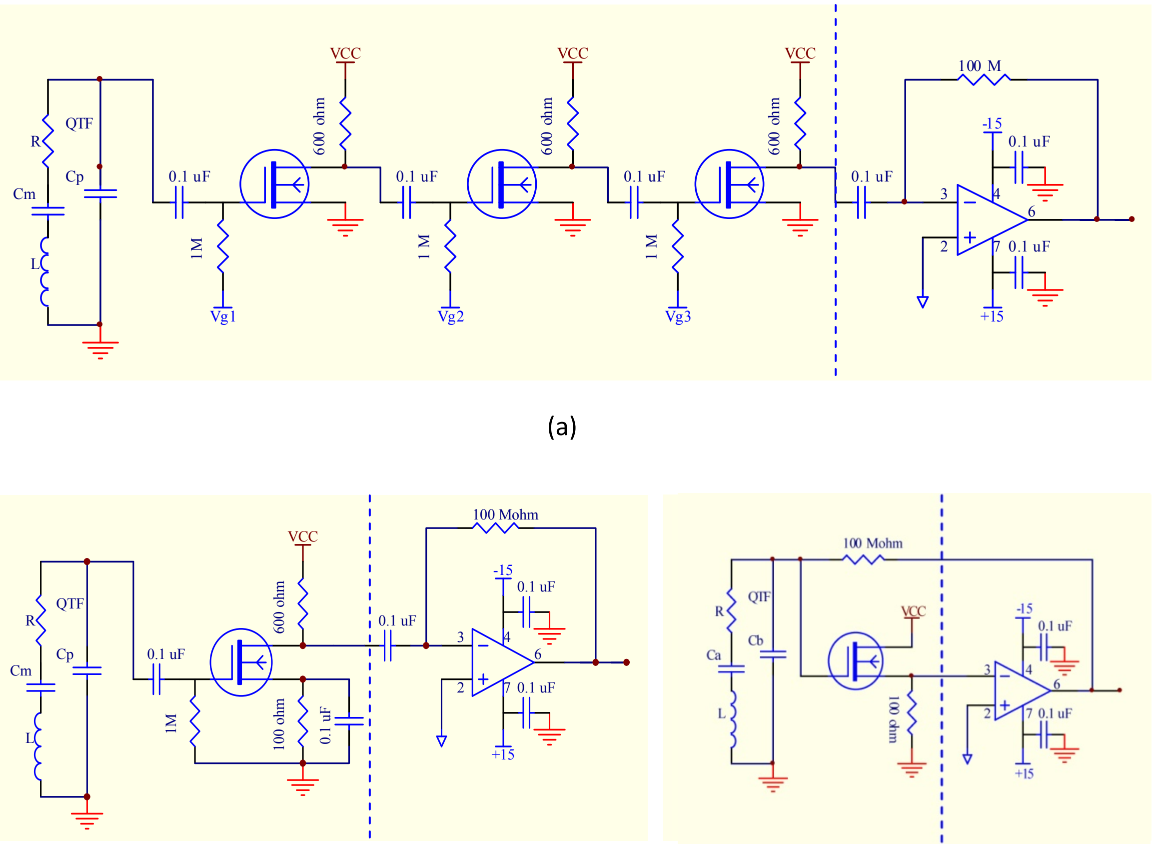

(a)

(b)

(c)

Figure 6.5. Low noise detection scheme. A schematic of three types of electronic circuits for low-noise detection of signal from tuning fork: (a) common-source, (b) self-biasing and (c) global feedback. Each of the circuits consists of a first-stage (left to the dashed line) pre-amplifier and a second-stage op amp (right of the dashed line).

Three types of pre-amplifiers: common-source, self-biasing and global feedback have been designed in this study, as shown in Figure 6.5a-c.

As mentioned previously, each of the circuits consists of a first-stage (left of the dashed line) pre-amplifier and a second-stage op amp (right of the dashed line). The first-stage pre-amplifier is put in the low-temperature environment for AFM test, while the second-stage op amp stays at room temperature. The GaAs MESFET used in the first stage is of n-type depletion mode. The op amp serves as the second stage for further amplification. As we know, the use of long thin wires at cryogenic temperature usually leads to a high (resistance-capacitance) time constant, which reduces the bandwidth of the amplifier.[24] More importantly, the use of long connection wire will cause a significant degradation of signal from the tuning fork with a high impedance (over 35 kΩ), because the impedance of the wire and tuning fork does not match. Therefore, in our design the input terminal of the first-stage preamplifier was placed as close as possible to the electrodes of the tuning fork.

As mentioned above, the noise induced from the first stage is critical to the overall noise performance, hence the parameters associated with this stage were optimized to obtain a minimized noise floor. Typical values of the resistors, capacitor and voltages were indicated in Figure 6.5. For instance, in common-source type, increase of the drain resistor value would increase both voltage gain and noise level. An optimal value of ~600 Ω was obtained in our experiment.

Table 6.1. Comparison of noise floor at room temperature for three types of amplifiers: common source, self-biasing and global feedback. The unit is μV $Hz^{-1/2}$

Common-source	Self-biasing	Global feedback
~ 13	~ 9	~ 1

The tuning fork can be either mechanically or thermally excited. In this experiment, the thermally activated tuning fork was used to evaluate the noise performance of the designed electronics so that no extra noise from the actuator was induced. It was found that little or no resonance signals were obtained for the common source and self-biasing amplifiers. Typical noise spectral density values at ~32768 Hz (resonance frequency of the tuning fork) are summarized in Table 6.1, where the noise floor for the global feedback is the lowest. The relatively noisier performance of the former two circuits likely overwhelmed the weak thermally activated resonant signals.

Figure 6.6a compared the noise performance for the global feedback with an op-amp-only amplifier circuit, which was used by Giessibl et al.[25] The corresponding circuits were also shown in Figure 6.6b. The experiments were performed at room temperature. It can be seen from the figure that these two circuits have a comparable noise floor and thermal activated signal can be observed for both. The resonance curve peaks at about 32764.8 Hz. Corresponding low-temperature (4.18 K) experiments showed that this peak shifted to 32711.5 Hz and a narrower sharp resonance peak was obtained (not shown here).

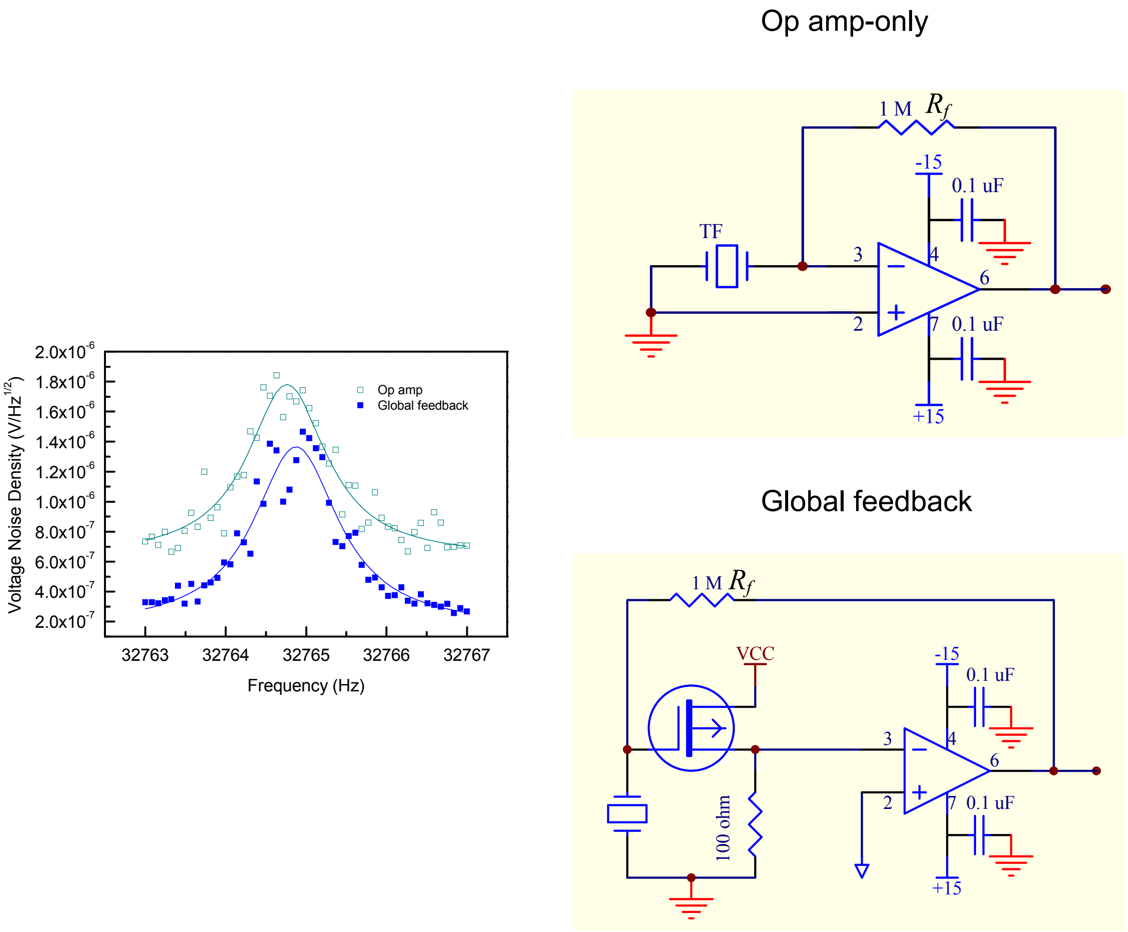

Op amp-only

Global feedback

(a) **(b)**

Figure 6.6. Noise performance. (a) Comparison of the noise spectral density for the op-amp-only and global feedback pre-amplifiers at room temperature; (b) Corresponding circuits for the two pre-amplifiers.

The sensitivity of the pre-amplifier (defined as V_{out}/z) can be determined experimentally and theoretically. According to the studies by Giessibl,[20] the sensitivity can be written as

$$S(f) = 24\pi f G d_{21} k_c L_e (L_e / 2 - L) / t^2 \tag{6.9}$$

where f, L_e, L, t are resonance frequency, tuning fork beam electrode length, beam length and beam thickness, respectively. d_{21} (= 2.31×10^{-12} C/N) is the coupling constant for quartz. G is the trans-impedance gain of the pre-amplifier. For op-amp only, $G = -R_f$ and for global feedback, the transfer function can be derived as[24]

$$G = \frac{V_{out}(\omega)}{I_{in}(\omega)} = -R_f \left[\frac{G_1(\omega)G_2(\omega)}{1 + G_1(\omega)G_2(\omega)} \right] \tag{6.10}$$

where R_f is the feedback resistor (see Figure 6.6b), and $G_1(\omega)$ and $G_2(\omega)$ are the voltage gain for the first- and second-stage global feedback amplifier. Since the op amp gain is usually far larger than that of the FET, G of the global feedback can be approximately $-R_f$ too. Using Eqs. (6.9) and (6.10), we obtained a sensitivity of 0.95 μV/pm for both circuits when $R_f = 1$ MΩ for both.

The sensitivity can also be obtained from Figure 6.6a. The output voltage is obtained by integrating over the resonance curve, subtracting that from the noise floor. The thermal noise amplitude was calculated to be about 1.2 and 1.3 μV for op-amp-only and global feedback circuits, respectively. The r.m.s. thermal vibration amplitude (A_{th}) is calculated from $k_c A_{th}^2 = k_B T$, where k_B is the Boltzmann constant. For room temperature ($T = 293$ K), $A_{th} = 1.49$ pm. Then the sensitivity is 0.81 and 0.87 μV/pm for op-amp-only and global feedback circuits, respectively.

The above study showed that at room temperature, the GaAs-based global feedback pre-amplifier can provide a good sensitivity comparable to the silicon-based op-amp-only amplifier, which enables the detection of even signal from a thermally activated tuning fork.

6.3.2 Quality factor

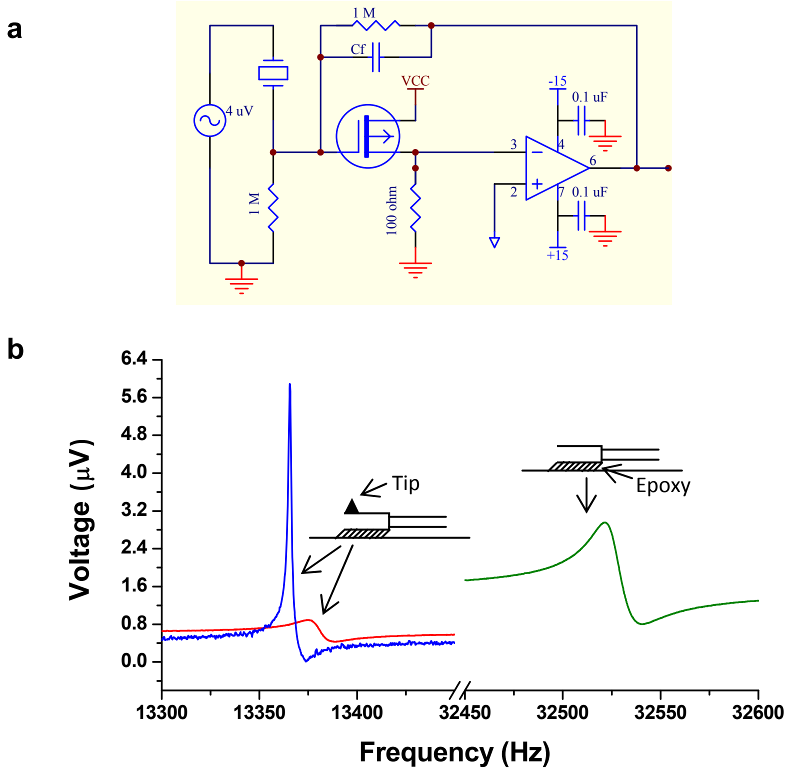

Figure 6.7. Excitation curves for quality-factor measurements. (a) Circuit (global feedback type) for external excitation experiments. (b) Excitation curves for a q-Plus type tip-tuning fork assembly sensor. Green, one prong is attached to the substrate and the curve is acquired at room temperature in air. Red, same as green except that the other prong is attached with a tip (filled triangle). Blue, same as red except the setup is in vacuum and the temperature is 77 K. The excitation voltage is 4 μV.

A high quality-factor (Q-factor) of the tuning-fork-tip ensemble is required for accurate detection of the frequency shift in FM-AFM. The Q-factor is examined by using an external excitation source. Figure 6.7a showed the circuit, where an extra resistor was connected in parallel with the tuning fork.

We examined the Q-factor for the q-Plus sensor (Figure 6.4b). Figure 6.7b showed the corresponding frequency response to the excitation. The Q-factor drops from ~30,000 (commercial) to ~900 due to the large damping effect of the epoxy. As a Pt-Ir tip is glued to the other prong of the tuning fork, resonance frequency shifted from 32521 Hz to 13375 Hz due to the extra mass added to the prong. Meanwhile, the Q-factor further drops to ~200. When in vacuum, the slight increases in both resonance frequency and Q-factor were observed (data not shown here). A large increase in Q-factor (~ 9000) is observed when the temperature is dropped to ~77 K (Figure 6.7b, blue line).

6.3.3 Topographic images

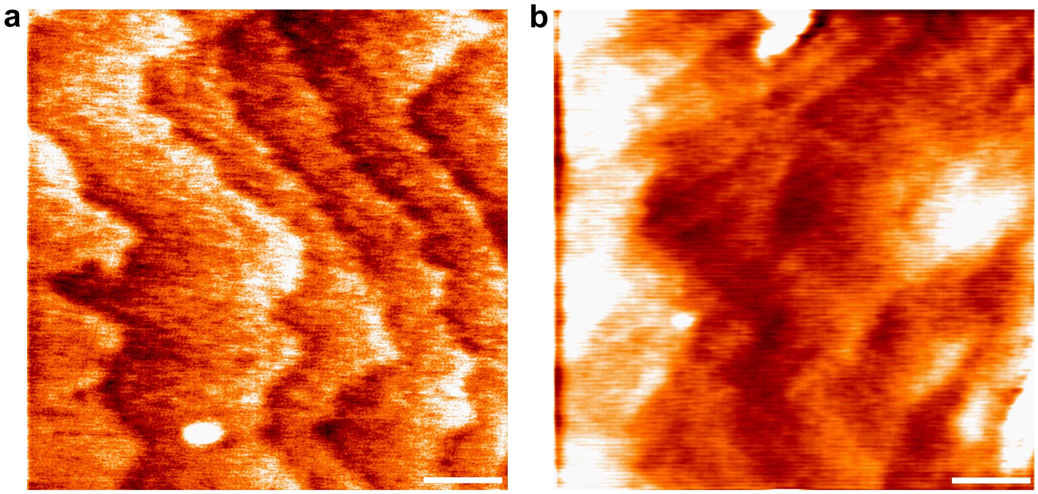

Figure 6.8. Frequency-modulated AFM topographic images. (a) H-terminated Si(111) at room temperature. (b) The same sample at liquid nitrogen temperature (77K). The set point is 20 Hz. The scale bar is 100nm. Vertical scale is from 0 to 2 nm.

Figure 6.8a shows typical frequency-modulated AFM topographic images of H-terminated Si(111) surfaces at room and liquid nitrogen temperature (77K), respectively.

This verifies our design of quartz-tuning-fork-based force sensor and pre-amplifier. The terrace and steps of at least one atomic height (~3.15 Å) are clearly seen on the images. However, the image resolution still needs to be improved in the future work. This may include optimization of the pre-amplifier design in order to further decrease the noise level; application of proper epoxy to minimize the damping of the q-Plus force sensor, etc.

6.4 Conclusion

In this chapter, the electronics functional at cryogenic temperatures to detect the signal from a quartz tuning fork has been designed. This force-sensor-electronic-detector system has been employed in frequency-modulated atomic force microscopy (FM-AFM). Noise performance of three types of pre-amplifier electronics has been compared. Results show that the force-sensor-global-feedback circuit detector system induces the lowest noise floor. The high detection sensitivity of this system demonstrates its ability to be used in FM-AFM at cryogenic temperatures. The quality factor of the tuning-fork-tip ensemble has also been examined. We found that a high Q of ~9000 in vacuum at ~77K is obtained for a q-Plus tuning-fork-tip ensemble system. This facilitates accurate detection of frequency in AFM operation. Surface topographic imaging from H-terminated Si(111) surfaces has been achieved, which verifies our rational design of quartz-tuning-fork-based force sensor and pre-amplifier.

6.5 References

1. Binning, G., Rohrer, H., Gerber, C. & Weibel, E. Surface studies by scanning tunneling microscopy. *Phys Rev Lett* **49**, 57-61 (1982).
2. Binnig, G., Quate, C.F. & Gerber, C. Atomic force microscope. *Phys Rev Lett* **56**, 930-933 (1986).

3. Morita, S., Wiesendanger, R., Meyer, E. & Giessibl, F.J. Noncontact atomic force microscopy. (Springer, Berlin; New York; 2002).

4. Giessibl, F.J. & Quate, C.F. Exploring the nanoworld with atomic force microscopy. *Phys Today* **59**, 44-50 (2006).

5. Garcia, R. & Perez, R. Dynamic atomic force microscopy methods. *Surf Sci Rep* **47**, 197-301 (2002).

6. Meyer, G. & Amer, N.M. Optical-beam-deflection atomic force microscopy - the NaCl (001) surface. *Appl Phys Lett* **56**, 2100-2101 (1990).

7. Bustamante, C. & Keller, D. Scanning force microscopy in biology. *Phys Today* **48**, 32-38 (1995).

8. Albrecht, T.R., Grutter, P., Horne, D. & Rugar, D. Frequency-modulation detection using high-Q cantilevers for enhanced force microscope sensitivity. *J Appl Phys* **69**, 668-673 (1991).

9. Giessibl, F.J. Atomic-resolution of the silicon (111)-(7x7) surface by atomic-force microscopy. *Science* **267**, 68-71 (1995).

10. Sugawara, Y., Ohta, M., Ueyama, H. & Morita, S. Defect motion on an InP(110) surface observed with noncontact atomic-force microscopy. *Science* **270**, 1646-1648 (1995).

11. Giessibl, F.J. Forces and frequency shifts in atomic-resolution dynamic-force microscopy. *Phys Rev B* **56**, 16010-16015 (1997).

12. Giessibl, F.J., Bielefeldt, H., Hembacher, S. & Mannhart, J. Imaging of atomic orbitals with the Atomic Force Microscope - experiments and simulations. *Ann Phys-Berlin* **10**, 887-910 (2001).

13. Giessibl, F.J. Advances in atomic force microscopy. *Rev Mod Phys* **75**, 949-983 (2003).

14. King, G.M. & Nunes, G. Attractive-mode force microscope for investigations of biomolecules under ambient conditions. *Rev Sci Instrum* **72**, 4261-4265 (2001).

15. Patil, N.G. & Levy, J. Low-noise variable-temperature preamplifier for piezoelectric tuning fork force sensors. *Rev Sci Instrum* **73**, 486-487 (2002).

16. Urazhdin, S., Tessmer, S.H. & Ashoori, R.C. A simple low-dissipation amplifier for cryogenic scanning tunneling microscopy. *Rev Sci Instrum* **73**, 310-312 (2002).

17. Jahncke, C.L., Brandt, O., Fellows, K.E. & Hallen, H.D. Choosing a preamplifier for tuning fork signal detection in scanning force microscopy. *Rev Sci Instrum* **75**, 2759-2761 (2004).

18. Giessibl, F.J. Atomic resolution on Si(111)-(7x7) by noncontact atomic force microscopy with a force sensor based on a quartz tuning fork. *Appl Phys Lett* **76**, 1470-1472 (2000).

19. Giessibl, F.J., Hembacher, S., Bielefeldt, H. & Mannhart, J. Subatomic features on the silicon (111)-(7x7) surface observed by atomic force microscopy. *Science* **289**, 422-425 (2000).
20. Giessibl, F.J. High-speed force sensor for force microscopy and profilometry utilizing a quartz tuning fork. *Appl Phys Lett* **73**, 3956-3958 (1998).
21. Hembacher, S., Giessibl, F.J. & Mannhart, J. Evaluation of a force sensor based on a quartz tuning fork for operation at low temperatures and ultrahigh vacuum. *Appl Surf Sci* **188**, 445-449 (2002).
22. Giessibl, F.J., Hembacher, S., Herz, M., Schiller, C. & Mannhart, J. Stability considerations and implementation of cantilevers allowing dynamic force microscopy with optimal resolution: the qPlus sensor. *Nanotechnology* **15**, S79-S86 (2004).
23. Motchenbacher, C.D. & Connelly, J.A. Low-noise electronic system design. (Wiley, New York; 1993).
24. Yang, C.H., Chang, T.H., Yang, M.J. & Moore, W.J. A low noise transimpedance amplifier for cryogenically cooled quartz tuning fork force sensors. *Rev Sci Instrum* **73**, 2713-2716 (2002).
25. Hembacher, S., Giessibl, F.J. & Mannhart, J. Force microscopy with light-atom probes. *Science* **305**, 380-383 (2004).